Development and Application of a Liquid Core Waveguide Membrane Microreactor

Entwicklung und Anwendung eines Fluidgefüllter Hohlkernlichtleiter-Membranreaktors

TECHNISCHE
UNIVERSITÄT
DARMSTADT

Vom Fachbereich Chemie

der Technischen Universität Darmstadt

zur Erlangung des Grades

Doktor-Ingenieurs

(Dr.-Ing.)

Dissertation

von Sebastián Ponce

Erstgutacher /in :   Prof. Dr.-Ing. Dipl.-Kfm. Bastian J. M. Etzold

Zweitgutachter/in: Prof. Dr. Christian Hess

Darmstadt 2019

Acknowledgments

I would like to thank Prof. Dr.-Ing. Dipl.-Kfm. Bastian Etzold for the advisory, and mostly patience for helping me to become a better student. I hope I can transfer his sense of quality, hard work, and fairness into my next steps. In addition, I would like to thank Prof. Alfons Drochner for his helpful advisory during my work. Finally, I would like to thank to all the etzoldlab staff for letting me work in a nice environment, in special to Hendryk for being such a welcoming and good friend for the last years.

"Este trabajo va enteramente dedicado a mis padres: Neptalí y Cecilia."

Most parts of this work, such as figures, tables, theoretical considerations, and text segments have been already published or are about to be published in form of publications.

Publications:

D. Voß, S. Ponce, S. Wesinger, B. J. M. Etzold, and J. Albert:

"**Combining autoclave and LCWM reactor studies to shed light on the kinetics of glucose oxidation catalyzed by doped molybdenum-based heteropoly acids**"

RSC Advances 2019, accepted

S. Ponce, M. Trabold, A. Drochner, J. Albert, and B.J.M. Etzold:

Insights into the redox kinetics of vanadium substituted heteropolyacids through liquid core waveguide membrane microreactor studies

Chemical Engineering Journal 2019, 369, 443-450. DOI: doi.org/10.1016/j.cej.2019.03.103

S. Ponce, H. Christians, A. Drochner and B.J.M. Etzold:

An optical Microreactor Enabling In Situ Spectroscopy Combined with Fast Gas-Liquid Mass transfer

Chemie Ingenieur Technik 2018*, 90, 11, 1855-1863*. DOI: doi.org/10.1002/cite.201800061

Presentation:

Liquid core waveguide membrane microreactor in situ studies of V-substitution in heteropoly acid catalysts in biomass oxidation

Jahrestreffen Reaktionstechnik: 27-29.05.2019 in Würzburg-Germany (Presenter: Prof. B.J.M Etzold)

A novel optical microreactor for gas/liquid reactions

15th International Conference on Micro Reaction Technology (IMRET15): 29-31.10.2018 in Karlsruhe-Germany

Posters:

Explaining redox activity of V-substituted heteropoly acid catalysts in biomass oxidation through liquid core waveguide membrane microreactor studies

14th European Congress on Catalysis, EuropaCat 2019: 18-23.08.2019 in Aachen-Germany

An optical micoreactor for gas-liquid reactions

Photo4future final conference: 12-13.11.2018 in Eindhoven- The Netherlands

A new concept for a microreactor with intense light/matter and gas/liquid interaction

25th International Conference on Chemical Reaction Engineering (ISCRE 25): 20-23.05.2018 in Florence-Italy

Optical microreactors using polymer based liquid core waveguides

Jahrestreffen Reaktionstechnik: 22-24.05.2017 in Würzburg-Germany

Catalytic Photonic Crystal Fiber Microreactors

50. Jahrestreffen Deutscher Katalytiker: 15-17.03.2017 in Weimar-Germany

Contents

Abstract

Optofluidic devices are unique as they combine properties of microreactors with an enhanced light-sample interaction. This can be advantageous for developing *in situ* spectroscopy as also photoactivation. However, up to now, their application in gas-liquid reactions can only be studied to a limited extend, as gas bubbles impede light transmission. To overcome this limitation in this work, a novel liquid core waveguide membrane (LCWM) microreactor combining intense light matter interaction for *in situ* sensing and/or photoactivation and excellent gas-liquid mass transfer is designed, realized, characterized and applied in three case studies. Basis is a liquid-filled Teflon amorphous fluoropolymer (Teflon AF) tube, which provides light transmission within the liquid core and gas permeation through the wall. Characterization of the new reactor was carried out from an optical and engineering point of view. The LCWM microreactor allows operating in a wide spectral range (240-1500 nm) with relatively low optical losses (UV/Vis regime: 1.67 dB m^{-1}). A working regime preventing gas bubble formation for CO_2, N_2 and synth. air was deduced for semi-batch and flow operation for pressures up to 8 bar. Furthermore, it was shown that residence time distribution (RTD) experiments can be carried out using the optical equipment of the reactor.

The capabilities of the LCWM setup are demonstrated for three case studies: i. deducing redox kinetics of different heteropolyacids during the oxidation of biomass to formic acid (the 'OxFA process'), ii. disentangling the complex network of (photo)degradation of methylene blue (MB) in glucose-alkaline solutions, and iii. studying ultra-fast (photo)degradation of silver nanoparticle (AgNP) colloids.

For the first application, the potential of this reactor concept to derive kinetics in gas-liquid reactions is demonstrated. For vanadium-substituted, Keggin-type heteropoly acids (HPA-n, n represents the degree of V substitution), the kinetics of the reduction and reoxidation step of the catalyst cycle was deduced using *in situ* UV/Vis spectroscopy. Reduction was studied from 40 to 80 °C under anaerobic conditions: a strong dependency of the reduction kinetics was deduced. In combination with additional cyclic voltammetry (CV) and electron paramagnetic resonance (EPR) characterization, it can be assumed that two active centers promote this reaction, the dissolved vanadium species, and the HPA itself, while the existence and proportions of both types depends on the degree of vanadium substitution. Being the HPA-5 complex the most active catalyst for biomass oxidation. On the other side, as demonstrated in the characterization section, the rapid mass transfer allowed transient response experiments to be carried out for the reoxidation step, which was studied up to 150 °C. Switching from

anaerobic to aerobic conditions, an even stronger dependency of the reoxidation kinetics on the degree of vanadium substitution was revealed. Higher V-substituted catalysts (e.g. HPA-5 and HPA-2) showed to be able to reoxidize at mild temperature conditions (< 90 °C) while non- and mono-substituted catalyst (HPA-0 and HPA-1) needed higher temperatures (> 100 °C), making the reoxidation step rate determining.

For the MB degradation study, the potential of the LCWM optical setup for revealing the complex interplay of several reaction and degradation pathways in gas-liquid photocatalytic systems is demonstrated. By combining long path lengths, intense light matter interaction for *in situ* characterization and/or photoactivation, and transient response studies, the photoenhanced methylene blue redox cycle in alkali is studied. Deconvolution of high resolution UV/Vis spectra, together with common liquid-phase characterization techniques, gives rise to several photo and non-photoactivated competing reaction pathways taking place. Accounting for all studied effects, it can be assumed that in addition to the redox cycle, photoexcited methylene blue fastly degrades via N/demethylation and deamination steps, forming new species which subsequently deprotonate in alkali. Furthermore, in the presence of molecular oxygen, the formation of highly reactive singlet oxygen via a photosensitizer cycle is likely, revealing an additional path for further degradation of organic matter in solution.

For the final application, the potential of the reactor to study photochemical transformations experienced in colloidal solutions is demonstrated. For highly diluted citrate-capped silver nanoparticles of average diameter $\approx$ 9 nm, the kinetics of the photooxidation by UV light irradiation was deduced. UV-induced photooxidation under anaerobic and aerobic conditions, variable initial citrate concentrations, and temperatures up to 80 °C was studied: A strong dependency of the photooxidation kinetics on the gas saturation was deduced following a pseudo-first order kinetic mechanism. Photoexcited NP surfaces seem to actively interact with dissolved molecular oxygen. Moreover, higher citrate concentrations seem to slow down the overall degradation process by protecting the nanoparticle surface against oxygen molecules. In addition, the effect of broader light (Vis) irradiation was studied. By applying the MIE model by fitting the UV/Vis surface-plasmon resonance (SPR) spectra recorded within the LCWM reactor, it can be assumed that in addition to the photooxidation process (fast), the indirect photooxidation of citrate (slow) induces nanoparticle growth. Being both two competing mechanisms. Finally, exemplary long-term stability studies under semi-batch and continuous operation were developed. Silver colloids in batch conditions and broad light irradiation tend to develop cyclic oxidation ←→ reduction processes, which results in NPs degradation and re- nucleation and growth. On the other hand, flow conditions seem to enhance nanoparticles agglomeration, but also the indirect citrate oxidation, which results in metallic silver deposition

to the formation of big flat surfaces. Interestingly, all above studied effects seem to happen in a shorter time scale (min to hours) compared to common batch photo-reactors (hours to months).

Zusammenfassung

Optofluidische Geräte sind einzigartig, da sie die Eigenschaften von Mikroreaktoren mit einer verbesserten Wechselwirkung zwischen Licht und Probe kombinieren. Dies kann sowohl für die Entwicklung der *in-situ*-Spektroskopie als auch für die Photoaktivierung vorteilhaft sein. Bisher ist ihre Anwendung in Gas-Flüssig-Reaktionen jedoch nur eingeschränkt untersuchbar, da Gasblasen die Lichtdurchlässigkeit beeinträchtigen. Mit dem Ziel, diese Einschränkung in dieser Arbeit aufzuheben, wurde in drei Fallstudien ein fluidgefüllter Hohlkernlichtleiter-Membranreaktor (LCWM, *Liquid Core Waveguide Membrane*) entwickelt. Der neuartige Reaktor kombiniert eine intensive Wechselwirkung zwischen Licht und Materie für die *in-situ*-Erfassung und Photoaktivierung mit einem hervorragenden Gas-Flüssig-Stofftransfer. Basis ist ein flüssigkeitsgefüllter Teflon AF-Schlauch (AF, *Amorphous Fluoropolymer*), der für Lichtdurchlässigkeit innerhalb des Flüssigkeitskerns und Gasdurchlässigkeit durch die Wand sorgt. Anschließend wird eine erste Setup-Charakterisierung aus optischer und technischer Sicht entwickelt. Der LCWM-Mikroreaktor zeigt, dass ein breiter Spektralbereich (240-1500 nm) mit relativ geringen optischen Verlusten (UV/Vis-Bereich: 1.67 dB m^{-1}) erreichbar ist. Ein Arbeitsregime, das die Bildung von Gasblasen verhindert, wurde getestet und für den halbkontinuierlichen (z. B. transiente Reaktionsstudien) und kontinuierlichen Betrieb für Gasdrücke (CO_2, N_2, synthetische Luft) von bis zu 8 bar abgeleitet. Darüber hinaus ergaben Versuche zur Verweilzeitverteilung im untersuchten Strömungsbereich innerhalb des Rohres Bodenstein-Zahlen von 21 bis 60, deren Einfluss bei Reaktionsratenberechnungen für niedrige Umsätze vernachlässigbar ist.

Die Fähigkeiten des LCWM-Setups werden anhand von drei Fallstudien demonstriert: i. Redoxchemie verschiedener Heteropolysäuren bei der Oxidation von Biomasse zu Ameisensäure („OxFA-Verfahren"), ii. (Photo-) Abbau von Methylenblau (MB) in Glucose-Alkali-Lösungen und iii. ultraschneller (Photo-) Abbau von Silber-Nanopartikel-Kolloiden.

Für die erste Anwendung wird das Potenzial dieses Reaktorkonzepts zur Ableitung der Kinetik in Gas-Flüssig-Reaktionen demonstriert. Für Vanadium-substituierte Heteropolysäuren vom Keggin-Typ (HPA-n, n steht für den Grad der V-Substitution) wurde die Kinetik des Reduktions- und Reoxidationsschritts des Katalysatorzyklus unter Verwendung von *in-situ* UV/Vis-Spektroskopie abgeleitet. Die Reduktion wurde unter anaeroben Bedingungen von 40 bis 80 °C untersucht: Eine starke Abhängigkeit der Reduktionskinetik wurde abgeleitet. In Kombination mit zusätzlicher Cyclovoltammetrie und Elektronenspinresonanz kann davon ausgegangen werden, dass zwei aktive Zentren diese Reaktion fördern, die gelöste Vanadiumspezies und das

HPA selbst. Dabei hängt das Vorhandensein und die Anteile beider Typen vom Grad der Vanadium-Substitution ab. Der HPA-5-Komplex ist der aktivste Katalysator für die Oxidation von Biomasse. Demgegenüber ermöglichte der schnelle Stoffübergang, wie im Abschnitt zur Charakterisierung gezeigt, die Durchführung von Experimenten mit transienten Reaktionen für den bis 150 °C untersuchten Reoxidationsschritt. Beim Wechsel von anaeroben zu aeroben Bedingungen wurde eine noch stärkere Abhängigkeit der Reoxidationskinetik vom Vanadium-Substitutionsgrad festgestellt. Höher V-substituierte Katalysatoren (z. B. HPA-5 und HPA-2) konnten bei milden Temperaturbedingungen (<90 °C) reoxidieren, während nicht- und monosubstituierte Katalysatoren (HPA-0 und HPA-1) höhere Temperaturen benötigten (> 100 °C). Das bedeutet, dass die Reoxidation der geschwindigkeitsbestimmende Schritt ist.

Für die MB-Abbauuntersuchung wird das Potenzial des optischen LCWM-Aufbaus zum Aufdecken des komplexen Zusammenspiels mehrerer Reaktions- und Abbauwege in photokatalytischen Gas-Flüssig-Systemen demonstriert. Durch die Kombination von hohen Weglängen, intensiver Wechselwirkung mit leichter Materie zur *in-situ*-Charakterisierung und/oder Photoaktivierung und transienten Reaktionsstudien wird der photoaktivierte Methylenblau-Redoxzyklus im alkalischen Milieu untersucht. Die Entfaltung von hochauflösenden UV/Vis-Spektren in Verbindung mit gängigen Flüssigphasen-Charakterisierungstechniken führt zu mehreren photo- und nicht-photoaktivierten konkurrierenden Reaktionswegen. Unter Berücksichtigung aller untersuchten Effekte ist davon auszugehen, dass das photoangeregte Methylenblau neben dem Redoxzyklus über N/Demethylierungs- und Desaminierungsschritte schnell abgebaut wird und neue Spezies entstehen, die anschließend im Basischen deprotonieren. Darüber hinaus ist in Gegenwart von molekularem Sauerstoff die Bildung von hochreaktivem Singulett-Sauerstoff über einen Photosensibilisator-Zyklus wahrscheinlich, was einen zusätzlichen Weg für den weiteren Abbau von organischem Material in der Lösung aufzeigt.

Für die abschließende Anwendung wird das Potenzial des Reaktors zur Untersuchung photochemischer Umwandlungen in kolloidalen Lösungen demonstriert. Die Kinetik der Photooxidation durch Bestrahlung mit UV-Licht wurde für hochverdünnte Citrat-verkappte Silbernanopartikel mit einem durchschnittlichen Durchmesser von 9 nm abgeleitet. UV-induzierte Photooxidation unter anaeroben und aeroben Bedingungen, variable anfängliche Citratkonzentrationen und Temperaturen bis zu 80 °C wurde untersucht: Eine starke Abhängigkeit der Photooxidationskinetik von der Gassättigung wurde nach einem kinetischen Mechanismus der Pseudo-ersten Ordnung abgeleitet. Photoangeregte NP-Oberflächen scheinen aktiv mit gelöstem molekularem Sauerstoff zu interagieren. Des Weiteren scheinen höhere Citratkonzentrationen den gesamten Abbauprozess zu verlangsamen, indem sie die

Nanopartikeloberfläche vor Sauerstoffmolekülen schützen. Darüber hinaus wurde der Effekt einer breiteren Bestrahlung mit Licht (Vis) untersucht. Bei Anwendung des MIE-Modells durch Anpassen der im LCWM-Reaktor aufgezeichneten UV/Vis-Oberflächenplasmonresonanzspektren kann davon ausgegangen werden, dass die indirekte Photooxidation von Citrat (langsam) zusätzlich zum Photooxidationsprozess Nanopartikelwachstum induziert. Die beiden Mechanismen konkurrieren miteinander. Abschließend wurden beispielhafte Langzeitstabilitätsstudien im halbkontinuierlichen und kontinuierlichen Betrieb entwickelt. Silberkolloide neigen unter diskontinuierlichen Bedingungen und bei Bestrahlung mit breitem Licht dazu, zyklische Oxidations-/Reduktionsprozesse zu entwickeln, die zum Abbau, zur erneuten Keimbildung und zum Wachstum von NPs führen. Demgegenüber scheinen die Fließbedingungen die Agglomeration von Nanopartikeln zu fördern, aber auch die indirekte Oxidation von Citrat, die zur Abscheidung von metallischem Silber und zur Bildung großer flacher Oberflächen führt. Interessanterweise scheinen alle oben untersuchten Effekte in einer kürzeren Zeitskala (Minuten bis Stunden) als bei herkömmlichen Batch-Fotoreaktoren (Stunden bis Monate) aufzutreten.

1. Introduction

Microreactor technology has emerged as an enabling tool for studying chemical reactions. Advantageous are the reduced safety hazards (e.g. for highly exothermic reactions or toxic substrates), minimal sample consumption, high reactor surface-to-volume ratio (10000 to 50000 $m^2\,m^{-3}$), enhanced mass-and heat-transfer, and strictly control of reaction parameters [1-3]. Lately, the integration of light led to the appearance of novel optofluidic [4] and continuous flow [5] devices. They have gained special attention, as they combine the precise control of microreactors with intensive light-fluid interaction. This can be advantageous for *in situ* spectroscopy, improved detection, and/or photoactivation. Applications of optofluidic devices can be various, such as in biomedicine, sensing, materials synthesis and characterization, waste water treatment, solar energy storage, and organic synthesis for the preparation of small molecules for pharma industry [4-8].

Remarkable example are optofluidic hollow-core photonic crystal fibers (HC-PCF), which allows low loss light transmission over long path-lengths [4]. These were employed for highly sensitive *in situ* monitoring of reaction products and efficient driving of photochemical reactions. Examples of successfully developed reactions within HC-PCF microreactors are: the photochemical conversion of Vitamin B_{12} [9], the photochemical and thermal *cis-trans* isomerization of azo dyes [10], homogenous catalyzed degradation of synthetic dyes [11], and heterogeneous catalyzed hydrogenation of ethane [12] and azobenzenes [13, 14]. However, as the presence of bubbles impede light guidance, these devices can only be employed limited for studying gas-liquid reactions, e. g. by employing a pre-saturated liquid phase. Depending on the solubility strong concentration gradients of the dissolved components result, which are unwanted for kinetic studies. Furthermore, a fast exchange of the gas phase component is not possible, thus transient response experiments, which can give important insight to catalyst kinetics, cannot be carried out.

On the other hand, within the field microreactors hydrophobic and porous polymer tubes were shown to be excellent gas-liquid contactors providing fast gas-liquid mass transfer. In this sense, Ley et al. introduced the tube-in-tube membrane reactor concept that consist of a non-permeable tube surrounding the Teflon AF [15]. The space between the tubes is filled with pressurized gas, and the liquid reactants are pumped into the inner tube. As a result, gas permeates through the inner wall, and dissolves into the liquid stream. This membrane microreactor technology has been successfully applied in a variety of multiphase reactions like oxidations, carbonylations, ozonolysis, hydrogenation, among many others [16-21].

Interestingly, Teflon AF-2400, shows the lowest refractive index (η) for a polymer known (1.29). Thus, a liquid filled tube is able to transmit light by total internal reflection (TIR) when filled with most liquids and especially also when filled with water. Optical paths over the meter scale are reported and Teflon AF tubes are applied as liquid core waveguides (LCW) [22]. Using this technique, UV/Vis/NIR [23, 24], fluorescence [25, 26], and Raman spectroscopy [27] measurements of highly diluted substrates have been performed in the last two decades [28, 29].

Thus, Teflon AF tube reactors combine two remarkable properties:

- the possibility of guiding light within a liquid core and
- the very fast gas-liquid mass transfer through the membrane wall.

Based on this, a novel liquid core waveguide membrane microreactor (LCWM) leveraging both properties is in principle possible. Such a reactor would be of high interest, and developing such a device would advance the possibilities of optofluidic microreactors for gas-liquid reactions strongly. In this thesis, such a reactor concept is developed, realized and validated. Furthermore, three exemplary case studies were identified, to show the advantages of such a reactor concept. First, the study of the reduction and reoxidation kinetics of vanadium substituted Keggin-type heteropolyacids during biomass oxidation. UV/Vis spectroscopy can allow to follow the concentrations of the reduced and oxidized form of the catalyst, while through the gas phase anaerobic and aerobic conditions can be applied. Second case study is the complex interaction of (non)photoactivated reactions of methylene blue in glucose-alkaline solutions. *In situ* spectroscopy, photoactivation, and highly diluted systems, under aerobic and anaerobic conditions are employed to enhance and monitor possible side reactions. Finally, for the third case study, the LCWM reactor concept is applied to develop ultra-fast (photo)degradation studies of silver nanoparticle colloids taking advantage of their surface-plasmon resonance properties. As before, *in situ* sensing, photoactivation (UV and/or Vis), highly diluted systems, and fully gas saturation are employed to study the NP photochemical transformations.

2. State of the Art

2.1. Microreactor technology

The application of microreactor technology has gained significant importance in recent years. Microdevices are of interest not only for academic investigations, but also for the chemical and pharmaceutical industry [30]. By definition, microstructured reactors are reactors with three-dimensional structures, in which the inner dimensions should be under a millimeter of size. They are commonly fabricated from different kind of materials, such as polymers, ceramics, stainless steel, and silicon. The advantages of microreactors are [1, 30, 31]:

i. High surface-area-to-volume ratio: in microreactors the specific areas lie between 10000 and 500000 m^2 m^{-3} compared to those of traditional reactors (100 to max. 10000 m^2 m^{-3}).

ii. Improved heat transfer: as the heat transfer is inversely proportional to channel diameter, values up 50 kW m^{-2} K^{-1} can be obtained, which are significant higher to ones obtained for traditional heat exchangers.

iii. Enhanced mass transport: mixing times usually down to several milliseconds are considerably short compared to the ones in conventional systems. Thus, the influence of mass transport on the overall reaction can be reduced.

iv. Defined flow conditions: flows in microreactors are mostly laminar, directed, and highly symmetric. However, it is also possible to generate multiphase flows, e.g. capillary flow, slug flow, segmented flow, etc.

v. Control of reaction conditions: process parameters, such as pressure, temperature, residence time, and flow speed are easily controlled.

vi. Increased safety: hazards related to highly exothermic or explosive reactions can be reduced.

A variety of designs have been developed for different applications, nevertheless, they can be classified in two categories: "lab-on-a-chip" designs, and capillary devices. Chip-designs normally consist of microchannels built in glass and metal systems with adaptations from the microelectronics industry (e.g. dry or wet-etching process). Capillary devices, on the other side, generally involve polymer tubing (> 0.5 mm, i.d.) with flow rates greater than 1 mL min^{-1}. Both types have been widely applied in different type of reactions, such as the synthesis of organic (e.g. zeolites) [32, 33], semiconductor [34], and metal nanoparticles [35], polymerization reactions [36], bio-synthesis [37], photochemical [38] and electrochemical [39]

transformations, and the developing of organic transformations in gas-liquid-solid [40], gas-liquid [41], and liquid-liquid phase [42].

2.1.1. Optical microreactors

Recent advances in microreactor technology, nanochemistry, and solid state lighting have impulse the development of optical microreactors for the study and development of photochemical reactions. Two type of arrangements are characteristic for this type of reactors: optofluidic devices [4], which allow *in situ* sensing and/or photoactivation within the setup due to light guidance within the liquid, and flow reactors with external light irradiation [5] widely used in photochemistry and photocatalysis in the last years.

Optofluidics is usually referred as "the marriage of optics and fluidics". Thus, these setups typically consist of fluidic and photonic components where at least one of the optical functions is realized using a fluid material [43]. Many applications for these setups can be found in the areas of biological and chemical analysis, such as absorption spectroscopy, fluorescence detection, surface-enhanced Raman spectroscopy, RI detection, among others [44-46]. For instance, one remarkable example is the fiber-based hollow-core photonic crystal fiber optofluidic system, first proposed by Chen et al [9]. There, light and fluid highly interact in a microscale central hollow core surrounded by a cladding formed by an array of channels running along the entire length of the fiber (cm to m) (Figure 1a right diagram). As schematically depicted in Figure 1b, this configuration uniquely allows single-mode and low-loss propagation of light in a wide-range (UV to NIR) in a tiny liquid-filled core. Importantly, the system also allows *in situ* absorption spectroscopy, with sensitivities not attainable with conventional systems (Figure 1a left diagram). These unique features have motivated its use as highly-sensitive chemical sensors and microreactors for photochemistry and catalysis. Some examples of reactions are the photochemical conversion of Vitamin B_{12} [9], the photochemical and thermal *cis-trans* isomerization of azo dyes [10], homogenous catalyzed degradation of synthetic dyes (e.g. photo-Fenton) [11], and heterogeneous hydrogenation of ethane [12] and azobenzenes by metallic nanoparticles [13, 14].
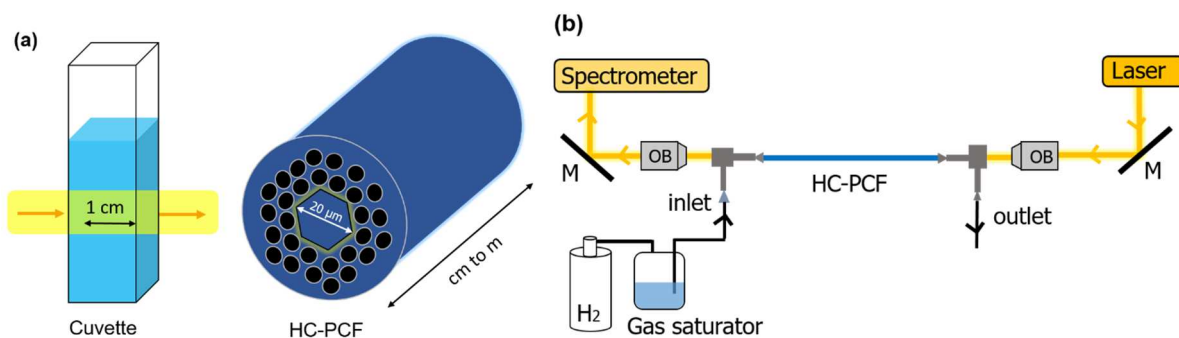
Figure 1. Schematic representation of a common 1 cm cuvette and a hollow-core photonic crystal fiber. (b) Hollow-core photonic crystal fiber microreactor setup. Scheme based on [13].

On the other hand, Booker-Millburn, Berry and co-workers, showed a simple methodology to carry out photochemical reactions under flow [47]. They used a FEP tubing wrapped around a UV lamp, in which the reaction solution flows (see an exemplary setup in Figure 2). This simple idea allowed for a continuous operated photochemical production and was basis for further applications, upgrading it to higher flow rates, temperatures, and more complex interactions. Among the reasons for its applications are: i. it provides an improved irradiation of the reaction mixture, ii. reliable scale-up, iii. improved reaction selectivity and reproducibility, iv. fast mixing, v. and further microreactor properties. For example, Seeberger et al., pioneered using the setup to develop reactions involving singlet oxygen as a reagent in several transformations, such as oxidations and cycloadditions [48]. Up to date, these continuous-flow reactors include, among others, applications in organic synthesis, materials science, and water treatment [6].
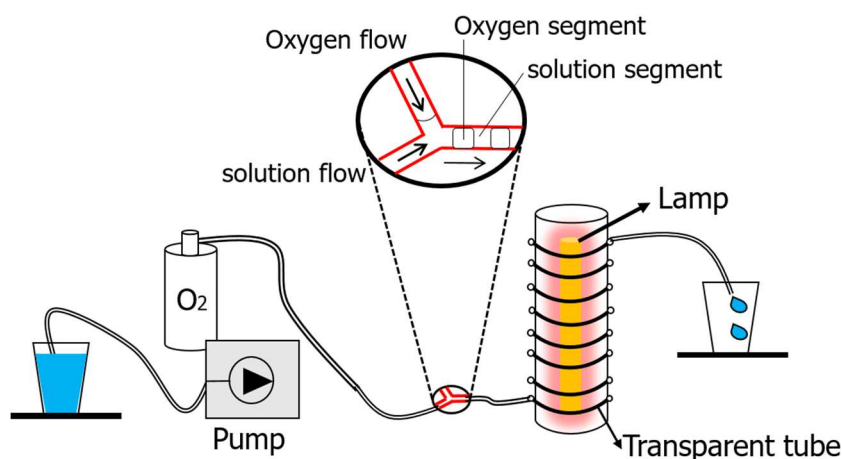

Figure 2. Schematic diagram of a Brooker-Milburn and Berry setup. Diagram based on [5].

2.2. Teflon AF based reactors

Teflon AF is an amorphous fluoroplastic made via copolymerization of the monomers tetrafluoroethylene (TFE), and 2,2-bis-trifluoromethyl 1-4,5-difluoro-1,3-dioxole (PDD) (see Figure 3). As a result, Teflon AF combines properties of both perfluorinated and amorphous polymers, which vary with the relative amount of PDD in their structure. Nowadays, Teflon AF is commercialized in two different grades by DuPont, such as the Teflon AF-1600 and 2400 with 64 and 83 mol% of PDD respectively. Some of the outstanding properties of this Teflon are summarized in

Table 1. In general, Teflon AF exhibits excellent chemical stability similar to commonly used polymer as polytetrafluoroethylene (PTFE), perfluoralkoxy, and FEP. It possesses also a good thermal stability with very small weight loss at temperatures, as high as 400 °C. The dielectric constant of Teflon AF is the lowest for a polymer known (1.89 to 19.3). Moreover, as an amorphous polymer, it exhibits excellent optical properties with a transmission (transparency) better than 90 % along the UV, visible, and near-IR spectrum. In this sense, it also possesses the lowest refractive indexes for any polymer family (e.g. $\eta_{Teflon\ AF-1600} = 1.31$ and $\eta_{Teflon\ AF-2400} = 1.29$, $\eta_{PTFE} = 1.35\text{-}1.38$). Interestingly, Teflon AF is an ultrahigh-free-volume glassy polymer [49], therefore exhibits an immense gas permeation for most gases (e.g. CO_2, H_2, O_2, SO_2, NO_x). For instance, it has an oxygen permeation rate of 99000 centi-Barrers (cB) compared to 420 cB of PTFE (see more examples in Table 2). Finally, it presents also good mechanical properties, and insolubility in water and other normal organic solvents [50, 51].
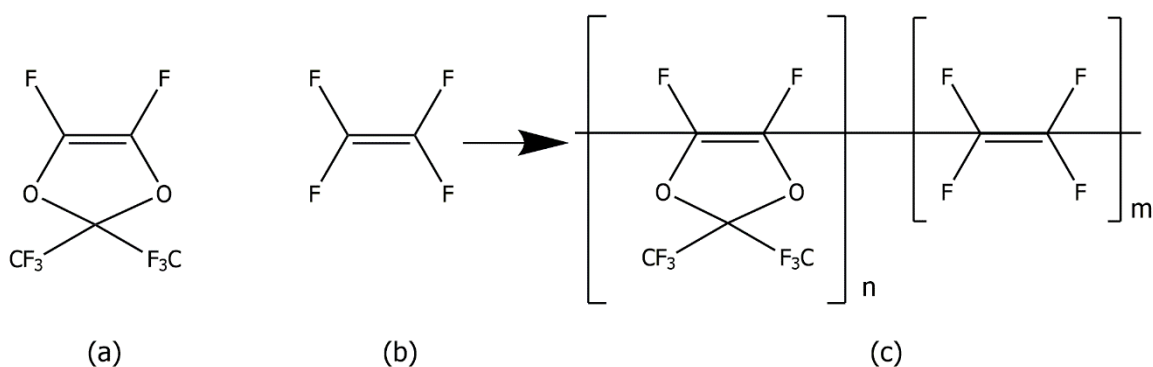

Figure 3. Copolymerization reaction for the synthesis of Teflon AF (c). (a) 2,2-bis-trifluoromethyl 1-4,5-difluoro-1,3-dioxole, and (b) tetrafluoroethylene.

Table 1. Properties of Teflon AF-1600 and 2400 [50, 51].

Property	AF-1600	AF-2400	Unit
Fraction of PDD	64	83	mol %
Density	1.8	1.7	g cm^{-3}
Thermal Conductivity	0.07	0.05	W m^{-1} K^{-1}
Glass transition temperature	160	240	^{o}C
Refractive index	1.31	1.29	-
Effective transmission (UV-NIR)	> 95		%
Yield Strength (23 ^{o}C)	27.4	26.4	MPa
Tensile Strength (23 ^{o}C)	26.9	26.4	MPa
Hardness (23 ^{o}C)	103	97.5	Rockwell
Thermal stability	260	260	^{o}C

Table 2. Gas permeability of Teflon AF and PTFE [52].

Gas	AF-2400	PTFE	Unit
Carbon dioxide	210	0.90	
Hydrogen	170	0.74	10^{-12} m^3 s kg^{-1}
Oxygen	74	0.32	
Nitrogen	37	0.11	

Due to these outstanding properties, Teflon AF polymer tubes have been widely applied not only in the area of optical sensing, as in the so-called liquid core waveguide sensors, but also as membrane reactors (i.e. tube-in-tube reactors) for developing a number of gas-liquid chemical reactions in the last two decades. Thus, due to the importance for this study, these two technologies will be reviewed separately in the next sections.

2.2.1. Teflon AF as optical sensor: Liquid core waveguides

The light guidance of LCWs is based on the total internal reflection phenomenon (TIR). Therefore, the refractive index of the liquid fluid needs to be higher than the refractive index of the core (tube), which confine the light [53]. As mentioned above, Teflon AF possess the lowest refractive index of a polymer known (1.29-1.31). Thus, light can be confined within the capillary via total internal reflection with almost most solvents even water (η =1.31) (see

Figure 4 for a typical setup) [25]. In general, in order to TIR occurs, a ray of light must travel from a material with higher refractive index (η_1) to one of a lower (η_2) and must hit the medium interface with an angle (∅) greater than the critical value (Equation (1)). Figure 4 inset depicts the TIR phenomena inside of a water-filled Teflon AF tube.
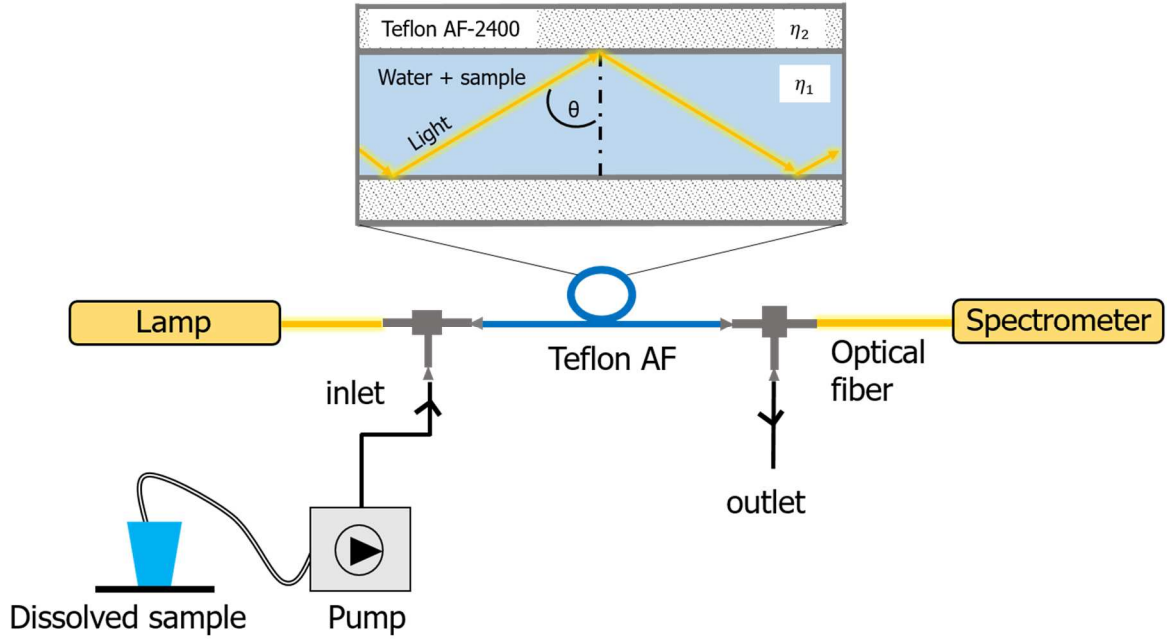

Figure 4. LCWM typical setup [22]. Inset: total internal reflection phenomenon for light transmission in a water-filled Teflon AF tube.

$$\emptyset = cos^{-1}\left(\frac{n_1}{n_2}\right) \tag{1}$$

Another optical effect occurring within a water-filled Teflon AF tube system is the absorption of light along the tube. LCWs successfully increase the signal-to-noise ratio by increasing the optical path-length compared to cuvette standard cells. This ability to sense lower concentrations is explained by the Beer-Lambert law (Equation (2)). The increment of the path-length increases the light attenuation by both absorption and light losses. In this sense, the optimum length will depend on the source, detector, fiber type, and tube diameters.

$$I = I_o * 10^{-\varepsilon bc} \tag{2}$$

where: I is the intensity of transmitted light, Io the intensity of incident light, ε the molar absorption coefficient (L mol^{-1} cm^{-1}), b the optical path-length (cm), and c is the solution molar concentration (mol L^{-1}).

Applications

According to Dasgupta et al. [29], pioneers in this technology, and recently reviewed by Páscoa et al. [28], LCW technology has found many applications in different light-dependent research areas. LCW long-path absorption spectrometry has been widely used for trace analysis in natural water and marine chemistry. Among others, the detection of metallic cations, organic, and inorganic compounds are the most frequent. Examples of analytes are hydrogen sulfide, iron, nitrate, nitrite, phosphate, chromium-molybdenum, copper, total organic carbon, colored dissolved organic matter, and others [22, 24, 28, 54-56]. In addition, the possibility to measure gaseous analytes dissolved in a liquid-phase, such as CO_2, Cl_2, H_2S, NO_2, O_3 is reported. For instance, Tao and Le [57], recently reported a UV absorption LCW spectrometer for monitoring a water ozonation process. The optical design was similar to the one depicted in Figure 4, but with the Teflon AF submerged in a water bath bubbled with ozone. Ozone permeates through the Teflon AF membrane, and further dissolves into the water-filled capillary, which is monitored by UV spectroscopy at 254 nm. Similarly, Liu et al. published an interesting *in situ* spectrometer for measuring dissolved inorganic carbon in seawater [58]. They took advantage of the capacity of the Teflon AF tubes to permeate carbon dioxide into the core, as already demonstrated by Byrne et al. [59]. As a result, the hydrophobic LCW acted not only as a long path-length optical cell, but also as a CO_2 equilibrator. For this purpose, they used a polyether ether ketone (PEEK) polymer rod to encapsulate the LCW and introduce acidified water in the gap between the rod and the fiber. Interestingly, two years later, Wang et al. improved the setup by adding *in situ* pH analysis applying a counter-flow for reducing the equilibration time [60]. Less applications have been found in areas, such as chemiluminescence, electrophoresis/fluorescence detection [25], and Raman spectroscopy [27].

2.2.2. Teflon AF as Tube-in-Tube gas-liquid contactor

The tube-in-Tube reactor concept was first proposed in 2010 by Ley's group at University of Cambridge, as a novel method for developing gas-liquid reactions on the microscale [61]. It consists of a permeable Teflon AF tube (inner) embedded in a non-permeable PTFE tube (outer) (see scheme in Figure 5). Generally, the liquid-phase is pumped into the inner tube and gas is

pressurized at the annulus between the inner and outer tube. Thus, gas permeates through a Teflon AF membrane and subsequently dissolved in the liquid until equilibrium is reached very quickly (see inset in Figure 5). In the last years, Ley and co-workers and several other groups extended the studies from non-reactive gas-liquid mass transfer to study of reactions with homogenous and heterogeneous catalysts (See Table 3 for a chronologically list of the most notable examples).
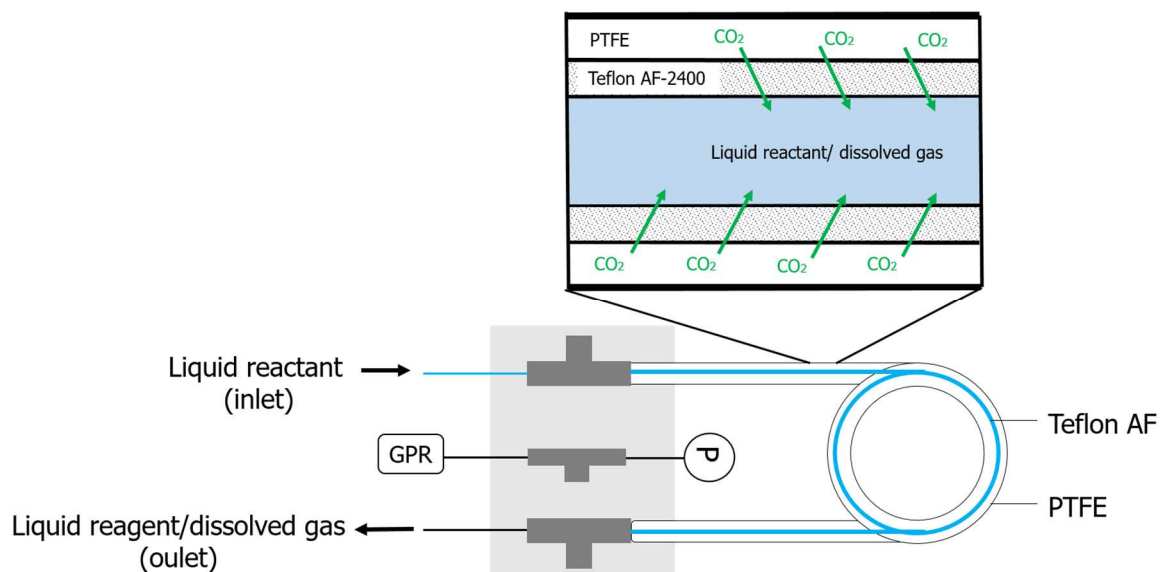

Figure 5. Schematic of the concentric tubular "Tube-in-Tube" gas-liquid reactor. GPR: gas back-pressure regulator, P: pressure indicator. Figure based on [17]. Inset: gas permeation through the Teflon AF membrane.

Table 3. Chronological summary of applications developed within tube-in-tube contactor systems.

Ref.	Study	Highlights
[61]	Ozonolysis of alkenes via gas-to-liquid transfer.	✓ First gas-liquid contact example.
[15]	Synthesis of carboxylic acids using CO_2	• Safe process, which not exceeds a gas volume of 2 mL. • Effective delivering of carbon dioxide into the flow stream. • Straightforward scale-up of reaction, thus carboxylic acid was prepared on a multigram scale.
[18]	Homogeneous and heterogeneous hydrogenation of ethyl cinnamate using Crabtree's and PdC catalysts respectively.	✓ Conversion in pressure dependency studied (10 to 30 bar). ✓ Conversion in residence time dependency studied (until 150 s).
[62]	Paal-Knorr pyrrole formation and gas concentration measurements.	• Synthesis of substituted pyrroles from 1,4-diketones (yields 33-100 %). • Efficient thermal contact, and rapid heated or cooled, which leads to higher rates of gas uptake.
[63]	Aerobic Anti-Markovnikov Waker oxidation.	✓ Efficient flow synthesis for arylacetaldehydes from functionalized styrenes. ✓ Simple and selective crystallization of the desired products by formation of bisulfite products. ✓ Highly control of oxygen delivering thanks to the two Tube-in-Tube system coupled.
[64]	Mass transport and reaction calculations.	• First model for analytically and numerically computing of gas and liquid concentration profiles. • Simulative approach for the reactor scalability.
[21]	Oxidation of Benzyl alcohol.	✓ 1 wt% Au-Pf/TiO_2 particles packed inside the PTFE external tube. ✓ Improved conversion compared to oxygen pre-saturated systems.
[65]	Automated measurement of gas solubility in liquids.	• Solubility measured by the steady-state flux balance of gas into the liquid. • Ultra-fast measurements (2-5 min) compared to 4-5 h by conventional methods. • Gas tested (H_2, N_2, O_2, CO_2) in several liquids (methanol, heptane, and methylstyrene)

2.3. Heteropolyacids for biomass to formic acid oxidation

The first case study will be on the catalysed biomass oxidation towards formic acid and the state of the art to this application is briefly summarized. Catalytic partial oxidation employing molecular oxygen is one important pillar of today's industrial chemistry and future sustainable scenarios. Partial oxidation is e.g. studied for conversion of biomass into valuable energy carrier molecules, platform chemicals, and other bio-based products. Formic acid (FA), for instance, is a widely used commodity in the chemical, textile, leather, pharmaceutical, agricultural, and rubber industries. Recently, also finding application as an efficient hydrogen storage compound [66]. Thus, the production of FA from biomass has gained in attention and has been extensively studied in the last years. Among several approaches, such as hydrothermal oxidation (at high temperatures and pressures) [67], integrated homogeneous and heterogeneous catalytic systems based on ruthenium, or V-substituted phosphomolybdic acid catalysts [68, 69], and photo-and electro-activated systems [70], the use of polyoxometalates (POMs) catalysts have emerged as a promising method to transform carbohydrate-based biomass, as recently demonstrated by Albert et al., in the so-called OxFA Process [71]. Due to the importance for this study, this process will be discussed in more detail below.

2.3.1. OxFA process

Wölfel[72] and Albert[73] fully developed a catalytic system for the selective conversion of biomass to formic acid and CO_2, operating at mild temperature conditions (< 373 K), and using molecular oxygen or air as environmental benign oxidants (> 20 bar). A wide range of water-soluble substrates, such as glucose, fructose, sorbitol, gluconic acid, *etc.*, but also raw water-insoluble biomasses like beech, and spruce wood have been successfully converted. Moreover, as both products separate nicely into liquid and gas phases, tedious separation process are avoided, making the so-called OxFA process an interesting alternative compared to other biomass technologies.

The OxFA process can be divided in the acid hydrolysis if water-insoluble substrates are present and then the catalytic cycle consisting of: i. oxidative cleavage of C-C bonds in the model substrate, which also involves the reduction of the catalyst (r_{red}), and ii. re-oxidation of the reduced catalysts by molecular oxygen (r_{ox}) (see Figure 6). Hence, from these three key components the minimum requirements for a suitable catalyst can be derived. The catalysts should (a) be able to reoxidize with molecular oxygen, (b) promote controlled C-C bond cleavage, (c) stay active in acidic solutions, (d) have a redox potential between the FA and O_2 values, and (e) stay unalterable with the presence of possible impurities in raw biomass [74].
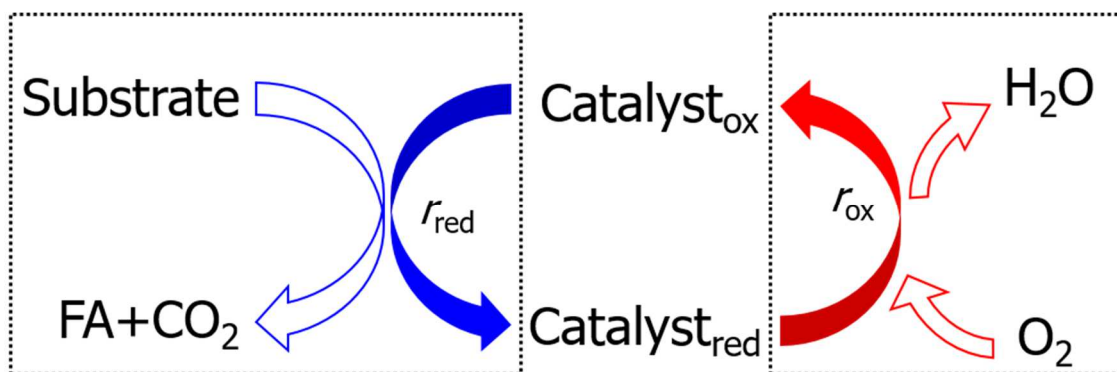
Figure 6. Schematic illustration of the HPA-n redox cycle in the "OxFA process". (a) Substrate oxidation and catalyst reduction, and (b) catalyst reoxidation.

Among other Polyoxometalate active structures applied, like Wells-Dawson, Lindqvist, and Anderson [71], the authors have mostly reported studies using Vanadium-substituted heteropolyacids of the Keggin-type as catalysts that fulfil the above mentioned requirements [74-78]. Vanadium-substituted HPA catalysts have several advantages that make them environmentally and economically attractive for biomass oxidation. They have a very strong Brönsted acidity, fast reversible multi-electron redox transformations under rather mild conditions, high solubility in various solvents, and good resistance against hydrophilic or oxidative degradation in solution.

In general, the Keggin-type heteropolyacids are typically represented by $[XY_mM_{(12-m)}O_{40}]^{(3+m)-}$, where X is the heteroatom (Si^{4+}, P^{5+}, etc.), M the addendum atom (M= Mo^{6+}, W^{6+}), and Y the possible substitutes of M (Y= V^{5+}, Co^{2+}, Zn^{2+}, Ta^{5+}, Nb^{5+}, etc.). Roughly, the Keggin anion is composed of a central tetrahedron XO_4 surrounded by 12 edge- and corner-sharing metal-oxygen octahedra MO_6 (see Figure 7a) or partial substituted by YO_6 structures, as in a HPA-2 catalyst (see Figure 7b) [79, 80].
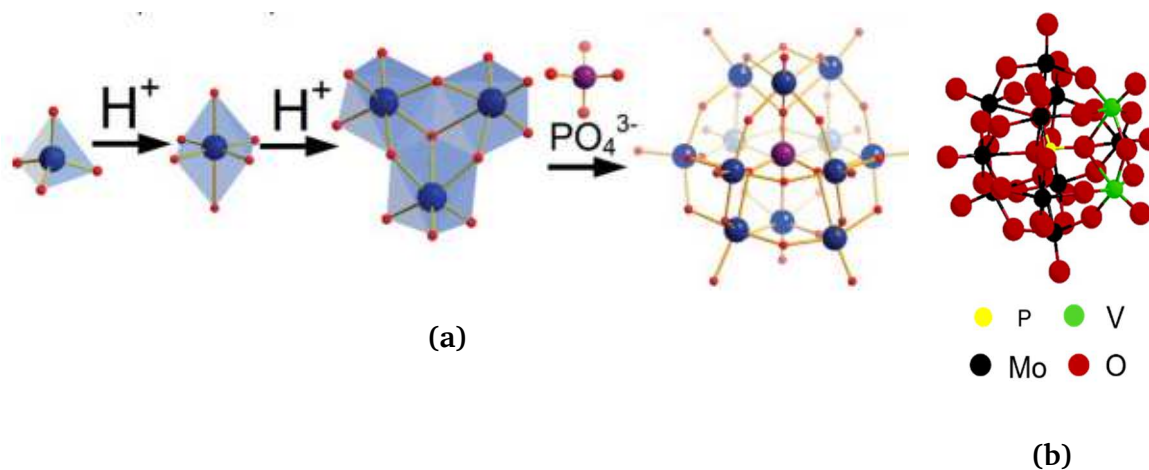
$$12\,WO_4^{2-} + PO_4^{3-} + 24H^+ \rightarrow [PW_{12}O_{40}]^{3-} + 12H_2O \tag{3}$$
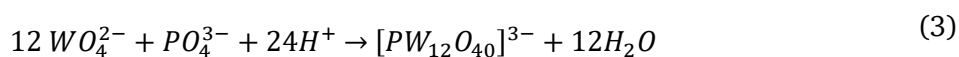
Figure 7. (a) Formation of the archetypal Keggin anion [PW12O40]³⁻. Up: Oligo-condensation reactions of tungsten ions in acidic media in the presence of phosphate templates. Bottom: Schematic self-assembly of the Keggin anion. Diagram reprinted with permission from [79]. Copyright Royal Society of Chemistry. (b) Structure of a two times V-substituted heteropolyacid $[PV_2M_{(10}O_{40})]^5$ complex (HPA-2). Diagram based on [81].

Furthermore, Figure 8 shows the reaction pathway for the Vanadium-induced glucose oxidation by molecular oxygen to formic acid in aqueous media, suggested by Li et al [82]. The electro transfer mechanism gives products, such as glycolaldehyde, glyoxal, and glyceraldehyde. Then, they are further oxidized to the formation of formic acid and CO_2.
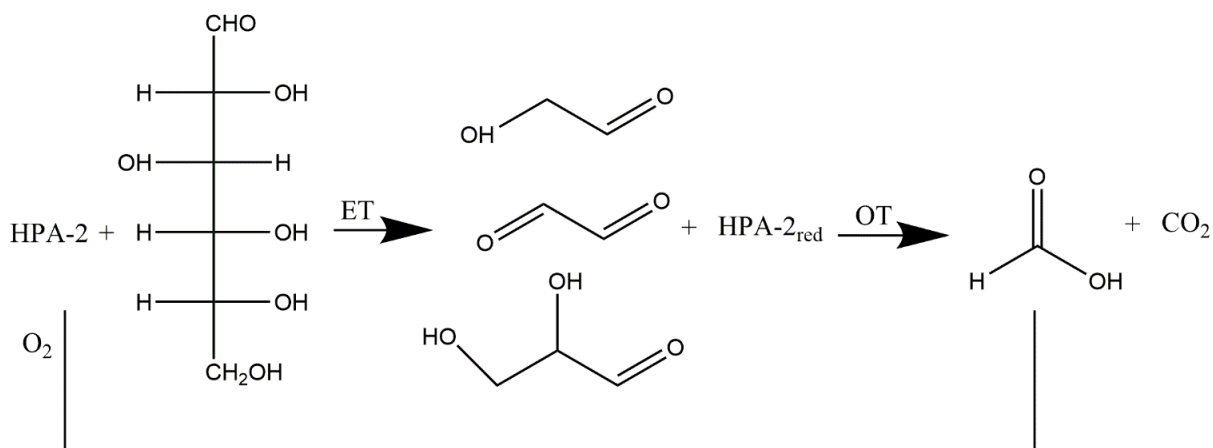
Figure 8. Proposed possible pathway for glucose oxidation catalyzed by HPA-2 reaction mechanism based on [82].
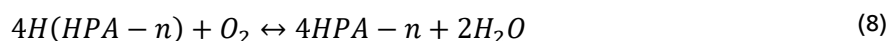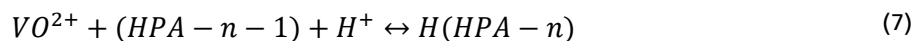
According to several authors [76, 80, 83-85], the reaction mechanism could be explained by the presence of two active species. In diluted acid solutions the HPAs suffer degradative dissociation (Equations (4) and (5)) with the formation of defect heteropoly species (lacunary

species: HPA-n-1) and monomeric pervanadyl (VO_2^+) ions without degree of reduction ($m = 0$). The latter, due to higher oxidation potential than the parent lacunary species, seem to be the principal active species in highly substituted catalysts. In turn, once the species has been reduced ($m = n$), the free vanadyl (VO^{2+}) ion cannot be oxidized by molecular oxygen, therefore, the reduced vanadium should return to the heteropolyanion structure by an electron transfer interaction, to be eventually reoxidized by O_2 via a multielectron-transfer mechanism (Equations (6) and (8)). Even though the complexity of the systems involved make difficult to clearly understand the mechanism of reoxidation, it is known that oxygen is a rather poor one-electron oxidant. Thus, the reoxidation of HPA-0 and HPA-1 would be unfavourable.

Dissociation equilibria:

$$(HPA - n)_{m=0} \leftrightarrow VO_2^+ + (HPA - n - 1)_{m=0} \tag{4}$$

$$(HPA - n)_{m=n} \leftrightarrow VO_2^+ + (HPA - n - 1)_{m=n-1} \tag{5}$$
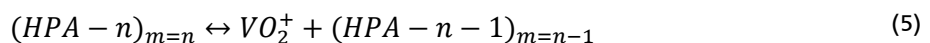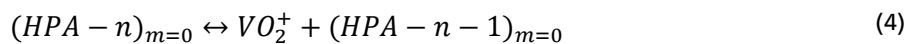
Reoxidation equilibria:

$$VO^{2+} + HPA - n + H_2O \leftrightarrow VO_2^+ + (HPA - n) + H^+ \tag{6}$$

$$VO^{2+} + (HPA - n - 1) + H^+ \leftrightarrow H(HPA - n) \tag{7}$$

$$4H(HPA - n) + O_2 \leftrightarrow 4HPA - n + 2H_2O \tag{8}$$

As mentioned above, while vanadium substitution is known to show an influence on the overall activity (see Table 5), experimental observations show a contrasting behavior. On the one hand, non-and mono-substituted catalysts have not shown any significant catalytic activity, presenting negligible yields with selectivity towards the formation of CO_2. This, even at high oxygen partial pressures and temperatures applied (> 20 bar, 90 ℃). On the other hand, higher V-substituted catalysts showed a remarkable activity, reaching a complete substrate conversion within a few hours (8 h, at > 20 bar oxygen pressure, 90 ℃, and 1000 rpm stirrer speed), and a good selectivity to FA (max. 61 % with glucose as substrate and $H_8[PV_5Mo_7O_{40}]$ as catalyst [76], see Table 4 for other catalysts). Differences in activity were up to now related to the reoxidation rate of each catalyst, nevertheless, a full study on the reduction and reoxidation kinetics for varying vanadium substitution content is missing. Visual observation of non-and mono-substituted catalysts solutions, after reaction, evidenced the presence of a dark blue colour

mixture, which is associated to the presence of heteropoly-reduced species (i.e. $r_{red} >> r_{ox}$) [71]. Whereas V-substituted catalysts stayed stable in their oxidized form during the experiments (yellow-orange mixture, $r_{ox}>>r_{red}$). All in all, further insights how vanadium substitution influences the redox cycle is required. *In situ* UV/Vis spectroscopy is suitable for obtaining further insights onto this gas-liquid reaction, as the concentration of the oxidized and reduced form of the catalyst can be followed.

Table 4. Oxidative conversion of glucose with different V-substituted heteropolyacids [76].

Catalyst	Combined yield FA+ CO2 (%)	Selectivity FA+ CO2 (%)
HPA-0	10	40:60
HPA-1	12	50:50
HPA-2	91	52:48
HPA-3	100	56:44
HPA-4	97	54:46
HPA-5	94	61:39
HPA-6	97	58:42

Table 5. Comparison of the catalytic conversion of different substrates using HPA-2 and HPA-5 catalysts [86].

Substrate	Reaction rate [mol L^{-1} h^{-1}]		
	HPA-0 and 1	HPA-2	HPA-5
Glucose	-	7.09	13.11
Cellobiose	-	1.68	2.93
Sucrose	-	12.22	15.02

2.4. Methylene Blue degradation

The second case study will be on the complex degradation network of Methylene Blue and the state of the art is briefly summarized. Methylene blue is a dark-green crystalline compound that dissolves in water to form a deep-blue solution. Since its first production [87], MB enjoys widespread industrial applications, such as dye for hair and textiles, ISO test pollutant in semiconductor photocatalysis, photosensitizer for singlet oxygen generation, antioxidant and antiseptic, stain for fixed and living tissues, antidote to cyanide and nitrate poisoning, and

treatment for malaria [88, 89]. However, this versatility makes it also a highly complex molecule, with some of its interactions remaining ambiguous. Most of the problems arrive, as MB readily decomposes reversible and irreversible (see scheme in Figure 9) in the presence of different reaction conditions. Due to the importance for this study, some of the most common reversible and irreversible degradation pathways of MB are discussed below.
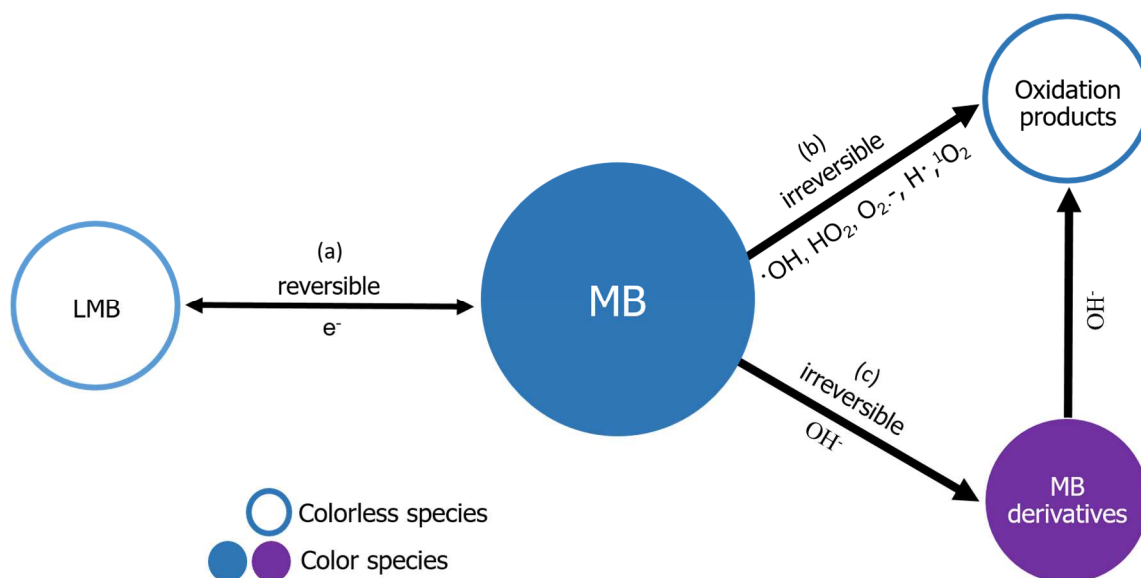

Figure 9. Scheme of different methylene blue degradation pathways: (a) Reversible redox cycle, (b) partial oxidation to non-visible products, and (c) mono-deamination and N-demethylation successively degradation. (LMB= leuco-methylene blue).

2.4.1. Reversible degradation

The degradation is reversible if the addition of oxygen to the anaerobic system oxidizes the MB-reduced form (leuco-methylene blue (LMB), see Table 6 entry 8)) to MB (Equation (11)). The leuco form can be obtained with the addition of one of almost any number of reducing agents, e.g. ascorbic acid, sodium borohydride, sodium dithionite, *etc.*, via an electron-transfer mechanism (Equation (9)) [90]. MB can also be reduced to its leuco form by the indirect oxidation of glucose in alkali, as in the well-known blue-bottle experiment (see scheme in Figure 10). Moreover, this process could also take place via interaction of a photoactivated catalyst together with a simple electron donor (SED) compound in anaerobic conditions (Equation (10)) [91].
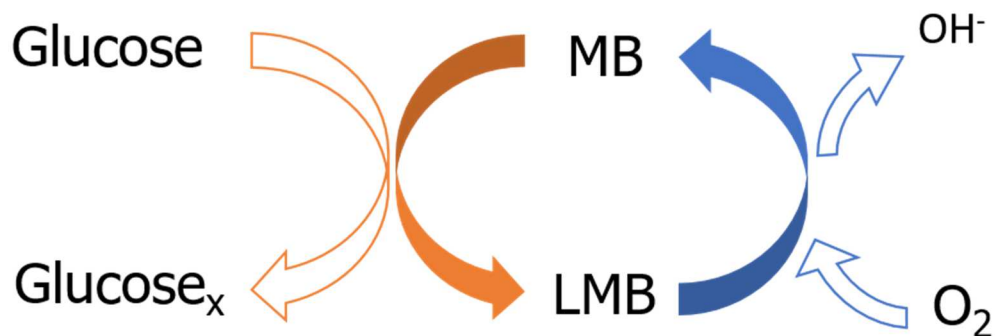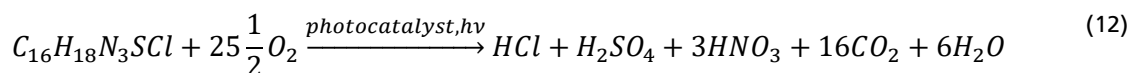
Figure 10. Schematic representation of the methylene blue redox cycle, as in the so-called blue bottle experiment. MB: methylene blue, LMB: leuco-methylene blue.
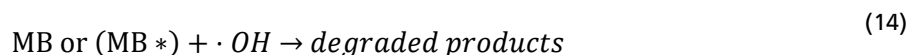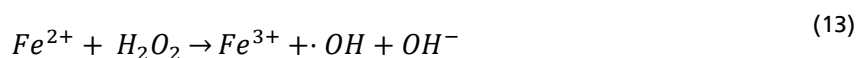
Reversible cycle:

$$MB \xrightarrow{H^+,\, 2e^-} LMB \tag{9}$$

$$MB + SED \xrightarrow{photocatalyst,\, h\upsilon} LMB + SED^{2+} \tag{10}$$

$$4LMB + O_2 \rightarrow 4MB + 2H_2O \tag{11}$$

Irreversible oxidation (photocatalyst in aerobic conditions overall reaction):

$$C_{16}H_{18}N_3SCl + 25\frac{1}{2}O_2 \xrightarrow{photocatalyst,\, h\upsilon} HCl + H_2SO_4 + 3HNO_3 + 16CO_2 + 6H_2O \tag{12}$$

Irreversible oxidation (Catalyst and oxidant):

$$Fe^{2+} + H_2O_2 \rightarrow Fe^{3+} + \cdot OH + OH^- \tag{13}$$

$$MB \text{ or } (MB*) + \cdot OH \rightarrow degraded\ products \tag{14}$$

2.4.2. Irreversible degradation

Irreversible degradation can be divided into two categories leading to different degradation-products: i) colour and ii) colourless derivatives (see scheme in Figure 9). On the one hand, colourless products normally result from the partial oxidation, e.g. the sulfoxide form, or the total oxidation of MB to CO_2 and H_2O, while in contact with highly oxidative radicals, such as $\cdot OH$, $\cdot HO_2$, $O_2{\cdot}^-$, $H\cdot$, and others (Equations (12) and (14)). The origin of these oxidative radicals

could be various. From advanced oxidation processes (AOPs), such as UV/H_2O_2, Fenton-and photo-Fenton reaction [92]), UV-Vis heterogeneous catalysis based on semiconductor and/or metallic materials (e.g. TiO_2, WO_3, Au/Ag NPs, Au-WO_3, *etc.* [93, 94]), and through photosensitizing interactions. On the other hand, studying the presence of coloured intermediates during the MB-degradation have gained special attention lately. They are of interest as they alter the characteristic absorption spectra of MB, affecting e.g. reliable kinetic studies, or the selectivity of the degradation process. This type of irreversible degradation has been observed mostly in heterogeneous photocatalytic experiments, but also in dye decomposition in alkaline solutions. Due to the importance for this study, some of the interactions numbered before will be in more detailed discussed below.

MB photosensitizing cycle

Superoxide ions and singlet oxygen are powerful reactants, which could irreversible oxidize MB (photobleaching) that is unaffected by oxygen in its normal state. Interestingly, both can be generated by MB itself through a photosensitizer (PS) cycle under light irradiation in aerobic conditions. MB exhibits four important properties making it an efficient PS: i. high absorption coefficient in the spectral region of light excitation (550-700 nm), ii. a triplet state with high energy (133 kJ mol^{-1}), iii. high quantum yield of the triplet state (0.52), and iv. long triple state lifetimes ($> 1\ \mu s$). Therefore, in a light irradiated oxygen environment, the excited triple state (MB*(3)) could interact with oxygen by two different mechanisms: Type I: electron-transfer between the sensitizer and a substrate, yielding free radicals, which could further react to oxygen to form superoxide ions, and Type II: by the direct collision, energy transfer, of (MB*(3)) with the triplet oxygen for the formation of singlet oxygen (see Figure 11 and Equations (15) to (20). Even though these are two competing mechanisms, the production of singlet oxygen is approximately 100 times faster compared to the production of superoxide anion. Particularly, in MB systems superoxide production is considered a side reaction, while the singlet oxygen mediated oxidation is usually the dominant pathway [95, 96].

$$PS(S_0) \xrightarrow{h\upsilon} PS(S_1) \xrightarrow{k_{ISC}} PS(T_1) \tag{15}$$

$$PS(T_1) +\ ^3O_2 \xrightarrow{k_{en}} PS(S_0) +\ ^1O_2 \tag{16}$$

$$PS(T_1) \xrightarrow{k_r} PS(S_0) + h\upsilon'' \tag{17}$$

$$PS(T_1) \xrightarrow{k_{nr}} PS(S_0) \tag{18}$$

$$PS(T_1) + O_2 \xrightarrow{k_{dO2}} PS(S_0) + O_2 \tag{19}$$

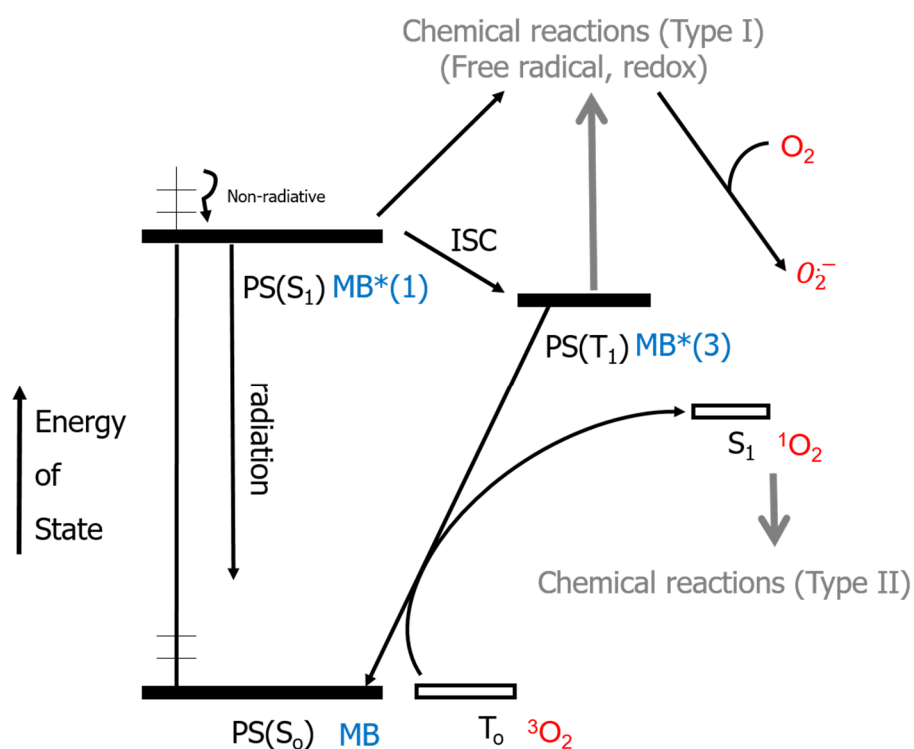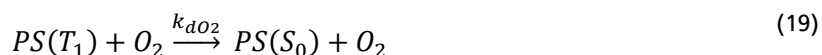$$PS(T_1) + O_2 \xrightarrow{k_{et}} PS^+ + O_2^- \tag{20}$$
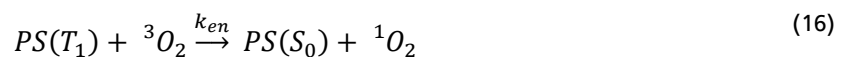
Figure 11. Generation of excited photosensitizer (PS) states and reactive oxygen species, representing all possible reactions described in (Equations (15) to (20)). Diagram based on [97].

From Figure 11, $S_{0,1}$ represents the singlet ground and first excited state respectively, T_1 the first excite triplet state, k_{ISC} is the rate constant of intersystem crossing, k_{en} the rate constant of energy transfer, $k_{r,nr}$ represent the rate constant of radiative and non-radiative processes, $^1O_2$ represents singlet oxygen, and $^3O_2$ ground state triplet oxygen.

Thermal degradation in alkali

It is known that the nucleophilic attack of OH⁻ ions on MB initiates a series of reactions giving a number of new, closely related MB substances. In this sense, liquid-phase analysis studies,

principally developed by Katafias et al, showed the presence of the protonated forms of Methylene Violet Bernthsen (MVB), Azure A, B, C (AA, AB, AC respectively), and Thionin (TH) as degradation products of MB in alkaline and alkaline hydrogen peroxide solutions. Possible side reactions leading to these compounds could be the N-demethylation of MB, which leads to AA, AB, AC, and TH. Also, the mono-deamination can take place to result in MVB (Table 6 entries 2-7). Nevertheless, the mechanism of reaction remain uncertain, therefore just some probable simplified mechanisms have been published by now (see Figure 12a) [98]. Other studies have also reported the presence of immiscible/lipophilic species, i.e. toluene-soluble, red/pink species, as products during the MB degradation in alkali. According to S. Basu et al [99], these species should be N-hydroxy adduct of MB (MB-OH). However, these results have been discussed by A. Mills et al [89], arguing that the predicted visible spectrum of MB-OH is colorless, and not red. Therefore, according to the authors those species should be related to the deprotonated forms of the mono-deaminated and N-demethylated derivatives present in the aqueous media (see diagram in Figure 12b).
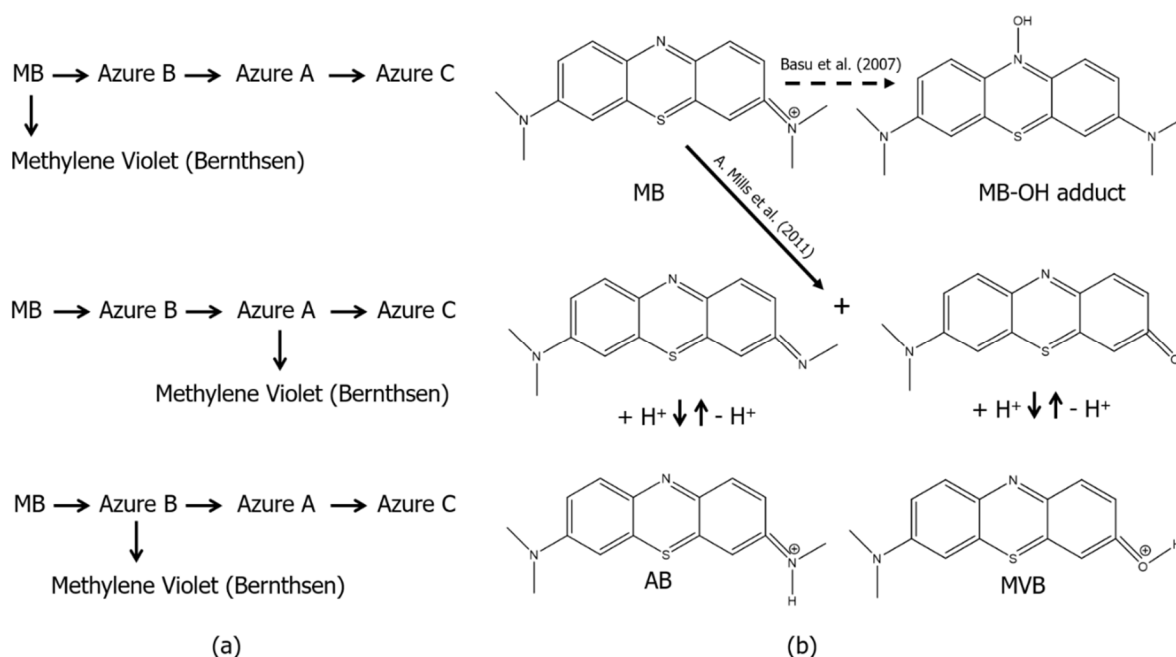
Figure 12. (a) Methylene blue and its mono-deaminated and N-demethylated derivatives [98]. (b) MB further reactions in alkali: dash-lines according to [99], solid lines to [89] .

MB photoinduced degradation

As mentioned before, MB irreversible degradation under UV/Vis- semiconductor and/or metallic systems has been widely investigated as efficient AOPs (Equation (12)). However,

recently many studies have shown the production of N-demethylated intermediates, such as AA, AB, AC, and TH (entries 3-6 in Table 6) together with the oxidized species. According to T. Zhang et al., as weak electron-donor substituents, methyl groups can facilitate attack on MB by electrophilic species during the demethylation process [100]. They suggested that N-demethylation of MB happens in a step wise manner as depicted in Figure 13a. The presence of these new species alters the characteristic MB absorption spectra, showing a clear blue or hypsochromic shift to higher frequencies. Accordingly, many authors have confirmed the presence of most of these species, e.g. by mass spectroscopy (MS), and high-performance liquid chromatography (HPLC) separation, and graphical and/or analytical spectra deconvolution, in a variety of photooxidation processes [94, 101-103].
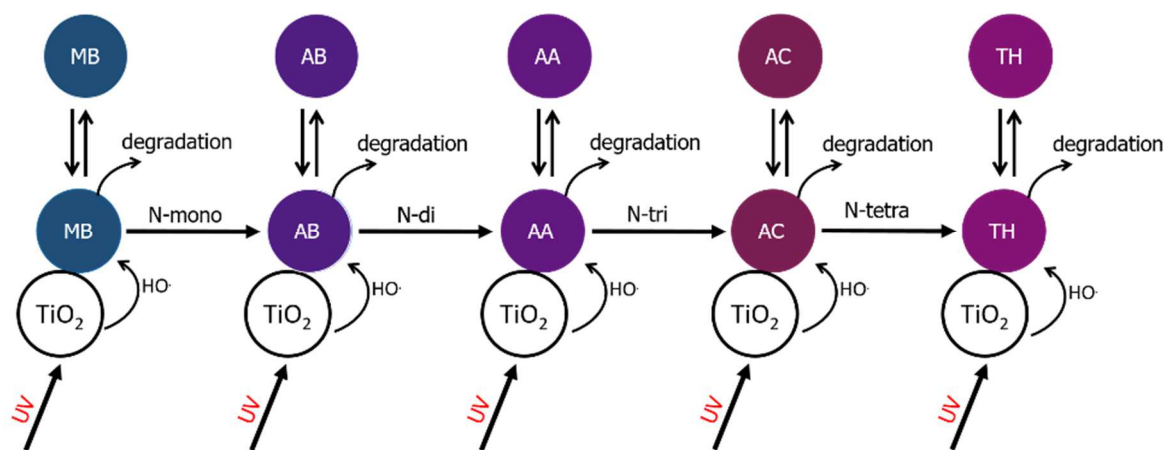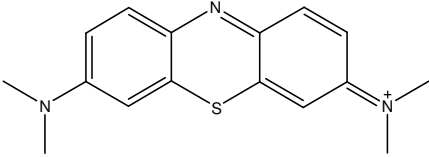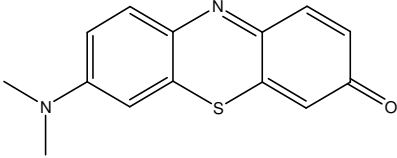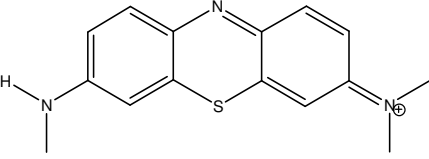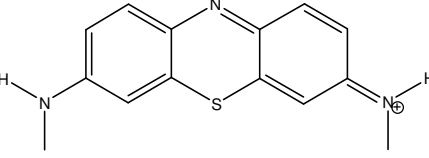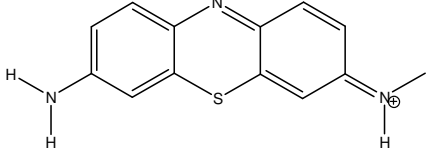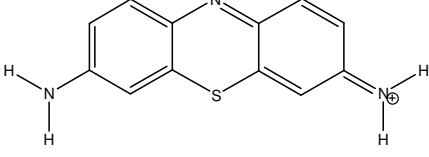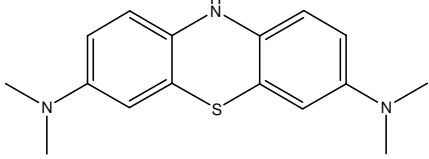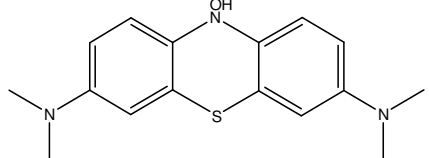
Figure 13. (a) Scheme describing the successive N-demethylation of MB and the dynamic equilibrium of MB and new species between the bulk solution and the photocatalysts during UV light irradiation. Diagram based on [100].

Table 6. Molecular structure, and absorption maxima of methylene blue and its possible degradation derivatives dissolved in water ([a] Absorption maxima of deprotonated species measured in acetone)[89].

Entry	Substance	Molecular structure	Absorption maxima (nm)
1	Methylene Blue (MB)		664 (cation)
2	Methylene Violet Bernthsen (MVB)		610 (cation) 520 (neutral)[a]
3	Azure B (AB)		645 (cation) 503 (neutral)[a]
4	Azure A (AA)		628 (cation) 500 (neutral)[a]
5	Azure C (AC)		615 (cation) 488 (neutral)[a]
6	Thionin (TH)		602 (cation) 487 (neutral)[a]
7	Leuco-Methylene blue (LMB)		256 (neutral)
8	Methylene blue-OH adduct [99] (MB-OH)		520 (neutral)

As already summarized, MB goes through different degradation pathways, e.g. in alkaline media, aerobic and/or anaerobic conditions, under light exposition, among others, making most

of the reaction systems, involving MB, extremely complex. Up to now, authors have studied the degradation patterns separately without applying corrections at evaluating the reaction under UV/Vis spectroscopy. Moreover, in many cases, they have just ignored the presence of degradation species [102], making some MB investigations ambiguous (e.g. for kinetic investigations). Thus, further studies, which could shed light onto the photo-and non-photo degradation processes faced by MB when working under different conditions, are still needed.

2.5. Synthesis and stability of colloidal silver nanoparticles

The third case study is on the synthesis and stability of colloidal Ag nanoparticles and the state of the art is briefly summarized. Due to their exceptional optical, electrical, antimicrobial, antifungal, and antiviral properties, silver nanoparticles have found many applications in today's life, and certainly in future scenarios. Among a broad-spectrum of products including nanomaterials, AgNPs are by far the most commercialized ones [104]. However, it has been widely proved that some of these products release nanoclusters into the environment along their complete product lifecycle (i.e. manufacture, useful life, and final disposal). Therefore, there is a big concern that their intrinsic toxicity would affect natural microbial communities, causing a significant impact on the environment. AgNP toxicity properties arise principally from their tendency to suffer a number of chemical and photochemical transformations depending on their synthesis procedure and surrounding environment. For these reasons, their most common synthesis methods, and most studied chemical interactions, will be discussed in the next sections.

2.5.1. Synthesis of colloidal silver nanoparticles

In general, AgNPs can be synthesized by physical, chemical, and recently introduced biological synthesis methods.

Physical methods include evaporation–condensation and laser ablation techniques. The uniformity of NPs distribution, and absence of solvent contamination (i.e. chemical reagents) are some the advantages of these methods compared to chemical processes. However, particle synthesis by evaporation using tube furnace at atmospheric pressure could also involve high amounts of energy, time, and space consumption. On the other hand, laser ablation of metallic bulk materials (see scheme in Figure 14a) in solution have shown to be an efficient and flexible system to obtain NPs of different sizes, shapes with narrow distributions. As demonstrated by Tsuji et al. [105, 106] and Hajiesmaeilbaigi et al. [107], these properties are highly dependent

on several parameters, such as light wavelength, duration of the laser pulses (femto-, pico-, nanosecond regime), laser fluence, ablation time, and liquid medium.

Chemical reduction by organic and inorganic agents, e.g. sodium citrate, ascorbate, sodium borohydride, hydrogen, Tollens, N-dimethylformamide, polyoxometalates, among others, is the most common silver NPs synthesis method (see scheme in Figure 14b). In general, these agents reduce Ag^+ to the formation of Ag^0. This is followed by agglomeration into clusters, and subsequently, the formation of colloidal particles. Moreover, one key factor for the colloids stability is the presence of protective agents, such as polyvinylpyrrolidone (PVP), polyethylene glycol, polymethacrylic acid, tri-sodium citrate (TSC), among others. These compounds can stabilize particle growth, protect particles from sedimentation, agglomeration, but also change the NP surface properties of the nanoparticles. Furthermore, among the classical reduction methods, the UV/Vis (LED, laser, Deuterium-Hallogen lamps)-initiated photoreduction in the presence of $AgNO_3$ and sodium citrate have won also special attention in the last years. Through these methods AgNPs of different size, shape, and high monodispersity have been synthesized. Please refer to Table 7 for a review of the most notable examples according to Iravani et al. [108].

Finally, biological NP synthesis is interesting as high pressure, energy, and toxic chemicals are not required, making them simple, rapid, and eco-friendliness methods. By now, bacteria (*Bacilus licheniformis*, *Bacilus subtilis, Pseudomonas stutzeri, Klebsiella pneumonia, Escherichia, and Enterobacter clocae,* among others)*,* extracts from plants (e.g. Camellia sinensis, alfalfa, geranium, *etc.*), and marine plants like seaweed *Ulva lactuta*, and *Trigonella foenumgraecum, and* algae, have been used as reduced agents and/or stabilizers [108-110].
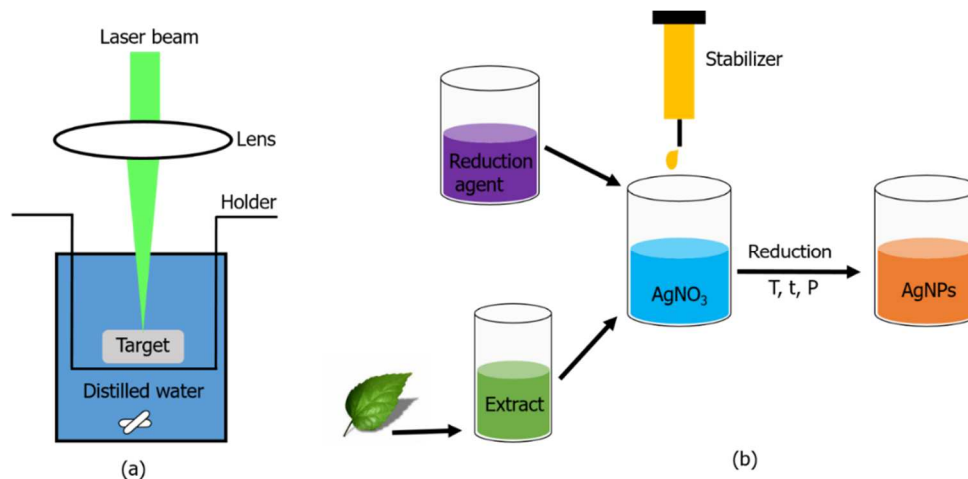
Figure 14. Scheme of physical, chemical and biological synthesis methods for AgNPs. (a) Experimental setup for colloid preparation by laser ablation. Diagram based on [106]. (b) Common reduction methods of silver nitrate by chemical and biological reducing agents.

Table 7: Some important methods for synthesizing silver nanoparticles according to Iravani et al. [108].

Method	Silver precursor	Reducing agent	Stabilizing agent	Size (nm)
Chemical reduction	$AgNO_3$	DMF	-	<25
Chemical reduction	$AgNO_3$	$NaBH_4$	Urfactin (a lipopeptide biosurfactant)	3-28
Chemical reduction	$AgNO_3$	Tri-sodium citrate	Tri-sodium citrate	30-60
Chemical reduction	$AgNO_3$	Ascorbic acid	-	200-650
Chemical reduction	$AgNO_3$	NaBH4	DDA	7
Chemical reduction	$AgNO_3$	Paraffin	Oleylamine	10-14
Chemical reduction (Thermal)	$AgNO_3$	Dextrosse	PVP	22
Chemical reduction	$AgNO_3$	Hydrazine	-	2-10

(Thermal) Chemical reduction (Glucose oxidation)	AgNO$_3$	Glucose	Gluconic acid	40-80
Chemical reduction (Polyol Process)	AgNO$_3$	Ethylene glycol	PVP	5-25
Chemical reduction (Polyol Process)	AgNO$_3$	Ethylene glycol	PVP	50-115
Chemical reduction (Polyol Process)	AgNO$_3$	Ethylene glycol	PVP	11
Chemical reduction (Tollen)	AgNO$_3$	m-Hydroxy benzaldehyde	PVP	15-260
Physical synthesis	Ag wires	Electrical arc discharge, water	-	10
Physical synthesis	AgNO$_3$	Electrical arc discharge	Sodium citrate	14-27
Photochemical reduction (pulse radiolysis	AgClO$_4$	Ethylene glycol	-	17-70
Photochemical reduction (microwave irradiation)	AgNO$_3$	Ethylene glycol	PVP	5-10
Photochemical reduction	AgNO$_3$	UV light	-	4-10
Photochemical reduction (X-ray radiolysis)	Ag$_2$SO$_4$	X-Ray	-	28

2.5.2. Stability of colloidal silver nanoparticles

Reactivity and stability of silver nanoparticles are influenced by the surrounding environment. During the last decade, it has been widely demonstrated that Ag colloids highly interact under the presence of dissolved oxygen, and or UV/Vis/NIR light irradiation. Due to the importance for the present study, some of these interactions will be discussed in more detailed in the next sections.

Oxygen interaction

Silver colloids are known to be highly stable for long periods of time under the presence of nitrogen saturated environments (days → months). This is in contrast to what is observed under aerobic conditions, where they are known to highly interact with oxygen present in the aqueous media to produce silver ions (see example from [111] for Ag^+ production in anaerobic and aerobic conditions). According to Liu and Hurt [112], in aerobic conditions, nanoparticle oxidation takes place involving a cooperative oxidation of oxygen and protons highly dependent on pH, as shown Equation (22). Most likely, oxygen is reduced by simple redox reactions that produce peroxide intermediates, rather than through a four-electron transfer mechanism. In this sense, oxygen should be reduced by a one-electron reaction to the formation of the superoxide anion, which further react with Ag^0 to release Ag^+ (Equation (21)). As a result, an aerobic colloid solution will consist of metallic Ag^0, and free Ag^+ and its complexes (e.g. Ag_2O, Ag_2S, Ag_3(citrate)), dissolved from the particle surface (see scheme in Figure 15).

Furthermore, studies measuring AgNP toxicity by liberation of Ag^+ have shown that particle properties, such as size, shape, surface coating, and surface charge clearly influence the rate, extent, location, and timing of silver release. For example, polyvinylpyrrolidone, tannic acid are more prone to release Ag^+ than citrate-stabilized NPs [113]. Moreover, as demonstrated by the same authors, bigger particles (50 nm) showed to persist an extended period of time compared to smaller (< 10 nm) clusters. While presence of NaCl in the aqueous media did not trigger the Ag^+ dissolution, total organic carbon and speciation could have an influence on the NPs degradation. In accordance with these results, Liu et al. developed a complete characterization for various chemical approaches for controlling the release of soluble active silver ions. According to the authors, the most effective methods are the surface modification involving preoxidation, sulfidation, and thiol ligand exchange [114].
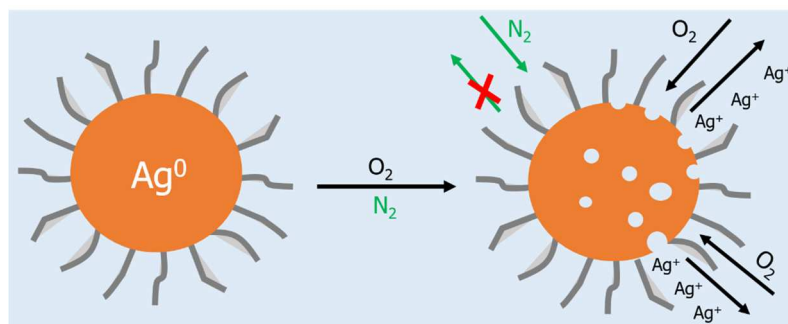
$$O_2 + H^+ \xrightarrow{Ag^0} Ag^+ + peroxide\ intermediates \xrightarrow{Ag^0} Ag^+ + H_2O \tag{21}$$

Figure 15.(b) Schematic representation of the oxidative dissolution of Ag$^+$ ions in water.

Light interaction (UV, VIS-NIR)

AgNP colloids exhibit surface-plasmon resonance absorbance at relatively long wavelengths depending on the NP configuration, making them ideal for fast UV/Vis characterization. A pioneer work from Mock et al. [115], studying individual NPs with transmission electron microscopy (TEM) imaging and optical spectroscopy demonstrated that the geometrical nanoparticle shape plays a major role in determining the plasmon resonance, while the spectrum redshifts with increasing particle size. Moreover, simple heat treatments showed to modify the particle shape, resulting in a variation of its plasmon resonance properties. However, this ability of Ag colloids to interact with light have also shown to produce a variety of desired and undesired photochemical transformations at the nanoparticle surface, which could lead to NP degradation and/or transformation to bigger aggregates (e.g. nanoprisms, rods, etc.).

Batch studies developed by Gorham et al. [116], showed that AgNPs irradiation with UV light ($\lambda < 400$ nm), leads to a faster photooxidation of the NP surfaces as without irradiation. In general, it is accepted that UV light photoactivates the NP surface to promote an electro-transfer mechanism with oxygen present in the colloidal solution. According to the authors, in a colloid aqueous system, oxidation of AgNP surface (formation of core-shell structure) is followed by dissolution into silver ions and subsequent decrease in particle size, and some agglomeration or aggregation (see exemplary scheme in Figure 16). These results are in great in accordance to the ones presented by Grillet et al. [117], during the photooxidation of individual AgNPs under aerobic conditions. Measurements were taken in a Spatial Modulation Spectroscopy setup, which allowed the real-time observation of the clusters through its extinction cross-section evolution, together with further TEM characterization. The authors observed the continuous formation of a core-shell (e.g. 11 % Ag^0- 89 % Ag$^+$, after 9 hours of light irradiation) structure, and correlations of these changes with the particle plasmon resonance properties were developed. As in a normal NP oxidation by oxygen, the UV photoenhanced process are

known to be highly dependent on the NP morphology. For instance, the authors demonstrated that core-shell formation was faster under spherical particles than in nanocubes.
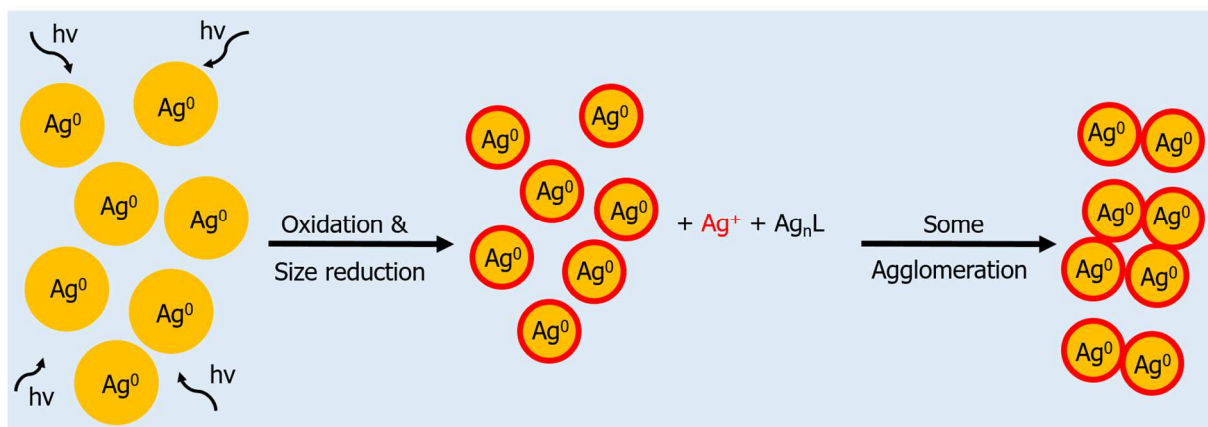
Figure 16. (a) Proposed mechanism by Gorham et. al, for the photoinduced transformations of AgNPs when exposed to 300 nm UV light. ● Pristine AgNP, ● surface-oxidized AgNP, n number of atoms, L= ligand.

On the other hand, early studies developed by Jin et al. [118], demonstrated the complete photoinduced conversion of silver nanospheres (8 nm) to nanoprisms (10 – 60 nm edge lengths) after 70 hours of fluorescent light irradiation ($350 < \lambda < 700$ nm, 40 W). They proved that reaction can be selectively turned on and off simply by controlling the colloid exposure to the appropriate wavelength. According to the authors, nanoparticle transformation followed three stages: induction, growth, and termination, which were clearly observable by following the change in the surface-plasmon resonance along the reaction time (see example in Figure 17a). Moreover, as schematically depicted in Figure 17, in the induction period extremely small spherical clusters (2 – 4 nm) together with small nanoprisms (5 -10 nm edge lengths) were formed by possibly fragmentation or dissolution of the initial particles. Next, the nanoprisms act as seeds and grow as the small spherical clusters disappeared. Once all spheres are consumed, the reaction terminates.

Lately, Wu and co-authors [119], proposed for the first time the mechanism of reaction taking place during nanoparticle transformation, coining as the Photo-voltage mechanism for it. According to the authors, the photochemical process occurs at very low light intensity over a period of hours or days. The mechanism therefore should be a combination of oxidative etching of reduced Ag, followed by the reduction of Ag^+ onto prisms, due to citrate photooxidation. In other words, nanoparticle seeds absorb light and weakly reduce dioxygen and release Ag^+ (see Equation (22)), subsequently, prims that absorb more strongly oxidize citrate, reduce Ag^+, and

gain Ag (Equations (23) and (24)). The overall reaction should be then the indirect photooxidation of citrate by oxygen catalysed by silver (Equation (25)).

Recently, this concept has been improved for the efficient preparation of silver nanoparticles with various sizes and morphologies, including dodecahedra, nanorods, and nanoplates. Stamplecoskie and Scaiano [120], irradiated small seeds (3 nm) with cost-efficient light-emitting diodes at different excitation wavelengths allowing the selectively formation of bigger particles, and or different shapes, as depicted in Figure 17b.

(a)   **(b)**
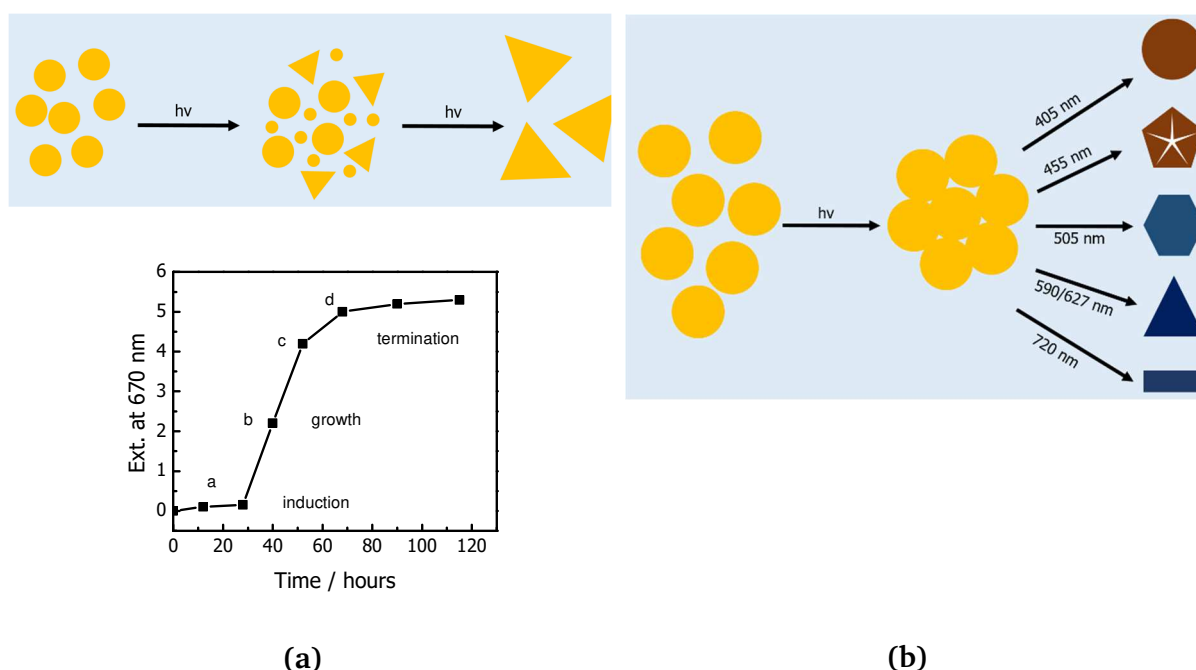
Figure 17. (a)Schematic representation of the mechanisms of formation of nanoprisms from nanospheres by light irradiation. Diagram: Absorption at 670 nm vs. time for a complete experiment. Diagrams based on [118].(b) Aggregation/Coalescence mechanism of transformation of AgNP seeds irradiated with different wavelengths. Diagram based on [120].

Seeds reduction and lose of silver ions:

$$2Ag + \frac{1}{2}O_2 + H_2O \rightarrow 2Ag^+ + 2OH^-$$

(22)
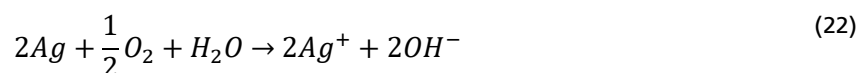
Citrate oxidation, Silver reduction:

$$citrate \rightarrow acetone - 1,3 - dicarboxylate + CO_2 + H^+ + 2e^-$$

(23)

$$2e^- + 2Ag^+ \rightarrow 2Ag \qquad (24)$$

Overall reaction is the indirect photooxidation of citrate by oxygen catalysed by silver:

$$citrate \frac{1}{2}O_2 \rightarrow acetone - 1,3 - dicarboxylate + CO_2 + 2e^- \qquad (25)$$
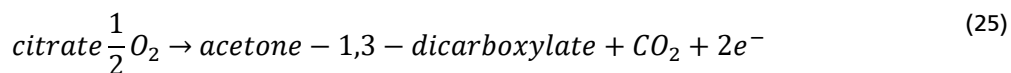
As already summarized, silver colloidal nanoparticles suffer chemical and photochemical transformations depending on their surroundings. Thus, since technical CNP suspensions will be exposed to different working conditions, it is essential to develop simple and fast screening methods to define how variables, such as temperature, gas saturation, light exposure, ligand concentrations, physical media, *etc.,* may affect their initial properties and surroundings [121, 122]. Among other techniques for measuring NP morphological changes [117, 123]; by now, exposing CNP batch solutions to controlled atmospheres within conventional photo-reactors (see scheme in Figure 18a) seems to be the chosen method for developing stability studies [116, 124, 125]. This method is rather simple, and products can be easily analysed by *ex situ* electron microscopy, liquid-and gas-phase analysis techniques, optical spectroscopy, and others. However, the long experimental times required (hours to months), due to e.g. inhomogeneous light-matter interaction, and gas-liquid mass-transfer limitations, could lead to i. the misidentification of different transformations taking place, and ii. a bottle neck in the synthesis and characterization process. Thus, the photo-activation (intense light-sample interaction), long path lengths (i.e. highly diluted samples), and gas permeation (i.e. fully saturated gas environments) properties, make the LCWM reactor attractive for carrying out ultra-fast stability studies under highly diluted samples (Figure 18b).
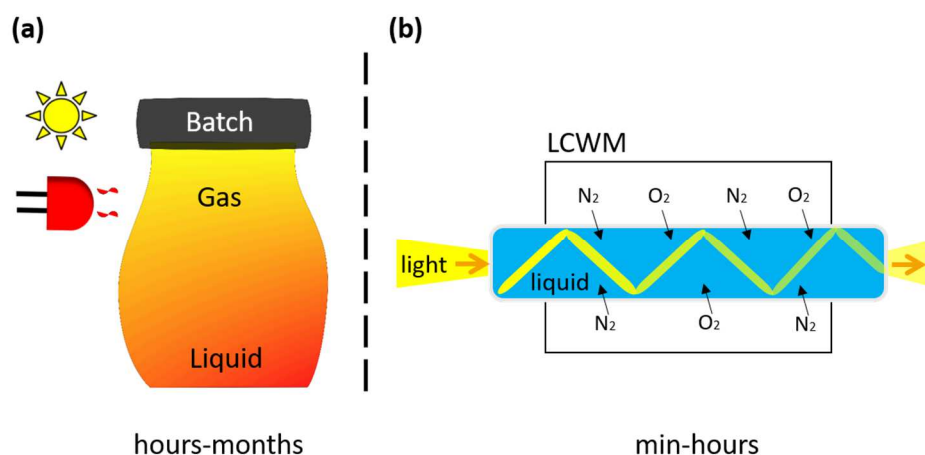
Figure 18. Scheme of a classical stability test in batch (a) compared to one in a LCWM optical reactor (b).

3. Objectives and Scope of the Study

The goals of this work are the design, setup, characterization, and application of a new microreactor concept for the *in situ* sensing and/or photoactivation of gas-liquid reactions. Key of the setup is a liquid-filled Teflon AF-2400 tube, which is known to provide light transmission by TIR within the core, and high gas permeation rates through the wall. With this knowledge, the combination of these two outstanding properties in one setup will be proposed to realize a liquid core waveguide membrane microreactor.

In the first part of this work, special focus will be given on a complete characterization of the new reactor setup from an optical and chemical engineering point of view. Cut-back experiments will be carried out to determine the wavelength depended optical losses in the tube. Furthermore, the setup UV/Vis/NIR spectroscopy performance will be validated by comparing spectra and molar absorption coefficients for different substances with absorbance in this regime. The application of Lambert-Beer's law for linear calibration will be also tested by performing concentration variation measurements of a color dye. Light transmission stability while developing semi-batch transient response studies (CO_2, $N_2 \leftarrow \rightarrow$ air) and gas-permeation in continuous flow experiments will be verified. On the other side, residence time distribution measurements will be developed to characterize the flow inside the Teflon AF tube, which could influence its behavior as reactor. For that, a step input experiment at the feedstock will be carried out to measure the time-dependent concentration distribution of a dye at the inlet and outlet of the Teflon AF tube at different volumetric flows. To obtain the age distributions of the reactor analytical calculations based on the tank-in-series model and the dispersion model will be applied. With these results, possible influence of dispersion in kinetic calculations in continuous mode within the setup shall be discussed.

Afterwards the possibility to use this new optofluidic microreactor for lab studies, will be demonstrated in three case studies:

i. A study of the kinetics of heteropoly acids employed a for partial biomass oxidation.
ii. A fundamental study concerning the complex methylene blue (photo)degradation in alkaline solutions.
iii. A study on the stability of silver nanoparticle (AgNP) colloids.

For the first application, the LCWM system will be tested as a chemical microreactor for performing *in situ* measurements with temperatures up to 150 °C. Vanadium-substituted Keggin-type heteropolyacid catalysts are received from the Biomass and Sustainable Production

of Platform Chemicals group at the University of Erlangen-Nuremberg. With these catalysts, the kinetics of the reduction and reoxidation step of the catalytic cycle will be deduced by *in situ* UV/Vis spectroscopy. Glucose and ethylene glycol are chosen as model substrates for this work. For the reduction experiments, measurements will be taken under anaerobic conditions to suppress the reoxidation pathway. From absorption spectra, concentration versus time profiles shall be obtained to determine the kinetic parameters through a power law approach. For the reoxidation step, transient response experiments with pre-reduced catalysts will be used to deduce the reoxidation kinetics. Kinetic data shall be quantitative and qualitative compared with literature values obtained in autoclave experiments. Furthermore, together with further characterization, such as cyclic voltammetry, Raman spectroscopy, and EPR measurements, insights into the mechanism of reaction of the different catalysts shall be discussed.

In the second application, the possibility of performing photoactivation and *in situ* sensing of ultra-low concentration side reactions within the setup will be tested. For that, the simple redox methylene blue cycle triggered by glucose and alkali is chosen as benchmark reaction. Transient response experiments will be first carried out to deduce the effect of light irradiation under the normal MB redox cycle. Then, possible extra degradation patterns will be studied separately under anaerobic and aerobic conditions. The dynamic change in the UV/Vis spectra shall be analyzed and discussed. Possible formation of new species will be studied by spectra deconvolution and further characterization techniques, such as MS-spectroscopy, HPLC separation, and proton nuclear magnetic resonance (H-NMR) spectroscopy. Finally, a possible new reaction pathway summarizing the complete studied effects shall be discussed.

In the final application, the intense light-sample and high gas-liquid interactions within the LCWM reactor to perform stability studies under colloidal NP solutions will be tested. Due to their broad application, silver nanoparticles are chosen as a model substrate. Silver nanoparticles will be synthesized following standard methods published in literature with different initial amounts of citrate. Degradation experiments under UV-light (deuterium lamp) irradiation under aerobic and anaerobic conditions will be first carried out. Kinetic data accounting for the photooxidation process shall be obtained. Moreover, the effect of broader light irradiation will be also studied by illuminating the samples with a halogen lamp. NPs morphology properties will be studied by transmission electron microscopy measurements, and applying the MIE model by fitting the UV/Vis surface-plasmon resonance spectra obtained. Finally, advantages regarding the application of the LCWM setup compared to conventional batch photo-reactors in literature shall be discussed.

4. Experimental Section

4.1. Solvents and chemical substances

Substance	Producer	Purity	Product ID
Acid orange 7	Sigma-Aldrich	>85 %	
Azure A	Alfa-Aesar	-	Lot: W06C014
Azure B	Sigma-Aldrich	-	Lot: #MKBX6668V
Azure C	Alfa-Aesar	-	Lot: G03Y032
Thionin-Acetat	Acros Organics	-	Lot: A0380355
Methylene blue	Sigma-Aldrich	82 %	M9140-25G
Methylene violet	Sigma-Aldrich	>65 %	Lot: 17196PH
Iron(III)-Chloride	Sigma-Aldrich	97 %	157740-100G
Hydrogen Peroxide	Carl Roth GmbH & Co	30 %	CP26.4
Oxalic acid dehydrate	Merck Millipore	99 %	8182420100
Sodium Hydroxide	Alfa-Aesar	99 %	
Silver Nitrate	Sigma-Aldrich	>99 %	Lot: #BCBP5006V
Tri-sodium citrate dihydrate	Fischer Chemical	-	Lot:1709634
Sodium borohydride	Acros Organics	>98 %	Lot: A0392565
Phenol	VWR chemicals	-	Lot: 13J010009
D-(+)-Glucose	Sigma-Aldrich	99.5 %	G8270-100G
Ethylene glycol	Grüssing GmbH	99 %	
Chloroform			
Methanol	Sigma-Aldrich	99.8 %	
Acetic acid	Carl Roth GmbH & Co	>99.8 %	-
High purity water	VWR chemicals		-
Carbon dioxide	Westfalen AG	99 %	
Nitrogen	Linde AG		-
Synthetic air	Westfalen AG	80 % N_2/20 % O_2	-

4.2. Liquid core waveguide membrane microreactor setup

A Teflon tube (AF-2400, *Biogeneral*, 1.0 mm i.d., 1.6 mm o.d.) was employed as core component of the LCWM microreactor (see Figure 19 and a picture of the real setup in Figure A.1). Key components are the custom-made polymethyl methacrylate (PMMA) T-fluidic cells (*a* & *b*) (see Figure A.4), which are placed at the beginning and end of the reactor. In these cells, the liquid and optical pathway is combined. Hence, the inlet fluidic cell is connected to an HPLC pump (E2001, *ProMinent Electronics*), conveying the reactants to the reactor, and to a light source (DH-2000, *Ocean Optics*, with Deuterium and Tungsten-Halogen Lamps) via a standard optical fiber (OCF-102754, *Ocean Optics*). The outlet fluidic cell is connected to a backpressure regulator (BPR) (*Upchurch Scientific*, 40-100 psi) (*c*) and a gauge (*d*) to control the liquid pressure within the Teflon AF tube. The liquid stream is collected in vials to generate liquid samples. The optical pathway after the outlet fluidic cell connects to a spectrometer (Spectro 320 (D) R5, *Instrument Systems*) through a standard optical fiber (OFG-322, *Instrument systems*). Between the fluidic cells, the Teflon tube itself is placed within a steel tube (1/4" o.d., 5.3 mm i.d.) by bored-through unions, forming the tube-in-tube gas-liquid contactor. Gas is supplied (*g*) and leaves the outer steel tube through two T-pieces (*e* & *f*). A backpressure valve (*h*), at the end of the line, sustain the desired pressure along the system. After the backpressure valve, a flow controller (*o*) limits the gas flow. Due to the tube-in-tube arrangement, gas permeates through the wall of the inner Teflon AF tube towards the liquid-filled core of the Teflon tube. In addition, for semi-batch operation, the liquid is pumped into the LCWM microreactor and two-way ball valves (*m* & *n*) at the inlet and outlet of the liquid pathway are closed, while gas is continuously flushed through the outer steel tube and gas pathway. Finally, for safety issues, pressure is measured using a gauge (*i*), and controlled by a safety release valve (*j*) adjusted to 40 bar. Finally, a heating wire (*k*) connected to a heater controller (*Julabo*, LC5-E) surrounds the outer steel tube, and the temperature is monitored by two thermocouples (*l*).
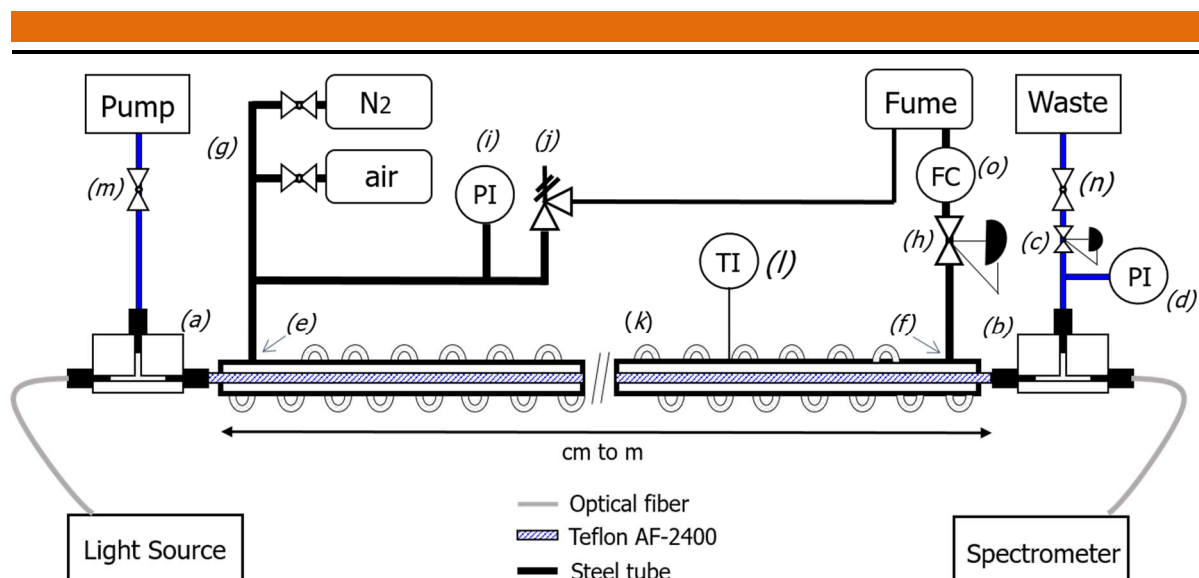
Figure 19. Scheme of the liquid core waveguide membrane optical microreactor using a Teflon AF-2400 tube (not to scale drawing). PI: pressure indicator, TI: temperature indicator, FC: flow controller.

4.3. General experiment in semi-batch and continuous operation within the LCWM

For the semi-batch experiments, measurements were taken as follows: i. a constant temperature was set on the LCWM reactor (27 to 150 °C), ii. the tube-in-tube contactor was flushed with gas (nitrogen or synthetic air) and the pressure set to the required pressure (< 8 bar), iii. the system was filled with bi-distilled water and a background spectrum was taken, iv. the reaction mixture was pumped into the reactor. The liquid inlet and outlet two-way valves were closed after a desired constant liquid pressure was reached (< 8 bar), v. for continuous-irradiated experiments: light transmission and optical absorption spectra recording (200 to 1000 nm in water) were started; on the other hand, for interval experiments: lights went on only to record the spectra every 10 min, vi. for gas exchange experiments (transient response experiments): the initial gas was liberated to the fume and the system flushed with the new gas, and vice versa, vii. finally, the time-evolution of different compounds was studied at different peak maxima. For continuous operation experiments, reaction mixture was continuously pumped through the system, while the inlet and outlet valves stayed open. The liquid-phase pressure was controlled by a fixed-pressure BPR (2.7 or 7 bar).

4.4. Optical losses and absorption measurements

Standard cut-back experiments following the procedure in [13] were carried out to determine the optical losses of a Teflon AF tube filled with bi-distilled-water. In general, the light transmission (P_1) was measured in the region between 350 and 750 nm, connecting the two sides of the tube to the fluidic cells. Without disturbing the input conditions, the tube was cut

back to different lengths (L) (e.g. 469, 419, 289, 149 cm) and its light transmission was measured (P_2). The fiber optical losses were calculated applying Equation (26). In addition, for absorption experiments measurements were taken as follows: i. a 52 cm Teflon AF tube was filled with bi-distilled water as reference and the intensity profile recorded in the UV/Vis range; ii. the tube was then filled with the test solution at different concentrations and the spectra recorded, and iii. the molar absorption coefficient was calculated from Lambert-Beer's law. Corresponding data were also recorded in a conventional spectrometer (Perkin Elmer, Lambda 900) with a 1 cm cuvette cell for comparison.

Moreover, for measurements in the Vis-NIR range of water-filled tubes, absorption coefficient as function of wavelength ($\propto (\lambda)$) were calculated as shown in Equation (27), where P_0 is light transmission in tetrachloroethylene-filled tubes used as reference, and P_{liq} is the light transmission with the tube filled with bi-distilled water.

$$Optical\ loss\ (dB\ m^{-1}) = \frac{10 * log_{10}\left(\frac{P_1}{P_2}\right)}{(L_1 - L_2)} \tag{26}$$

$$\propto (\lambda) = \frac{\ln(\frac{P_{liq}(L_1,\lambda)}{P_{liq}(L_2,\lambda)}\frac{P_0(L_2,\lambda)}{P_0(L_1,\lambda)})}{L_2 - L_1} \tag{27}$$

4.5. Residence time distribution step input experiments

Residence time distribution measurements were carried out by applying a step change of the liquid feedstock via a peristaltic pump (REGLO Analog, *Ismatec,* see calibration in Figure A.2b in Annex). The pump feed was changed from pure bi-distilled water to a 40 µM MB solution. This step change was repeated for different volumetric flow rates ranging from 0.20 to 1.59 mL min^{-1}, which represent residence times from 258 to 33 s in a 112 cm Teflon AF tube. The time-dependent concentration distribution of the dye at the inlet and outlet of the Teflon AF tube were recorded using the One-Point-Measurement setup (see Figure 20). Two common optical fibers (FT200UMT, *Thorlabs,* 300-1200 nm, and FG050LGA, *Thorlabs*, 400-2400 nm) are mounted perpendicular to the Teflon AF tube, while facing each other and being connected to light source and spectrometer. Thus, the spectroscopic information is obtained at a specific axial position (here inlet and outlet) and not an integral of the whole reactor. Absorption spectra at 664 nm were recorded every   5 s.
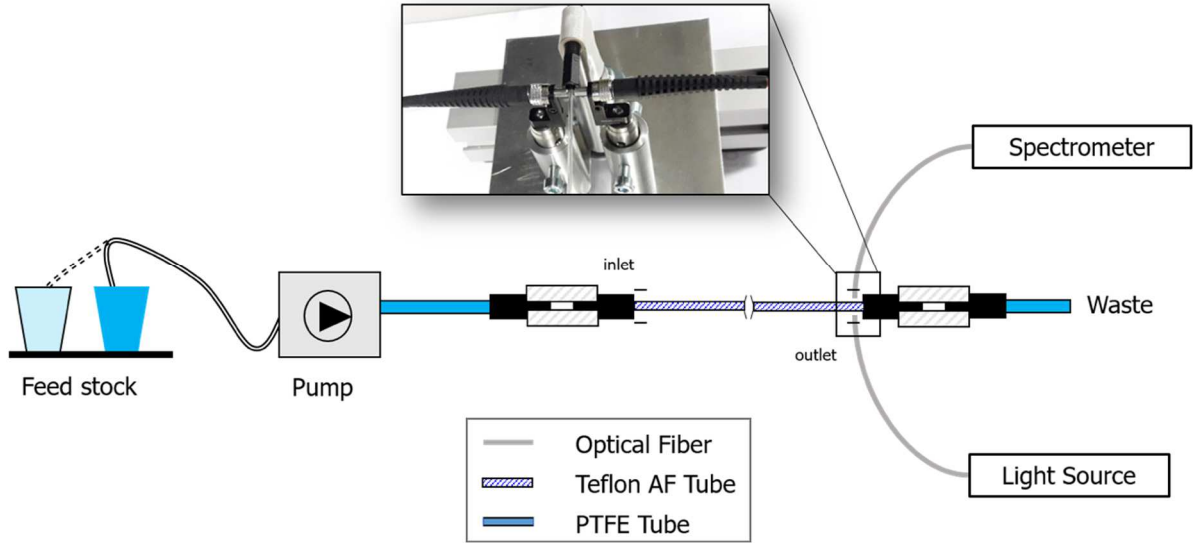
Figure 20. Schematic representation of the one-point measurement at the inlet and outlet of the Teflon AF tube (not-to-scale diagram).

4.5.1. Age distribution calculation and kinetic modelling

Two RTD models, the tank-in-series and the axial dispersion model were applied in this work to calculate the $E(\theta)$ functions.

Tank-in-Series model

This simple model considers a reactor as a cascade of N identical continuously stirred tank reactors with the same total volume as the actual reactor. Accordingly, $E(\theta)$ can be expressed as a function of N (Equation (28)):

$$E(\theta) = (N\theta)^{N-1} * \frac{N}{(N-1)!} e^{-N\theta} \tag{28}$$

where E represents the age distribution, N the number of tanks, θ the dimensionless time.

The age distribution is characterized by the variance σ_θ^2 and the standard deviation σ_θ, which is a quantity for the spread of the curve. The variance is correlated with the number of tanks N (Equation (29)).

$$N = \frac{1}{\sigma_\theta^2} \tag{29}$$

Like this, N can be approximated from a measured RTD by determining the variance with the help of the two first raw moments(μ) of the distribution (Equation (30)).

$$\mu_n = \int_0^\infty \theta^n E(\theta)d\theta \qquad \sigma_\theta^2 = \mu_2 - \mu_1 \tag{30}$$

Axial dispersion model

Here, the Bodenstein (Bo) number represents the spread of the curve. Smaller values of Bo widen the spread of the curve. When Bo approaches infinite, the flow in the tube approaches plug flow behavior. For the age distribution, it is possible to derive an analytical solution (Equation (31)), and relate the Bo numbers to the variance (Equation (32)).

$$E(\theta) = \sqrt{\frac{Bo}{4 * \pi * \theta}} * exp\left[-\frac{Bo * (1 - \theta)^2}{4 * \theta}\right] \tag{31}$$

$$\sigma_\theta^2 = \frac{2}{Bo} + \frac{8}{Bo^2} \tag{32}$$

Conversion and kinetic modelling

According to literature, the concentration profile along the reactor can be solved more accurately with the help of the Bo number obtained in RTD experiments. Successively, this concentration profile could be inserted into to the absorption term (Beer-Lamber equation), to obtain an expression which relates the measured absorbance in the spectrometer as a function of the kinetic constant (Equation (33)).

$$Absorbance = 4 * \varepsilon * c_{A,0} * exp^{\frac{Bo}{2}} \int_0^L \frac{a}{(1 + a)^2 * exp^{\frac{a*Bo}{2}} - (1 - a)^2 * exp^{\frac{-a*Bo}{2}}} \tag{33}$$

$$a = \sqrt{1 + \frac{4 * k * L}{Bo * v}}$$

$$Absorbance = \varepsilon * c_{A,0} * \int_0^L (exp^{\frac{k*L}{v}}) \tag{34}$$

where L represents the length of the tube (cm), v the flow speed (cm s^{-1}), k the kinetic constant of the reaction system (s^{-1}), ε the molar absorption coefficient of the substance (L mol^{-1} cm^{-1}), and $c_{A,0}$ the initial concentration of the substance (mol L^{-1}).

As we were unable to obtain an analytical solution of (Equation (33)), the right term of the equation was numerically integrated using MATLAB. With this expression, k was fitted to the absorbance values measured at the outlet fluidic cell during flow experiments, then the concentration path was modelled along the tube. The same procedure was developed considering a simple concentration gradient for ideal flow (Equation (34)).

4.6. Heteropolyacid catalysts

Keggin-type heteropolyacid catalysts were synthesized and received from the Biomass and Sustainable Production of Platform Chemicals group at the University of Erlangen-Nuremberg with the following characteristics (see Table 8).

Table 8. Composition of Keggin-type heteropolyacid catalysts used in this work. Original content [126].

Catalyst	Molecular composition	P/V/Mo ratio
HPA-0	$H_3[PMo_{12}O_{40}]$	1/0/11.83
HPA-1	$H_4[PVMo_{11}O_{40}]$	1/0.82/11.14
HPA-2	$H_5[PV_2Mo_{10}O_{40}]$	1/2.01/10.12
HPA-5	$H_8[PV_5Mo_7O_{40}]$	1/4.87/7.21

To get further evidence into the presence of vanadium in the heteropolyacid cage, square wave voltammograms Raman spectra, and XRD measurements of the prepared catalysts were recorded. On the one side, the electrochemical measurements were performed as described in Section 4.9. Figure 21a shows a comparison of the catalysts indicating significant changes with increasing the vanadium content. While the main redox-peaks at -0.46, -0.40, and +0.30 increased with increasing the V-content, a decrement of the peaks at -0.56 and +0.20 was also observed. This implies that peaks at -0.40 and +0.30 should belong to the reduction of different vanadium species.

On the other side, Raman spectroscopy was conducted using a laser Raman microscope at a wavelength of 532 nm. As Figure 21b depicts, whole catalysts exhibited the main bands assigned to heteropoly compounds with a Keggin structure, which is also confirmed by the X-ray spectra (see Figure A.10 in Annex): i. split bands between 230-250 cm^{-1} (M=O groups), ii. broad band at 625 cm^{-1} (Mo-O$_c$-Mo vibration bands), iii. bands in the region 876-909 cm^{-1} (Mo-O$_b$-Mo and Mo-O-P stretching vibrations), and iv. band at 984 and 1002 cm^{-1} (Mo-O$_d$ stretching bands) [127, 128]. The gradual disappearance of bands, predominantly in the regions at 625 cm^{-1} and 876-909 cm^{-1}, implies that the Keggin structure was partially damaged by the substitution of vanadium in the structure.
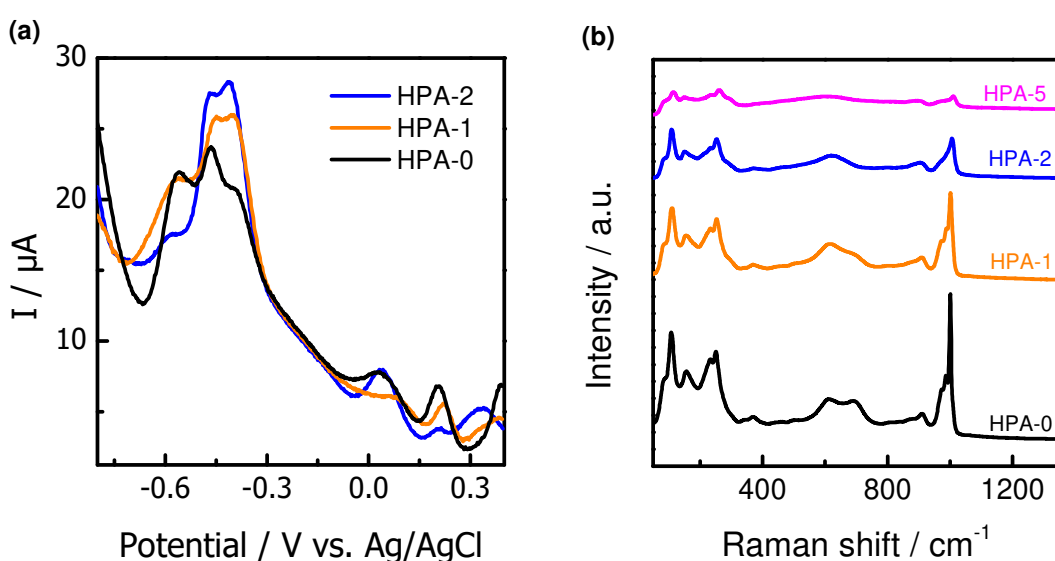
Figure 21. (a) Square wave voltammograms of HPA-n (n= 0, 1, 2) in a 0.5 M Na$_2$SO$_4$ aqueous electrolyte solution (pH=3.3), potential range +0.4 to -0.8. (b) Raman spectra of HPA-n (n= 0, 1, 2, 5) powder catalysts. Diagrams original source [126].

4.6.1. Preparation of HPA-n reduced (HPA-n$_{red}$) catalysts in batch

Reduction of HPA-n$_{ox}$ catalysts by glucose was carried out in a magnetically stirred two-neck glass reactor (25 mL) equipped with a reflux condenser and temperature control. The reactions took place at least 1 hour under vigorous stirring (700 rpm) in a nitrogen-presaturated solution at 80 °C. The initial concentration ratio between glucose and the catalysts was 50:1. The final pH of the reacted solution showed a negligible change with respect to the initial values.

4.6.2. Kinetic method used in the experiments

Reduction step

The time-evolution of the HPA-n_{ox} catalysts was studied at 450 nm every 15 s with glucose as a substrate. Same experiments were developed with ethylene glycol as a substrate for comparison. Concentration versus time profiles obtained from UV/Vis spectra (see example for a HPA-2 catalyst in Figure 33b in Section 5.2) were employed to determine the initial reaction rate from the initial slope in the first 300 s, which represents less than 10 % of total conversion. As glucose was in excess, its concentration was assumed to be constant and is summarized within the reaction rate constant. Finally, a power law (see Equation (35)) and Arrhenius law (Equation (37)) were employed to describe the reduction rate. The reduction rate constant and order was determined by linearization of the logarithmic form as in Equation (36).

$$r_{0,red} = k_{red} * c_{0,HPA-n_{ox}}^{a} \tag{35}$$

$$lnr_{0,red} = lnk_{red} + a * \ln(c_{0,HPA-n_{ox}}) \tag{36}$$

$$k_{red} = k_0 * e^{\frac{-E_a}{RT}} \tag{37}$$

where $r_{0,red}$ (µM min^{-1}) is the initial reduction rate, k_{red} (min^{-1}) the reduction rate constant, $c_{0,HPA-n_{ox}}$ (µM) the initial catalyst concentration in the oxidized form, a represents the reaction order, k_0 denotes the pre-exponential factor, E_a (J mol^{-1}) the activation energy, R (J K^{-1} mol^{-1}) the universal gas constant, and T (K) the absolute temperature.

Oxidation step

The time-evolution of the HPA-n_{red} catalysts was studied at 750 nm every 60 s. Initial reaction rates (Equation (38)) were obtained again from the initial slope of the concentration versus time curve. Due to the very fast gas-liquid mass transfer, the oxygen concentration in solution is assumed to be constant. Activation energy values were calculated applying (Equation (37)) for the reoxidation reaction rate constant values and temperatures.

$$R_{0,ox} = -\frac{dc_{0,HPA-n_{red}}}{dt} = -k_{ox} * c_{0,HPA-n_{red}} \tag{38}$$

where $R_{0,ox}$ (μM min^{-1}) represents the initial reoxidation reaction rate, k_{ox} (min^{-1}) the reoxidation rate constant, and $c_{0,HPA-n_{red}}$ (μM) the initial catalyst concentration in the reduced form.

4.7. Spectra deconvolution method

To identify different Methylene blue degradation species, an absorption spectra deconvolution was applied. The procedure follows an improved method based on Marban et al [102]. A calibration in aqueous solution in the 0.1 to 0.6 μM range for all expected species (entries 1-6 in Table 6) was performed. To obtain the Gaussian deconvolution of the spectrum, a linear baseline crossing the 730 and 795 nm was set. Then a number of Gaussian peaks with different center, height, and half width of the half maximum (HWFM) were found to obtain a suitable deconvolution of the original spectra (see example for MB in Figure 22a, and parameters for all calibrations in Table A.2 in Annex). From the deconvolution at different concentrations, it was found that the Gaussian parameters, such as center, HWFM and the ratio between the peak heights stay constant. Thus, the peak height was the only one value to be fitted during deconvolution for each specie. The method was validated with a calibration solution of 0.2 μM MB, 0.2 μM MV, and 0.1 μM AB. The spectra of the mixture and the deconvolution is given in Figure 22b (lower panel), while an accurate determination of the given concentrations resulted.
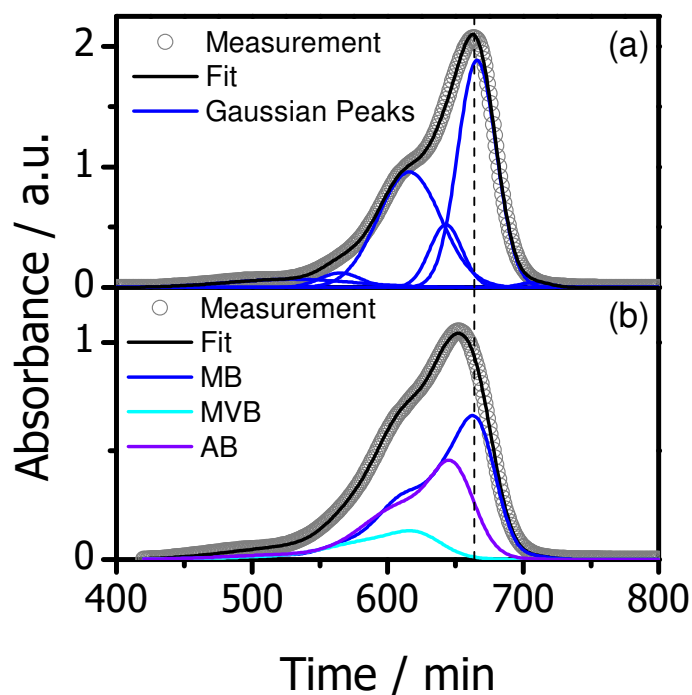
Figure 22. (a) MB (0.6 μM) spectra deconvolution based on a 6 Gaussian peaks method from [102]. (b) Spectra deconvolution of a prepared mixture of MB (0.2 μM), MV (0.2 μM), and Azure B (0.1 μM) with the optimized method.

4.8. Silver nanoparticles synthesis and characterization

Ag NP colloids (see Table 9) were synthesized by adapting a procedure from [119], and follows: i. an Erlenmeyer containing 50 mL of bi-distilled water, 0.5 mL aqueous $AgNO_3$ (100 mM, freshly prepared), and 0.1 to 4 mL tri-sodium citrate (100 mM, freshly prepared, see Table 9) was immersed in an ice bath, and the solution bubbled with N_2 for 20 min under constant stirring, ii. then 0.5 mL of $NaBH_4$ (100 mM, freshly prepared) was quickly added into the vigorously stirred solution, iii. after 10 min, 0.5 mL of $NaBH_4$ were added again, and kept stirred for 20 min, iv. finally, the prepared solution was removed from the ice bath, and aged overnight in the dark under stirring. TEM image analysis of sample 1 shows mainly sphere AgNPs with an average diameter of 8.6 ± 1.2 nm (see TEM image at Figure 23a). These observations are in agreement with the corresponding UV-Vis spectra recorded, showing characteristic surface-plasmon resonance spectrum for spheres particles with a peak maxima approx. at 398 nm (Figure 23b). The spectrum was fitted by applying the Mie model method, and a particle size distribution of 8.64 ± 0.4 nm was predicted (see Figure 23b and explanation below). Moreover, as depicted Figure 24, all prepared samples (2 to 5) showed similar NPs size and distribution independent on the initial capping agent concentration. Finally, AgNP colloids showed to be stable, experiencing no changes within few weeks to months in storage in the dark.
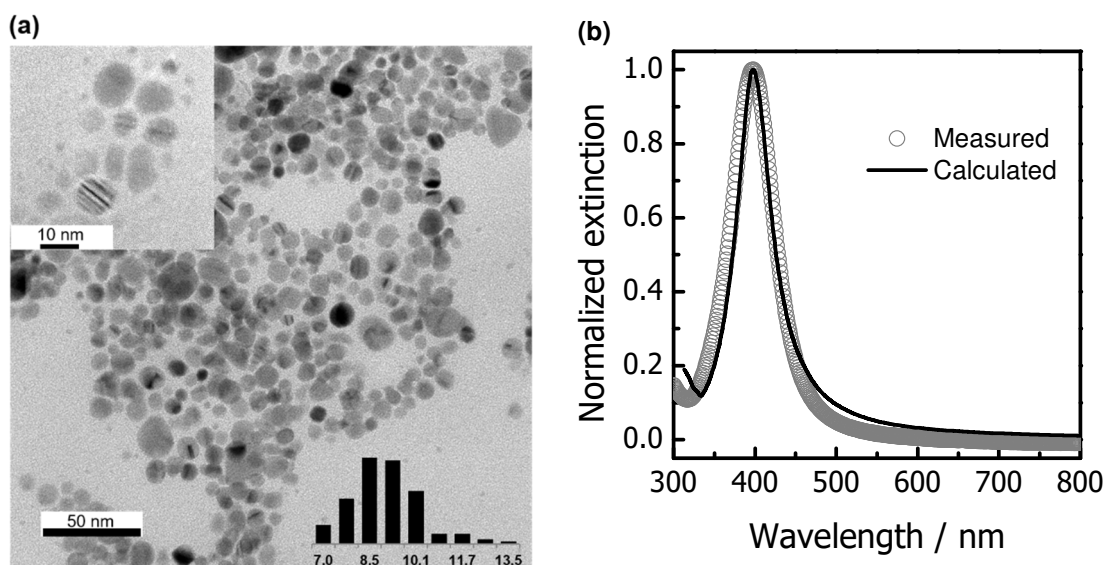
Figure 23. (a) TEM image and particle size distribution of AgNPs synthesized with an initial tri-sodium citrate concentration of 0.2 mM. (b) Experimental and calculated surface-plasmon resonance of sample 1 (0.2 mM of TSC) applying the Mie model method.
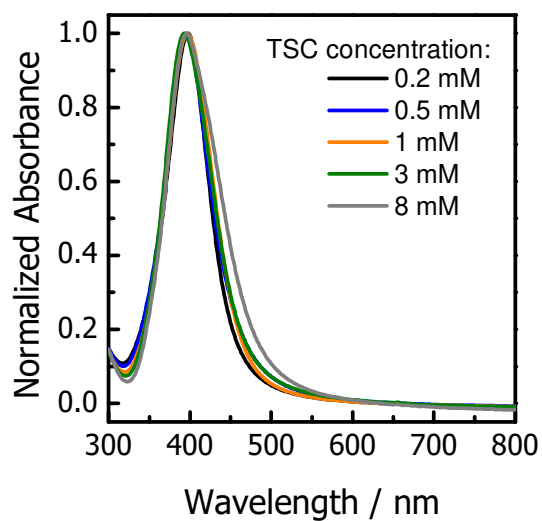
Figure 24. Normalized UV-Vis absorption spectra of the prepared AgNP solutions after aging overnight in the dark with different tri-sodium citrate initial concentrations.

Table 9. Concentration of tri-sodium citrate used in Ag nanoseeds synthesis.

Sample	Volume (mL) (from 100 mM)	C_{TSC} (mM)
1	0.1	0.2
2	0.25	0.5
3	0.5	1
4	1.5	3
5	4	8

4.8.1. Mie model for nanoparticle size distribution calculations

To predict the silver nanoparticle size and size distribution values, the Mie model was used as a tool by fitting the UV/Vis spectra measured in the experiments. The procedure follows a customized method based on the MATLAB code available in (http://dx.doi.org/10.17863/CAM.6226), and developed by Wu et al [129].

As in typical Mie theory calculations, the input parameters are the particle size, and optical functions of the bulk material and surrounding medium. Thus, the extinction cross section was calculated as a function of R_p (radius or size parameter):

$$\sigma_{ext} = \frac{2\pi}{k_{wv}^2} \sum_{L=1}^{\infty} (2L_{mp} + 1)Re[a_L + b_L] \tag{39}$$

$$a_L = \frac{s\psi_L(sx)\psi_L'(x) - \psi_L'(sx)\psi_L(x)}{s\psi_L(sx)\eta_L'(x) - \psi_L'(sx)\eta_L(x)} \tag{40}$$

$$b_L = \frac{\psi_L(sx)\psi_L'(x) - s\psi_L'(sx)\psi_L(x)}{\psi_L(sx)\eta_L'(x) - s\psi_L'(sx)\eta_L(x)} \tag{41}$$

where k_{wv} is the wave vector of incident light, L_{mp} is the multi-pole order, Re denotes the real part of the complex number $a_L + b_L$, a_L and b_L are the Mie scattering coefficients in terms of spherical Ricatti-Bessel functions (ψ_L and η_L). Moreover, ($s = \eta_c/\eta_m$) η_c is the complex index of refraction, η_m) the real surrounding medium index of refraction, and ($x=k_{wv}*R_p$). Additionally, the dielectric constant can be corrected with the term:

$$\Gamma(R) = \Gamma_\infty + A\frac{v_F}{R_p} \tag{42}$$

where Γ_∞ is the bulk metal value, and v_F is the Fermi speed, and A is an empirical parameter, which follows ($A = -0.5495 + 0.6905\,R$) as calculated in [129].

The fitting method was validated with particle size and size distribution calculations from TEM measurements of Sample 1, as depicted above in Figure 23.

4.9. Supplementary characterization

Inductive coupled plasma-optical emission spectroscopy

To analyse the catalyst stoichiometry, inductive coupled plasma-optical emission spectroscopy (ICP-OES) measurements were conducted using a Perkin Elmer Plasma 400 by dissolving ca. 20 mg of the HPA-n catalyst in 250 mL of double distilled water. For calibration on phosphorus, molybdenum and vanadium, ICP-standard solutions (1000 μg per mL) were used.

Raman spectroscopy

To get further insights about vanadium substitution effect under the Keggin structure of the received catalysts (HPA-n), Raman spectroscopy was conducted using a laser Raman microscope (Bruker Senterra 1, NDYAG laser) at a wavelength of 532 nm.

Electrochemical measurements

To analyse the reduction potential properties of the heteropolyacid catalysts received, electrochemical measurements were performed in a three-electrode system connected to a PARSTAT MC Multichannel potentiostat with a platinum working electrode, a platinum coil counter electrode, and an Ag/AgCl reference electrode. All experiments were carried out at room temperature in a 0.5 M Na_2SO_4 aqueous electrolyte solution. The sample solutions were purged with nitrogen for 3 min and then maintained for 1 min for stabilization.

Electro paramagnetic resonance measurements

To account the presence of Vanadium-reduced species in dissolved HPA-n catalysts, electron paramagnetic resonance spectra of 10 mM HPA-n$_{ox}$ and HPA-n$_{red}$ samples were measured on an EPR Miniscope MS-400 (Magnettech, Germany) equipped with a TC H03 temperature controller and a rectangular TE102 resonator operating at 9.43 GHz. All EPR spectra were

recorded at room temperature with a modulation amplitude of 0.2 mT and a modulation frequency of 100 kHz. Spectra were taken under 5 dB of microwave attenuation with a mantissa gain of 1 and an exponential gain of 2. A magnetic field range of 180 mT was swept with a B0-field of 345 mT with a sweep time of 60 s. The relative amount of reduced species present in reduced catalysts was calculated with the area below the spectra (range: 290 to 370 mT) of the different HPA-n_{red} samples.

Transmission-electron microscopy

To analyse the morphology of silver nanoparticles TEM images were captured using a JEOL JEM-2100F microscope operated at 200 kV. The TEM samples were prepared by placing a drop of the colloidal solution onto a carbon-film-coated Cu grid, followed by drying under ambient conditions.

Proton nuclear magnetic resonance

To analyze un-known methylene blue species precipitated during the methylene blue degradation, proton nuclear magnetic resonance measurements were developed. Dry dye solid samples were dissolved in d-Chloroform and measured in a 500 MHz NMR spectrometer (DRX, *Bruker BioSpin GmbH*).

Time-of-flight mass spectroscopy

For analyzing the presence of different methylene blue degradation species, time-of-flight mass spectroscopy (TOF-MS) of samples was conducted. Experiment were taken by introducing the samples via a syringe pump into a quadrupole-time of flight mass spectrometer (Impact II, *Brucker Daltronik*) measured in an APPI ion source at the

High-performance liquid chromatography

To get additional proved of the methylene blue degradation species after reaction, high-performance liquid chromatography analysis was developed. HPLC separation was conducted in a C18 column by infusing the samples at 15 μL/min into an isocratic flow (50 % acetonitrile and 50 % H_2O, with 0.05 % formic acid) mobile phase flow from a Shimadzu UFLC liquid chromatography system. Mobile phase was maintained at 0.5 mL L^{-1}.

Powder X-ray diffraction

Powder X-ray diffraction (XRD) was performed to confirm the presence of Keggin structures on an equipment (STADIP Stoe & Cie GmbH). All measurements were carried out on a flat sample holder in transmission geometry (4–60°/2θ, λ=1,54060 Å, Ge[111]-monochromator), detector: Mythen1K (Dectris, Baden, Switzerland). The experimental X-ray patterns of the three

---

compounds look very similar to each other (Figure A.10). Here, reflections of the compound $H_3PMo_{12}O_{40} \cdot 13\, H_2O$ are present, but additional reflections at about ~6.6, ~8.5, and ~9.9°/2θ cannot be assigned unambiguously without further information about the samples.

5.1. Characterization of the liquid core waveguide membrane optical microreactor

A novel liquid core waveguide membrane microreactor setup for developing *in situ* and/or photoactivated reactions has been described in Section 4.2. In this first section, special focus is given on a complete characterization from an optical (e.g. losses, light transmission) and chemical reaction engineering point of view (e.g. RTD measurements and gas-permeation).

5.1.1. Optical performance

As described in Section 4.4, cut back experiments were carried out to determine the wavelength depended optical losses in a water-filled Teflon AF tube. Figure 25 shows that light transmission losses appear fairly low (1.67 ± 0.70 dB m^{-1} at 575 nm) at wavelengths under 575 nm. For larger wavelengths, the transmission losses increased considerably, as the absorption of water becomes more relevant. Thus, the low losses observed, would allow to detect highly diluted substances through increasing the light-matter interaction even in several meter-long tubes (refer to Figure A.5 in Annex for spectral intensity curves measured in water-filled tubes with different lengths).
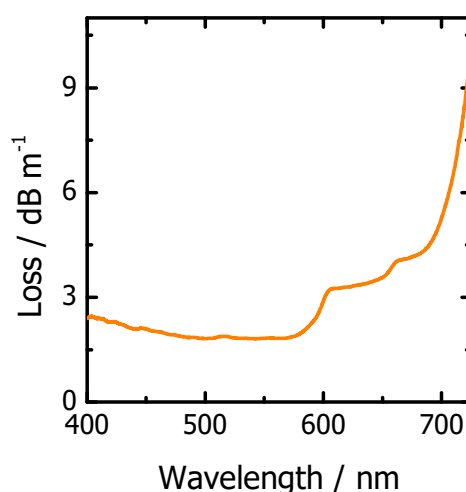
Figure 25. Optical losses at different wavelengths in a water-filled Teflon AF tube. Reprinted with permission from [130]. Copyright 2018 John Wiley and Sons.

To show the setup UV/Vis spectroscopy capabilities, exemplary absorption spectra of two dyes in a broad range (240-900 nm) are depicted in Figure 26a up. This performance was validated through comparing spectra and molar absorption coefficients for Phenol, Acid Orange 7, Azure A and Methylene Blue with data from classical UV/Vis cuvette measurements. The spectra collected in the LCWM reactor and classical UV/Vis spectrometer are in excellent accordance (see exemplary spectra in Figure 26a bottom). Furthermore, the absorption coefficient values at peak maxima (see Figure 26b and values in Table 10) show a linear relation between both systems, which confirms the high accuracy of measurements within the LCWM system. Moreover, a concentration variation from 0.1 to 0.6 µM of MB carried out within the LCWM setup proved the validity of linear calibration following Lambert-Beer's law (see curve in Figure A.3 in Annex).
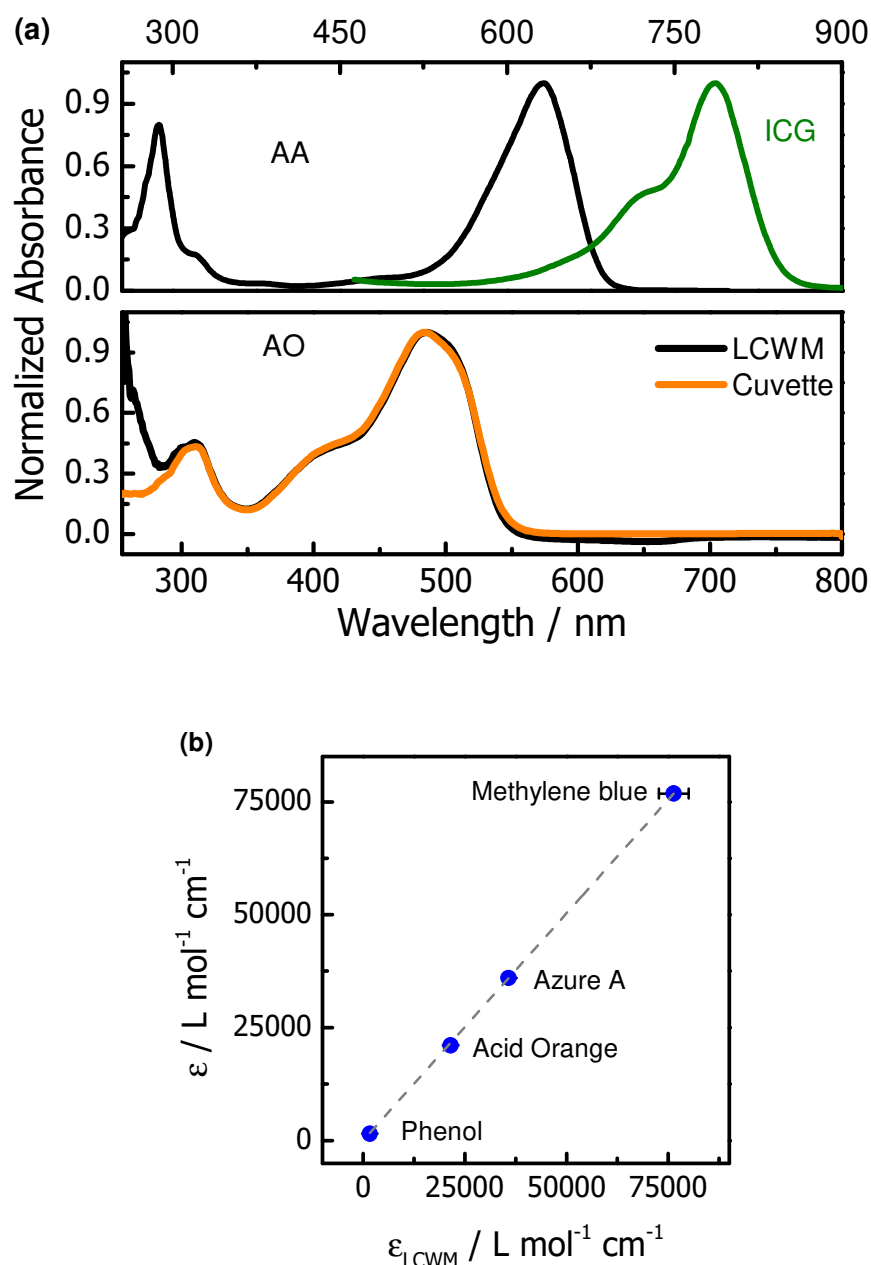
Figure 26. (a) Up: example absorption spectra measurements within the LCWM reactor in the UV-Vis regime, and bottom: exemplary absorption spectra of Acid Orange 7 within the LCWM compared to a conventional spectrometer (1 cm cuvette). Reprinted with permission from [130]. Copyright 2018 John Wiley and Sons. (b) Molar absorption coefficient calculated from a standard spectrometer versus LCWM values for phenol, Acid Orange, Azure A and methylene blue measured at 270, 485, 632, 664 nm. AA: azure A, AO: acid orange 7, ICG: Indocyanine green.

In addition, Figure 27 up exemplary depicts absorption spectra of two organic solvents (methanol and chloroform) to show the setup capabilities for developing measurements at longer wavelengths (Vis-NIR, 600-1500 nm). This is interesting for developing, e.g. high accurate humidity content measurements in ultra-pure solvents. In this case, the setup performance was validated by calculating the absorption coefficient as function of wavelength

(see Equation (27)) for water-filled Teflon AF tubes (Figure 27 bottom) in comparison with literature values at three different wavelengths. As expected, LCWM properties accurately resemble the published values at 760 nm ($\propto_{LCWM}= 0.0213$, $\propto= 0.026$), 970 nm ($\propto_{LCWM}= 0.460$, $\propto= 0.464$) and 1190 nm ($\propto_{LCWM}= 1.540$, $\propto= 1.050$) [131, 132].

Overall, the low loss allows to employ also LCWM length of meters. Nevertheless, the optimal reactor length depends on the concentration and molar absorption coefficients of compounds studied. For highly concentration solutions small length in the lower centimeter length are more likely, on the other hand, for highly diluted solutions long interaction length will lead to optimal absorption spectra results.
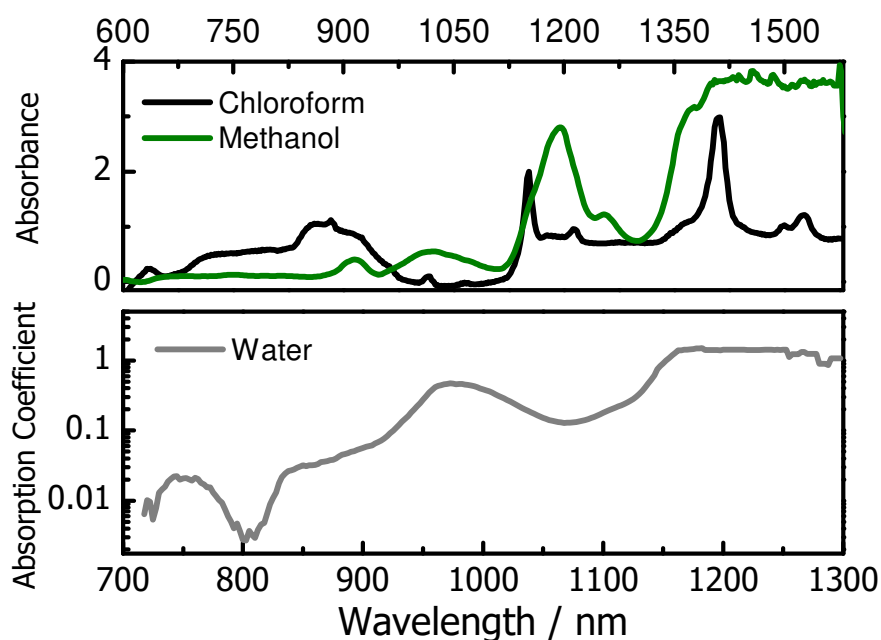
Figure 27. UP: example absorption spectra of Chloroform and Methanol within the LCWM reactor in the Vis-NIR regime. Bottom: calculated absorption coefficient of bi-distilled water on logarithmic scale as function of wavelength in a 6 cm Teflon AF-tube.

Table 10. Calculated molar absorption coefficients for different test substances. The data were obtained from measurements in the LCWM reactor and a conventional spectrometer. Uncertainty of measurements is given as standard deviations for the measurements. Reprinted with permission from [130]. Copyright 2018 John Wiley and Sons

| Substance | Peak maxima (nm) | Molar absorption coefficient (L mol^{-1} cm^{-1}) | |
		Conventional Spectrometer	LCWM
Phenol	270	1542 ± 58	1633 ± 145
Acid Orange	485	21073 ± 237	21537 ± 449
Azure A	632	35996 ± 57	35754 ± 15
Methylene blue	664	76830 ± 493	76419 ± 3670

5.1.2. Residence time distribution

As the flow characteristics inside of the Teflon AF tube can influence significantly degree of conversion and product distribution, RTD measurements were carried out by applying a step input at the pump feedstock. Figure 28 shows the time-dependent concentration distribution of the dye at the inlet and outlet of the Teflon AF tube for all volumetric flows studied. As observed, the inlet signals are not an ideal step signal. Thus, the outlet signals do not show the cumulative function of the Teflon AF tube. Instead, it results from a convolution of the RTDs of the tube before the reactor and the reactor itself.
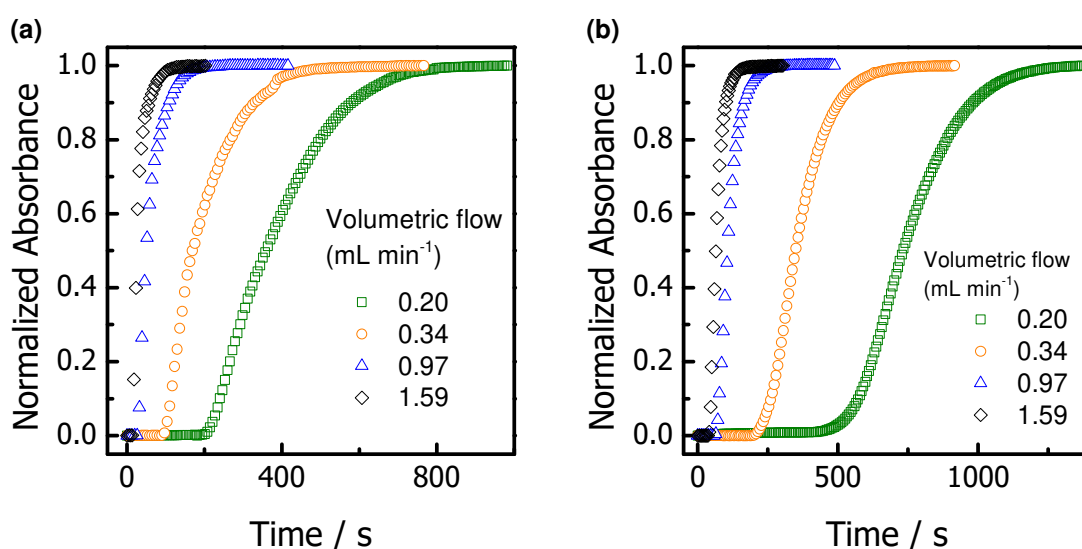
Figure 28. Time-dependent concentration distribution curves measured at the inlet (a) and outlet (b) of the Teflon AF tube from One-Point-measurement setup at different volumetric flows [130].

To obtain the age distributions of the Teflon AF tube (E_{AF}), analytical calculations based on the tank-in-series model and the dispersion model were developed (Please refer to Section 4.5.1 for a detailed explanation). Table 11 lists the resulting number of tanks and Bo values at different volumetric flows. These results show that the Teflon AF tube cannot be considered as an ideal plug flow system, as the calculated Bo and N values are lower than the considered ideal conditions (Bo > 100). Figure 29a confirms this deviation, as the age distribution curves get broader with increasing volumetric flow according to the axial dispersion model (see Figure A.6 in Annex for age distribution curves from the tank-in-series model).

In addition, to verify the suitability of the two models, calculated output signals were obtained by the convolution of the measured inlet signals with the E_{AF} curves and compared with the experimental ones (see Equation (43)). The depicted curves (Figure 29b and Figure A.7 in Annex) show that the RTD in the Teflon AF tube can be well described by the two models in the flow range regime studied.

Table 11. Calculated parameters, which describe the axial dispersion model and the tanks-in-series model, at four different volumetric flows. Reprinted with permission from [130]. Copyright 2018 John Wiley and Sons.

Volumetric flow mL min^{-1}	Tanks-in-series model N	Axial dispersion model Bo
0.20	17	60
0.34	15	53
0.97	9	34
1.59	5	21

$$output\ signal = \int_0^t inlet\ signal\ (t')\ E_{AF}(t-t')dt' \tag{43}$$
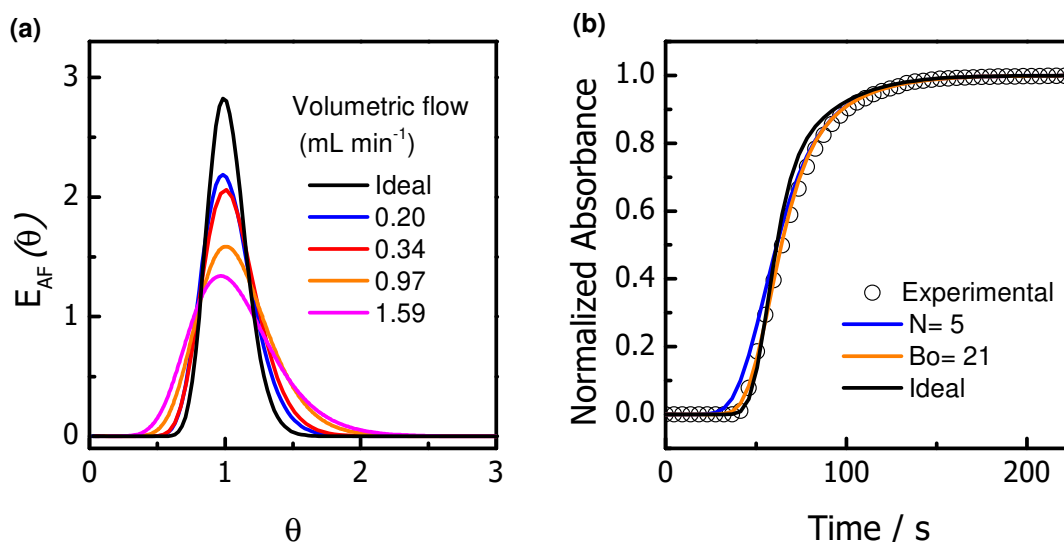
Figure 29. (a) Calculated Teflon AF age distribution curves, $E_{AF}(\theta)$, obtained from the axial dispersion model for all volumetric flows tested, where θ represents the dimensionless time (t/τ). (b) Example step response at the outlet of the Teflon AF tube at a total flow rate of 1.59 mL min^{-1}. Empty circles: experimental results. Lines: Convolution curves with the calculated age distribution curves obtained from a dispersion model with Bo = 21, and a tanks-in series model with a number of tanks N = 5. (Ideal: Bo = 100). Reprinted with permission from [130]. Copyright 2018 John Wiley and Sons.

Conversion and kinetic modelling

In continuous flow experiments, the measured transmission at the outlet fluidic cell (Figure 19b), is the integral spectra of concentration varying with the length of the reactor. Thus, the Lambert-Beer law needs to be solved in parallel with the mass balance, accounting for the reaction rates and the RTD influence. As test reaction, photo-Fenton experiments, resulting in the decolorization of MB, were studied at different residence times. Assuming first-order kinetics the kinetic constants were derived from the experimental data accounting for the measured RTD and assuming ideal plug flow behavior. The calculated paths depicted in Figure 30, show that dispersion can be neglected in the whole flow regime studied, even at high flow rates (low Bo = 34, Figure 30c). As at high flow rates and low Bodenstein numbers the degree of conversion observed is relatively low, the influence of residence time distribution is rather low. Thus, accounting RTD might get important, e.g., for experiments with higher degrees of conversion.
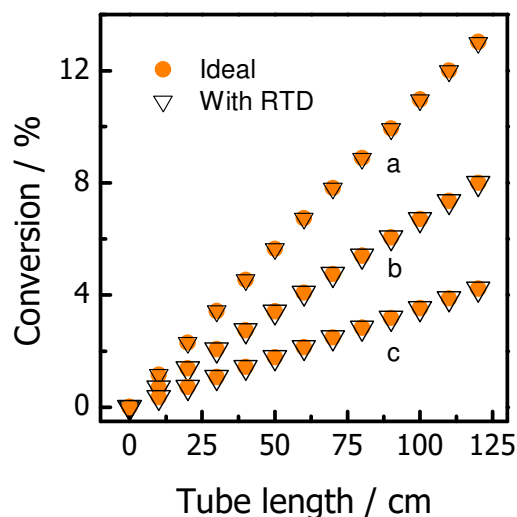
Figure 30. Calculated conversions along a 122 cm Teflon AF tube for an ideal and non-ideal behavior. a. Volumetric flow 0.20, Bo = 60, b. 0.34 mL min^{-1}, Bo = 53, and c. 0.97 mL min^{-1}, Bo = 34. Reprinted with permission from [130]. Copyright 2018 John Wiley and Sons.

5.1.3. Gas permeation in semi-batch and continuous operation

To test the ability of the microreactor for performing *in situ* spectroscopic measurements in semi-batch conditions, the permeation of CO_2 and uptake by water was studied. To detect the CO_2 uptake the color change of a pH indicator (bromocresol purple - BCP) was detected by UV/Vis spectroscopy, where the concentration drop of the basic form (purple color) and the formation of the acidic form (yellow color) can be followed. Figure 31 shows exemplary UV/Vis spectra of those experiments. As expected, BCP spectra shows a clear isosbestic point at approx. 492 nm, which indicates the presence of two species contributing to the overall spectra. Peak at 595 nm track the drop in the basic form, while peak at 432 nm the increase of the acidic form of the dye [59] (see absorbance versus time profiles in Figure 31b). It confirms the permeation of carbon dioxide though the membrane, and further dissolution in the water medium to react and form carbonic acid, reaching nearly equilibrium within 5 minutes.
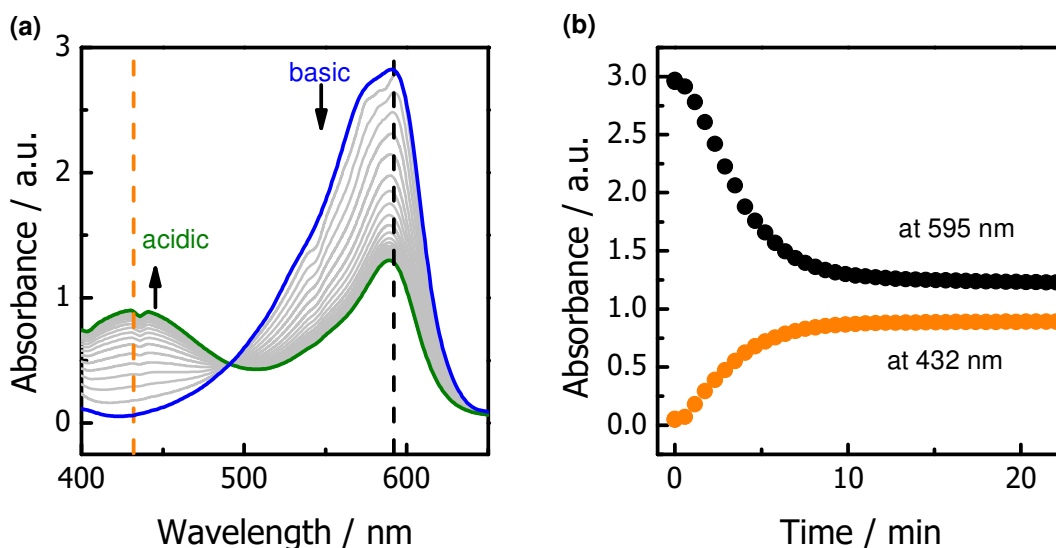
Figure 31. Absorbance spectra of bromocresol purple during the permeation of CO_2 within the Teflon AF tube. (Blue spectra: initial basic form of BCP, and green spectra: acidic form). (b) Absorbance versus time curves at 432 and 595 nm from (a). ***Reaction conditions:*** bromocresol purple as pH indicator (0.8 µM), calcium carbonate as base (initial pH = 10.9), temperature: temperature: room temperature (373 K), gas saturation: 1 bar CO_2.

Operations regime avoiding gas bubbles

Furthermore, according to vast literature concerning tube-in-tube contactors working in continuous flow, Teflon AF tubes show a rather fast gas diffusion across the membrane and flow. Only at very short residence times, a dependency of the dissolved gas concentration on the residence time and concentrations below the solubility limit can be observed. At saturation, most authors report the absence of bubbles [18, 64]. However, this depends of course strongly on the applied pressure difference between gas and liquid phase and the solubility of the gas in the liquid system. As gas bubbles, which can also be difficult to visualize by eye, impede the light transmission, the operational regime for air and N_2 was deduced. Therefore, the residence time as also the gas phase pressure was varied until the loss of light transmission was observed. For a liquid-phase pressure of 2.8 bar Figure 32 shows the work regime, where stable light transmission is still obtained. With shorter residence times higher gas phase pressures are available. It is likely that at this short residence times, the gas-liquid mass transfer through the permeable wall is limiting and thus no full saturation is taking place. At longer residence times the mass transfer seems not to be limiting. When increasing the liquid phase pressure to 7.0 bar with the accessible gas phase pressure of 8 bar not loss of light guidance was observed (see raw experiments in Figure A.9 in Annex).
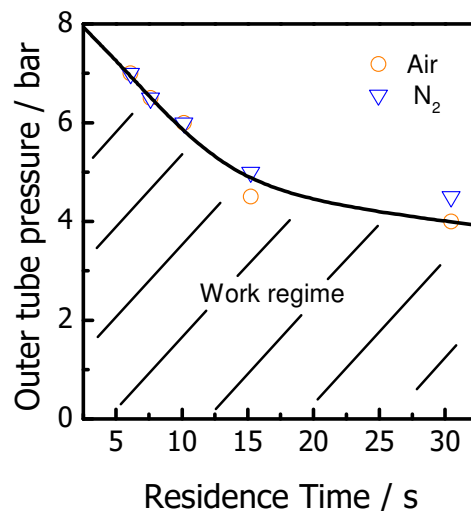
Figure 32. Gas-liquid saturation line, depending on the residence time, at different outer tube (nitrogen and synthetic air) pressures, and a constant 2.8 bar liquid-phase pressure. Reprinted with permission from [130]. Copyright 2018 John Wiley and Sons.

5.1.4. Conclusion

In this section, a first characterization of the optical LCWM microreactor was carried out. The used liquid core waveguide sensor based on Teflon AF obeys the Lambert-Beer's law and transmits light with low optical losses. Residence time distribution experiments and calculations revealed that the Teflon AF tubes diverge from ideal behavior with Bo numbers between 21 and 60, which are important for calculation of kinetic data in continuous flow. In addition, light transmission during gas permeation is supported by the precise control of the liquid-phase pressure avoiding the presence of degassed bubbles in semi-batch (e.g. gas permeation and transient response studies) and continuous operation under homogeneous and heterogeneous reaction systems. As a result, high-resolution measurements and, therefore, trustable and reproducible data of gas-liquid systems can be obtained within the optical LCWM setup.

5.2. Application for *in situ* spectroscopy in homogeneous catalysis: Redox kinetic investigations of Vanadium-substituted heteropolyacids

In this case study, the novel concept of a LCWM microreactor is used to carry out *in situ* UV/Vis spectrometric studies of the reduction and reoxidation kinetics for different vanadium-substituted Keggin-type heteropolyacid catalysts, varying temperatures, substrates and initial catalyst concentrations. Furthermore, cyclic voltammetry and EPR characterization is carried out to support the observations. The combination allowed distinguishing the parallel influence of the vanadium substitution degree on the amount of dissolved and catalytic active V^{4+} species as also on the reduction potential of the HPA itself, which controversially affect the reduction kinetics. Additionally, a huge influence of the substitution degree on the reoxidation rate is deduced.

5.2.1. Influence of vanadium substitution on reduction kinetics

According to Khenkin and Neumann [133], if the reactions are carried out under anaerobic conditions, one might assume the new oxygen atoms in the products originated from the HPA-n (n denotes the number of vanadium substitution) catalysts. Thus, the rates of the reduction step were determined employing fully oxidized HPA-n catalysts under anaerobic conditions, where the reoxidation pathway is suppressed.

The concentration drop of the oxidized (HPA-n_{ox}) as also the formation of the reduced forms (HPA-n_{red}) were monitored via *in situ* UV/vis spectroscopy. Figure 33a depicts an exemplary UV/Vis spectra of a reduction experiment carried out within the LCWM microreactor. Bands under 450 nm (characteristic V^{5+}, and Mo^{6+} bands) allow to follow the drop in HPA-n_{ox}, while bands > 500 nm (heteropoly blues band) the increase in HPA-n_{red}. The 450 nm feature was employed to obtain concentration versus time profiles for the oxidized HPA catalyst. The reduction rate was determined for varying vanadium substitution degrees, initial catalyst concentrations varying from 3 to 14 μM, temperatures ranging from 40 to 80 °C, and using glucose as well as ethylene glycol as a substrate. Such low temperatures are advised to avoid further decomposition of the formic acid. Please note, that within the LCWM experiments especially the HPA catalyst is probed via *in situ* UV/Vis spectroscopy. Product phase analysis is not carried out during this study, but as reference exemplary product distribution obtained from autoclave experiments developed in the Biomass and Sustainable Production of Platform Chemicals group at the University of Erlangen-Nuremberg are given in Annex (see Table A.1).

Figure 33b shows exemplarily for HPA-2$_{ox}$ the reduction of the catalyst at different temperatures and Figure A.11 in Annex show the results for the variation of the initial catalyst concentration.
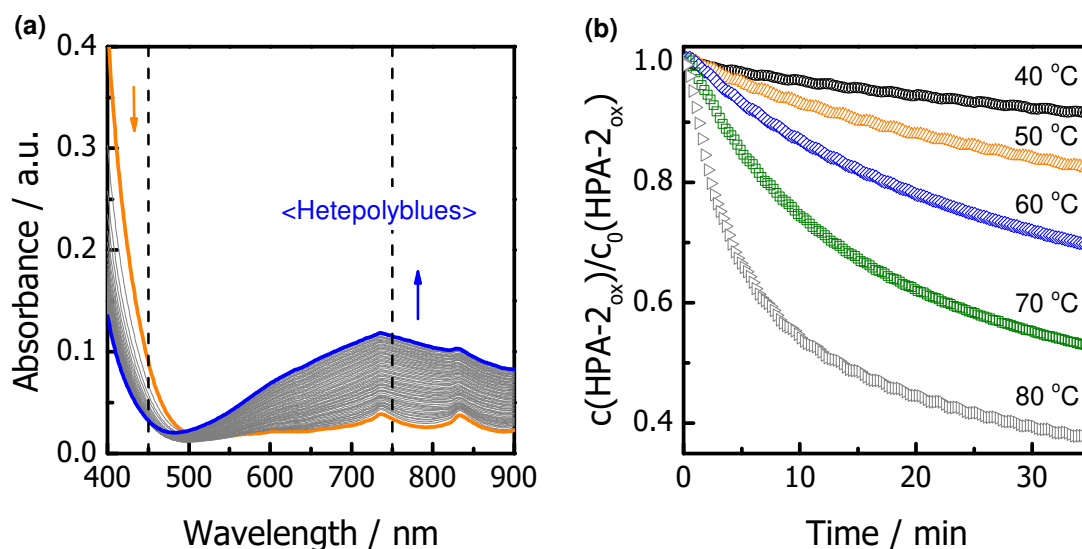
Figure 33. (a) Example absorption spectra during the reduction of a HPA-0$_{ox}$ catalyst. ***Reaction condition***s: HPA-0$_{ox}$ as catalysts (40 μM), D-Glucose as substrate (0.75 mM), temperature: 130 °C, gas saturation: 2 bar N$_2$. (b) Normalized HPA-2$_{ox}$ concentration vs. time curves deduced at 450 nm. ***Reaction conditions:*** HPA-2$_{ox}$ as catalyst (12 μM), D-Glucose as substrate (0.75 mM), temperature: 40 to 80 °C, gas saturation: 2 bar N$_2$. Diagram original source [126].

From the later one, the reaction order regarding the catalyst was determined (see exemplarily for HPA-2$_{ox}$ Figure 34 inset) and from the temperature variation the activation energy (see exemplarily for HPA-2$_{ox}$ Figure 34). For the other catalysts, please refer to Figure A.12 and Figure A.13 in Annex. The kinetic parameters obtained are summarized in Table 12. Despite HPA-1, all catalysts showed a first order in the HPA concentration. HPA-5 presents the highest oxidation rate constant, being almost twice as high compared to HPA-2. While a link between higher V-content and the catalytic activity of the Keggin-type HPAs is obvious, interestingly no linear correlation of activity to substitution degree can be drawn. Especially, HPA-0 shows higher reduction activity compared to HPA-1 and similar activity as HPA-2. Regarding activation energies, HPA-5 and HPA-2 catalysts display similar values in the order of 70 kJ mol^{-1}, which are in agreement with literature [133]. HPA-0 shows a pronounced higher and HPA-1 a pronounced lower activation energy. While the higher activity of HPA-0 can be explained as here Mo is the only redox active metal, the observed lower activation energy for HPA-1 remains unclear in this study.

It needs to be noted that the novel concept of LCWM microreactor proved to suite very well for the kinetic studies. While employing an approx. 10^4 times smaller amount of catalysts, the obtained glucose oxidation rate constants are in excellent accordance with literature reported autoclave reactor studies (for glucose oxidation using HPA-2 catalysts at 80 °C: $k_{red,\ autoclave}$ 0.1 min^{-1} and $k_{red,\ LCWM}$ 0.096 min^{-1}) [86].

Table 12 summarizes the kinetics parameters using ethylene glycol as a substrate. As expected, ethylene glycol reduction rate constants are higher compared to the ones obtained with glucose. However, similar to the glucose system, the HPA-5 catalyst is the most active complex during the substrate oxidation experiments and no linear correlation of substitution degree with activity can be drawn. Interestingly, the activation energies, for all catalysts, show similar values independent of the initial substrate, as both proceed by an electron transfer – oxygen transfer reaction mechanism.
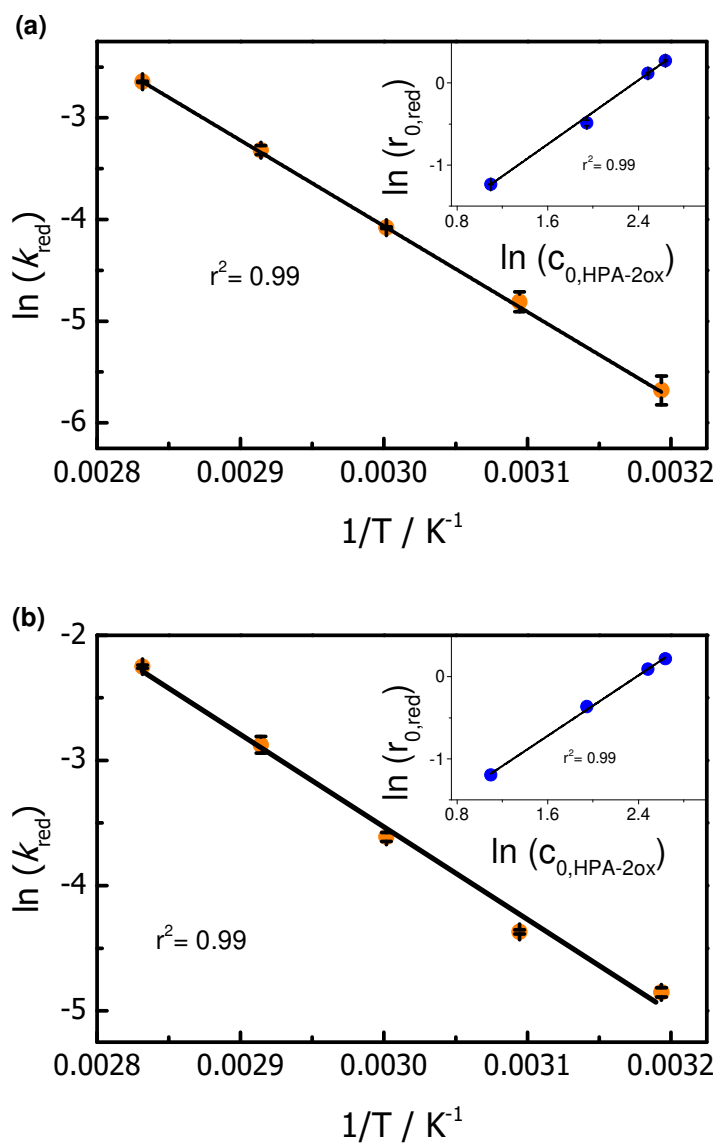
Figure 34. Arrhenius plot for the reduction of HPA-2ox catalyst. (inset) Logarithmic plot of the reduction reaction rate vs. natural logarithm of initial concentration of HPA-2ox catalyst. **_Reaction conditions:_** HPA-2ox as catalyst (3 to 14 µM), (a)D-Glucose as substrate (0.75 mM); (b) Ethylene Glycol as substrate (4 mM), temperature: 40 to 80 °C, gas saturation: 2 bar N_2. Diagrams original source [126].

Table 12. Kinetic data obtained in the LCWM reactor from reduction experiments. Uncertainty of measurements is given as standard deviations for the measurements. Original content [126].

Catalyst	Substrate: D-Glucose			Substrate: Ethylene glycol		
	Effective reaction order (a), at 80 ºC	k_{red}, at 80 ºC (min^{-1})	E_a (kJ mol^{-1})	Effective reaction order (a), at 80 ºC	k_{red}, at 80 ºC (min^{-1})	E_a (kJ mol^{-1})
HPA-0	1.12	0.0878 ± 0.0003	103.95 ± 0.82	1.10	0.138 ± 0.044	101.48 ± 1.49
HPA-1	1.60	0.0381 ± 0.0138	33.66 ± 0.94	1.39	0.068 ± 0.033	34.12 ± 2.24
HPA-2	0.98	0.0966 ± 0.0050	70.30 ± 1.38	0.92	0.114 ± 0.002	61.47 ± 0.66
HPA-5	0.89	0.2223 ± 0.0199	70.82 ± 1.87	0.92	0.304 ± 0.076	68.74 ± 0.48

Correlation between redox properties and catalytic activity

To understand the reason for the non-linear response of reduction rate to vanadium substitution the redox properties of each catalyst were electrochemically characterized. Following Park et al., the first electron reduction potential of HPA-n catalysts can be used as representative redox potential of the heteropolyanions [134, 135]. Figure A.14a in Annex shows the cyclic voltammograms of HPA-n catalysts with resulting electrochemical reduction potentials listed in Table 13. Comparing the electrochemical reduction potential of all catalysts, it decreases in the order HPA-0 > HPA-1 > HPA-2 > HPA-5 and in an almost linear manner, which is in accordance with literature [136].

Figure 35a correlates the reduction rate constant at 80 ºC using glucose as a substrate with the electrochemical reduction potential and clearly no direct correlation results. This atypical behaviour could be explained by the mechanism of reaction proposed by several authors [76, 83, 84] (please refer to Section 2.3.1 for a detailed explanation), which suggest that the greater oxidation activity of highly V-substituted complexes is influenced by the presence of very active pervanadyl ions dissolved in the acidic reaction medium. These ions oxidize the substrate and form a free vanadyl ion, which stays dissolved in the reaction medium. To confirm this behaviour in our reaction system, the amount of V-reduced species (V^{4+}) present in HPA-n$_{red}$ catalysts was detected by EPR measurements (Figure 35b). Accordingly, HPA-5$_{red}$ catalysts show 2.1 times higher V^{4+} content than HPA-2$_{red}$ complexes. This value is in great accordance to the initial V-content between both catalysts determined by ICP-OES (2.42), and further correlates to the higher reduction rate constant of HPA-5 compared to HPA-2 (2.3).
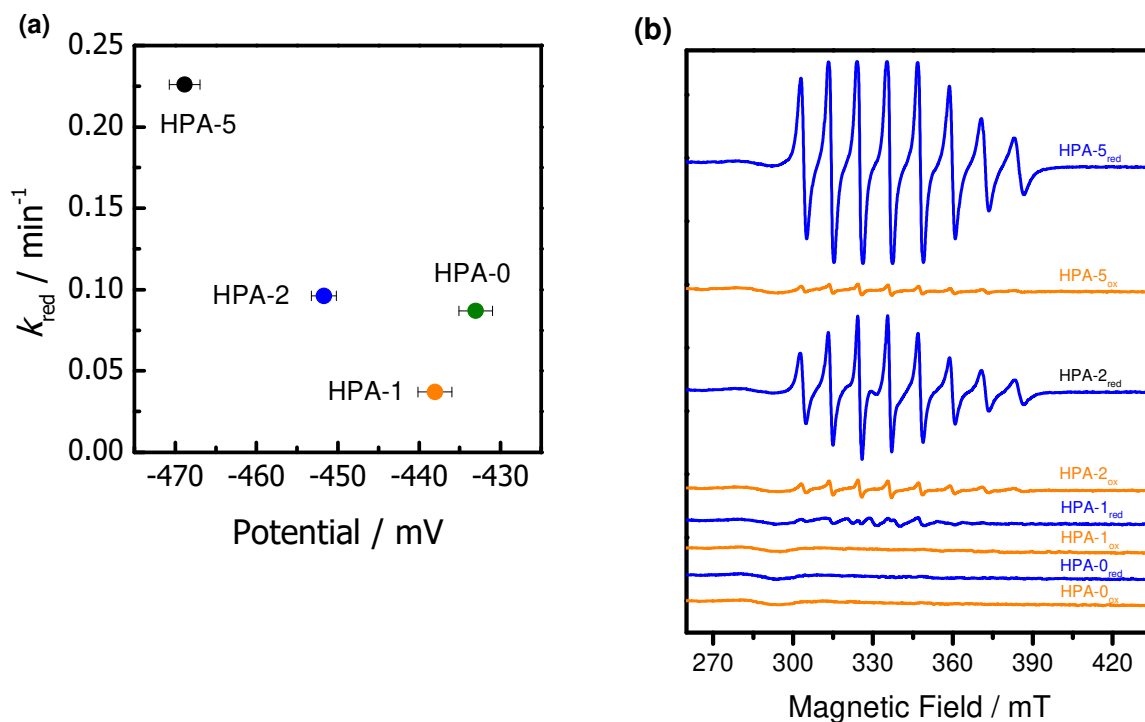
Figure 35. (a) Correlations between reduction rate constants at 80 °C and glucose as substrate and reduction potential of the HPA-n catalysts. (b) EPR spectra of HPA-n catalysts in their oxidized and reduced forms. Diagrams original source [126].

However, on the other hand, poor V-substituted catalysts (e.g. HPA-0$_{red}$ and HPA-1$_{red}$) show almost a negligible amount of V^{4+} species dissolved in the reacted medium, in spite of showing reduction activity. Therefore, a direct correlation between V-content and reactivity cannot be made for the whole catalysts. Most likely, the activity results are stemming from two active sites: i) dissolved vanadium oxidized (V^{5+}) species, and ii) the HPA itself. In this sense, the activity of HPA-0 and HPA-1 stems mostly from the heteropolyanions as active species itself. Furthermore, the activity of the HPA as active site seems to drop with increasing vanadium substitution, due to the changed redox properties. For HPA-2 and HPA-5, additional V^{5+} seems to be present as active site. While the activity of the V^{5+} site is probably not influenced by the vanadium substitution, the total number of active V^{5+} species depends on the substitution degree. For HPA-2 and HPA-5 this seems to be the major effect on activity. In summary, the opposing influence of vanadium substitution on the activity of the HPA active site as also a number of V^{5+} active sites can explain the observed reduction activity trend HPA-1 < HPA-0 HPA-2 < HPA-5 very well.

Finally, the different active sites seem to affect not only the kinetics, but also their selectivity towards the products. As previously reported in [76], from autoclave experiments, poorly V-

substituted catalysts show higher selectivity towards CO_2 and higher V-substituted ones towards formic acid. It can be speculated that the V^{5+} active sites more selectively show a one-electron transfer mechanism, which could favour the production of formic acid. Instead, the HPA as multielectron-oxidant active site can tend to overoxidize the glucose to form CO_2 [80].

Table 13. Kinetic data obtained, reduction potential values, and calculated EPR areas of different V- substituted HPA- n catalysts. Uncertainty of measurements is given as standard deviations for the measurements. Original content [126].

Catalysts	CV	EPR measurements
	First reduction potential (mV)	Area (a.u.)
HPA-0	-433.03 ± 2.07	0
HPA-1	-438.03 ± 2.08	5321
HPA-2	-451.70 ± 1.54	110755
HPA-5	-468.83 ± 1.92	2352790

5.2.2. Influence of vanadium substitution in reoxidation kinetics

Even though the reoxidation step (Figure 6b) plays an important role in the overall reaction, just few is known about the interaction of HPA-n_{red} complexes with oxygen. Hence, transient response experiments with pre-reduced HPA-n catalysts were performed, to deduce the reoxidation kinetics. Therefore, the gas phase component was switched fast from nitrogen to air. The fast gas-liquid mass transfer of this reactor concept, which needs due to the gas-liquid contactor no dispersed gas bubbles, allows for this kinetic experiment not possible in a classical autoclave study.

The UV/Vis spectra of the fully reduced HPA-n_{red} catalysts is obtained initially and discussed first of all (see blue spectra in

Figure 36a). A characteristic broad absorption band typical for the so-called "heteropoly blues" is observed. Nevertheless, for the HPA-0_{red}, a characteristic broad peak centered at 750 nm results (blue spectra in Figure A.14b), which is related to homo-intervalence-charge-transfer-bands (IVCT) of Mo-O-Mo groups. On the other hand, for V-substituted catalysts, this peak appears less pronounced (Figure 36a) indicating also the presence of hetero-IVCT of a V-O-Mo group [76, 137]. Interestingly, for V-substituted HPAs$_{red}$ measured at the same molar

concentration, the overall absorption intensity increases with higher vanadium substitution content. This behaviour most likely is related to the major presence of vanadyl species dissolved in the reaction medium after catalyst reduction, as described above.
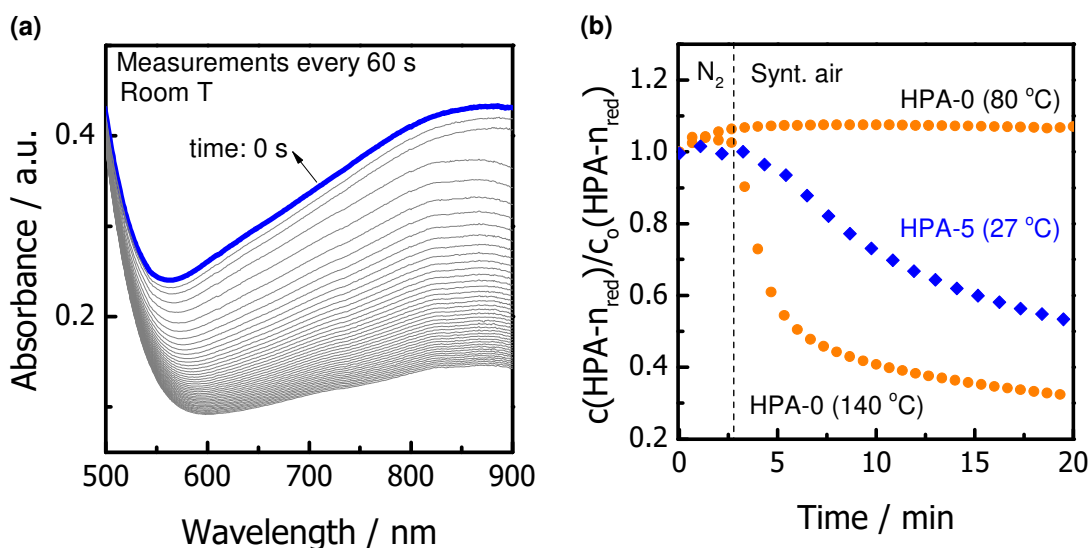
Figure 36. Example absorption spectra during the reoxidation of HPA-0$_{red}$ catalyst. ***Reaction conditions***: (a) HPA-5$_{ox}$ as catalysts (20 µM), temperature: 27 °C, gas saturation: 5 bar synthetic air. (c) Normalized concentration-time profiles at 750 nm of the reoxidation of HPA-n$_{red}$ catalysts. ***Reaction conditions:*** HPA-0$_{red}$ (20 µM), HPA-5$_{red}$ (16 µM), temperature: 25 to 140 °C, gas saturation: 5 bar synthetic air. Diagrams original source [126].

Figure 36a shows the dynamic change in the UV/Vis spectra after starting the transient response experiment and changing the gas from N$_2$ to synthetic air. Similar behaviour was observed for HPA-2$_{red}$ complexes and both show reoxidation activity at room temperature. As expected, HPA-0$_{red}$ and HPA-1$_{red}$ catalysts showed no tendency to reoxidize at this low temperature. Their reoxidation mechanism which is supposed to be thermodynamically unfavourable [80], is known to be different from that of the higher-substituted HPA-n and seems not to depend on the oxygen concentration. To confirm this claim, reoxidation experiments at higher temperatures (up to 150 °C), keeping air saturation constant, were carried out. The reoxidation of unsubstituted HPA-0$_{red}$ and poor substituted HPA-1$_{red}$ catalyst started to be observable at liquid-phase temperatures over 100 °C (see Figure A.14b in Annex). In all cases, time depended disappearance of the broad bands is observed, and the wavelength at 750 nm was employed to deduce the concentration-time profiles (see exemplary profiles in the

Figure 36b). From this, initial reactions rates for the reoxidation of HPA-n$_{red}$ were deduced and further evaluated for activation energies and reaction orders for the catalyst. From the

experiments a clear activity trend for the reoxidation following HPA‑0 < HPA‑1 < HPA‑2 < HPA‑5 and thus a direct correlation with the vanadium substitution can be seen.

While due the strong activity differences the study for HPA-0 and HPA-1 needed to be carried out at 120 to 150 °C and for HPA-2 and HPA-5 at < 80 °C similarities in the kinetic parameters can be observed (see Table 14). The reaction order with respect to the concentration was determined by plotting the initial reaction rate versus the initial concentration of HPA-n_{red} (Figure 37 a and b). Independent on the vanadium substitution, the reoxidation reactions resulted to be first-order in the HPA-n_{red}. Regarding the activation energy for HPA-0 and HPA-1 a similar value of 20 kJ mol^{-1} results (Figure 37c). With higher substitution degrees a dependency is observed, and the activation energy increases to 24 and 28 kJ mol^{-1} for HPA-2 and HPA-5, respectively.

It needs to be noted that qualitatively a difference in the reoxidation activity of the HPA-5 and HPA-2 catalyst was deduced also from autoclave experiments and is inline with our findings [76]. In autoclave experiments an indirect conclusion on the reoxidation step was carried out from the dependency of the overall reaction rate (influence by the reduction and reoxidation step) on the oxygen pressure dependency. It was observed that 60 bar of oxygen pressure are required to ensure that the reoxidation step is not any more the rate-determining using HPA-2, while only 30 bar for HPA-5 complexes is required [86]. Within this study and the possibility for transient response experiments quantitative kinetic data also of the reoxidation step could be deduced. From this it can be stated that HPA-5$_{red}$ shows a 10 times faster initial reoxidation reaction compared to HPA-2$_{red}$.
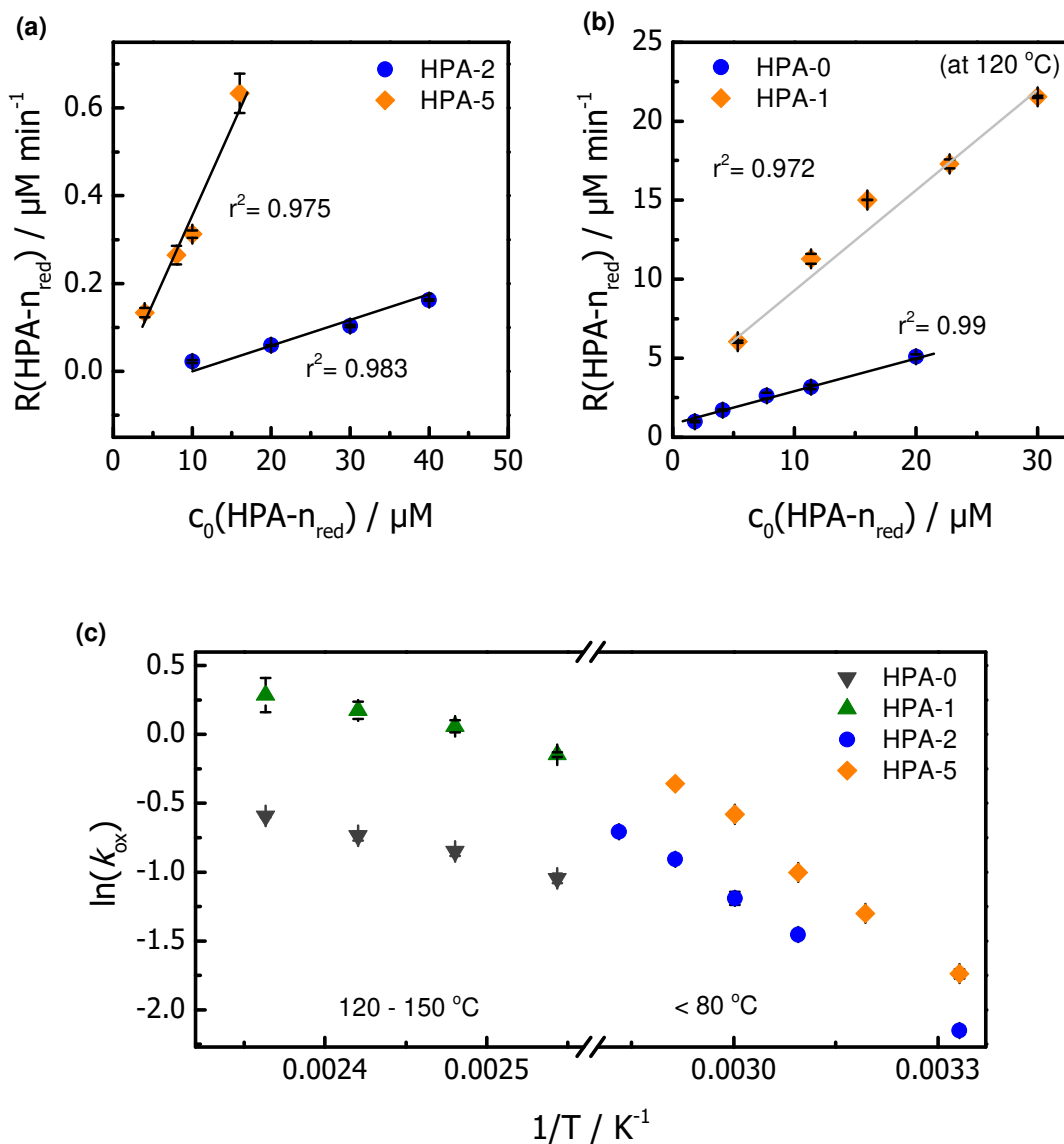
Figure 37. Initial reaction rates vs. initial concentration of HPA-n_{red} catalysts. (a) HPA-5$_{red}$ and HPA-2$_{red}$ at 27 °C, and (b) HPA-0$_{red}$ and HPA-1$_{red}$ at 27 °C. ***Reaction conditions:*** HPA-n_{red} (4 to 40 μM), gas saturation: 5 bar synthetic air. (c) Arrhenius plot for the reoxidation of HPA-n_{red} catalysts. ***Reaction conditions:*** HPA-n_{red} as catalysts (10 to 40 μM), temperature: 27 to 150 °C, gas saturation: 5 bar synthetic air. Diagrams original source [126].

Table 14. Kinetic data obtained in the LCWM reactor from reoxidation experiments. Uncertainty of measurements is given as standard deviations for the measurements. Original content [126].

Catalysts	Reaction order, at 27 °C	k_{ox}, at 27 °C (min^{-1})	E_a, (kJ mol^{-1}) < 80 °C	Reaction order, at 120 °C	k_{ox}, at 120 °C (min^{-1})	E_a, (kJ mol^{-1}) 120-150 °C
HPA-0	-	-	-	0.99	0.219 ± 0.005	20.43 ± 0.85
HPA-1	-	-	-	0.97	0.604 ± 0.009	19.40 ± 2.16
HPA-2	0.98	0.0047 ± 0.0002	24.03 ± 1.06	-	-	-
HPA-5	0.98	0.0418 ± 0.0026	28.15 ± 0.46	-	-	-

5.2.3. Conclusion

It has been demonstrated that the developed LCWM reactor concept suits excellent for kinetic *in situ* UV/Vis studies of gas-liquid homogeneous catalytic reactions. For the HPA catalyst conversion of glucose to formic acid the kinetics of the reduction as also the reoxidation step within the catalytic cycle were deduced. The results are consistent with observations of the overall reaction rate (determined by the full catalytic cycle) carried out in autoclave reactor experiments (30-60 bar O_2, hours), but using 10^4 times lesser amount of catalyst, lower pressure (2-5 bar), and shorter time scales (min). While the autoclave experiments allow only for qualitative interpretation especially of the reoxidation kinetics, the transient response experiment possible with the LCWM reactor allowed to deduce quantitative kinetic information.

The studies of the reduction step kinetics in combination with EPR and electrochemical characterization revealed that two active sites can promote this step. On the one hand, dissolved VO_2^+, seems to be an active site and on the other hand the heteropolyanion itself. While the activity of the heteroplyanions as active site itself seem to slow down with higher V-substitution degree, the amount of highly active VO_2^+ dissolved increases with higher substitution. The detrimental effect of vanadium substitution on activity and number of active sites explains the observed reduction activity trend as also selectivity patterns reported in literature. The kinetic study of the reoxidation step showed that non-substituted and one times substituted HPA-0 and HPA-1 catalyst are only reoxidized above 100 °C and due to the decomposition of formic acid at high temperatures not suitable for this reaction. In contrary HPA-2 and HPA-5 showed suitable reoxidation below 80 °C, while HPA-5 shows at 27 °C a 10 times higher reoxidation rate compared to HPA-2. This quantitative true kinetic data of both reaction steps of different vanadium substituted HPA catalysts can allow for further catalyst and process optimization, with the aim to reduce the process temperature, as also oxygen pressure needed for the reoxidation step.

5.3. Application for studying photoactivated reactions: Methylene blue degradation in alkaline solutions

In this case study the LCWM microreactor concept is employed to disentangle the complex reaction network occurring, when photoactivated and non-photo reactions overlay. As a model system, the well-known redox cycle of methylene blue and leucomethylene blue was chosen. Within the study the possibility of the LCWM microreactor to exchange the gas atmosphere from anaerobic to aerobic conditions fast, *in situ* UV/Vis spectroscopy, as also variation of the light illumination time was employed. This allowed to deduce a complex interplay of several reaction pathways and to propose a new reaction network, which can account for all observed effects.

5.3.1. Influence of photoactivated reactions on methylene blue redox cycle in alkali

Within the LCWM reactor the individual steps of the main MB ↔ LMB cycle can be decoupled. Please refer to Section 7.3 Figure A. 15 in Annex for an exemplary transient response experiment within the LCWM reactor in a MB/NaBH$_4$ solution. In this experiment, the MB → LMB reduction is studied by applying anaerobic conditions. Switching to aerobic conditions by exchanging N$_2$ with synthetic air allows to study the oxidation step LMB → MB. For our case study (MB-glucose in alkali), Figure 38a top shows such an experiment carried out at pH 11. The depletion of MB under anaerobic conditions and the full recovery of MB under aerobic conditions can be observed. While this experiment was carried out with minimal light exposure and only view spectra taken (approx. 10 % of reaction time was with light exposure) an experiment with continuous light exposure is given in Figure 38a bottom. In the direct comparison, it can be seen clearly that for continuous illumination in the air exposure step, MB is not fully recovered. As the only difference between both experiments is the light exposure, it gets clear that this observation is not due to unsuccessful reoxidation of LMB (see example in Figure A. 15), but must stem from additional non-reversible photoactivated reactions. The same set of experiments was carried out at more alkaline conditions (pH 12.5) and is shown in Figure 38b. Here already for the minimal light exposure no full recovery is observed. Even more, the MB recovered with air, shows no stable concentration but even under air a continuous drop in concentration. For continuous light exposure the MB recovery rate under air is clearly lower (e.g. comparing point x with y in Figure 38b), indicating again that photoactivated reactions take place.
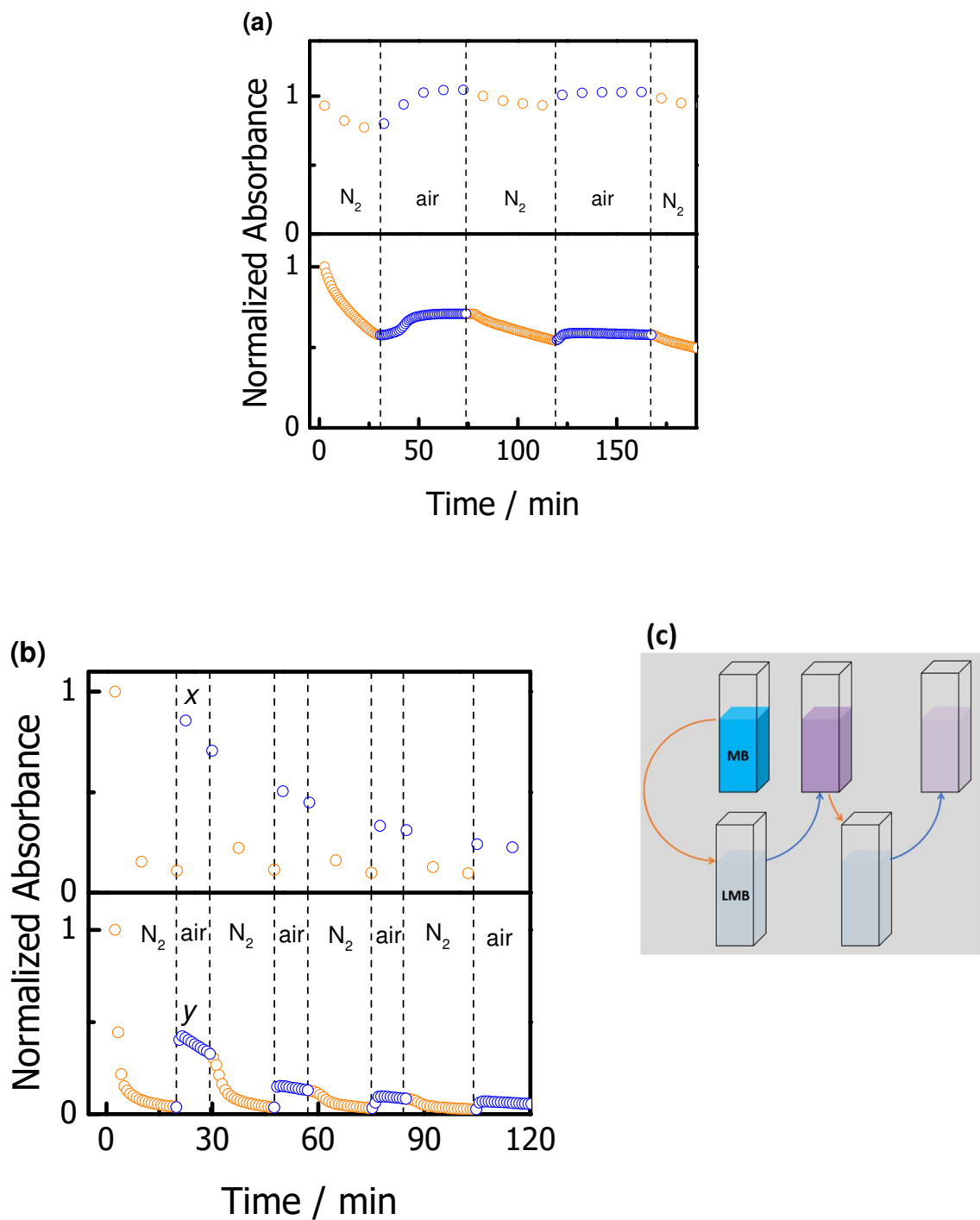
Figure 38. Normalized absorbance at MB absorption maxima (664 nm) vs. time for an experiment with anaerobic and aerobic conditions and different initial substrates concentrations. ***Reaction conditions***: (a) MB (0.6 µM), glucose (0.5 mM), NaOH (1 mM), pH = 11, temperature: 27 °C, gas saturation: N$_2$ ←→ synth. air (b) MB (0.6 µM), glucose (50 mM), NaOH (100 mM), pH = 12.5, temperature: 27 °C, gas saturation: N2 ←→ synth. air (Up: short term interval irradiation, and bottom: continuous light irradiation). (c) Schematic representation of MB degradation taking place in b.

5.3.2. Possible intermediates and side products formed

After proofing the occurrence of photoenhanced side reactions the obtained product spectra are studied to identify possible reaction pathways. Figure 39a shows the absorption spectra of pristine MB together with the spectra corresponding to point x and y in Figure 38b, where additional products of side reactions must be present. Clearly the spectra changes and despite MB additional species are detected. A characteristic shift of the absorption maxima to lower values (hyposochromic/blue shift) with respect to the MB reference can be observed. Furthermore, additional bands below 600 nm evolve (hatched region in Figure 39). Figure 39a shows also the spectra resulting for continuous light exposure for MB at pH 12.5 under anaerobic conditions, but without glucose as reducing agent. The blue shift and bands evolving below 600 nm can also be clearly seen for this experiment. While these alterations can be observed in literature for the direct MB decomposition in alkaline solutions [138], and the MB photocatalytic degradation under UV and/or Vis light irradiation [94, 100], their effect on the absorption spectra are commonly not accounted [102].

Katafias et al.[98] showed in a study employing HPLC and UV/Vis spectroscopy that the protonated forms of MVB, Azures A, B, C and Thionin (AA, AB, AC, TH) are degradation compounds of MB in alkaline hydrogen peroxide solution. Possible side reactions leading to these compounds can be the N-demethylation of MB, due to the nucleophilic attack of OH⁻ ions enhanced by light, which leads to AA, AB, AC, and TH. Also, the deamination can take place to result in MVB. Spectra for these compounds are given in Figure 39 b & c. It gets obvious, that these side products could explain the blue shift, but fails to explain the pronounced new bands evolving below 600 nm.

To get more evidence if additional products despite AA, AB, AC, TH and MVB are responsible for the new bands below 600 nm mass spectroscopy (see Figure 40a) and HPLC characterization (see Figure 40b) were carried out. The solution which shows the features most pronounced (alkaline MB solutions without glucose, irradiated continuously with light; Figure 39a), was taken for the additional characterization. Major MS peaks were observed at m/z = 284.13, 270.10, 257.07, 256.09, 242.07 and 228.06, which can be correlated to MB, AB, MVB, AC, AA and TH, respectively. Similar results were obtained by HPLC, however highly N-demethylated products such as AC, and TH were difficult to separate fully. All in all, no-evidence to the presence of new species was found.
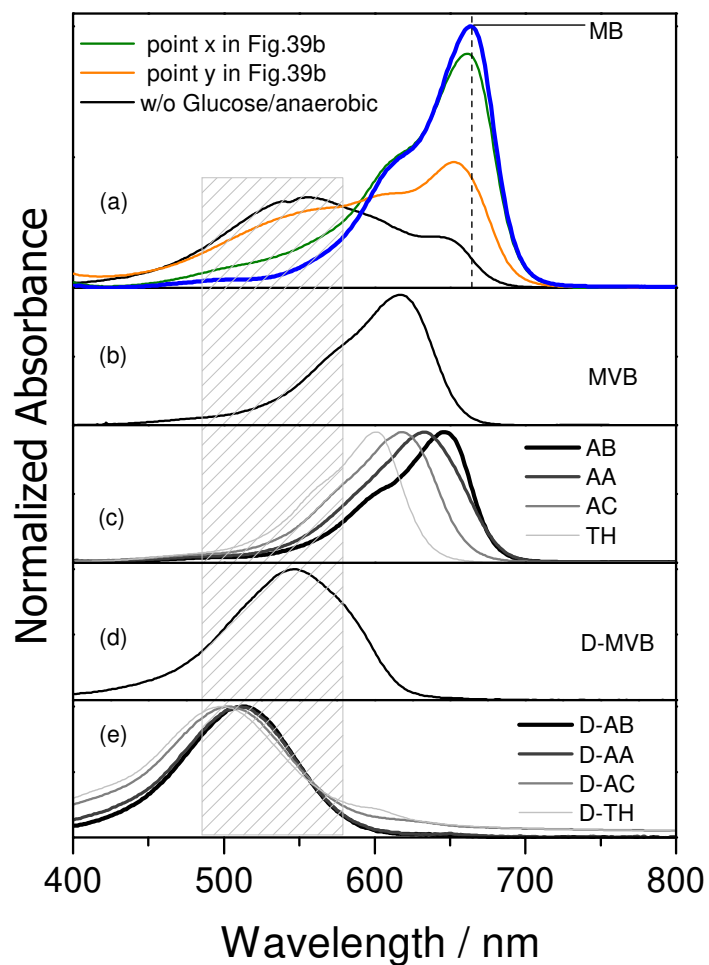
Figure 39. (a) Initial MB normalized absorption spectra compared to spectra taken after 20 min and corresponding to point x and y of Figure 38b, and an experiment without glucose in anaerobic conditions. (b & c) Absorption spectra of known MB-degradation derivatives dissolved in water. (d & e) Deprotonated (D-) absorption spectra of known MB-degradation derivatives dissolved in acetone.
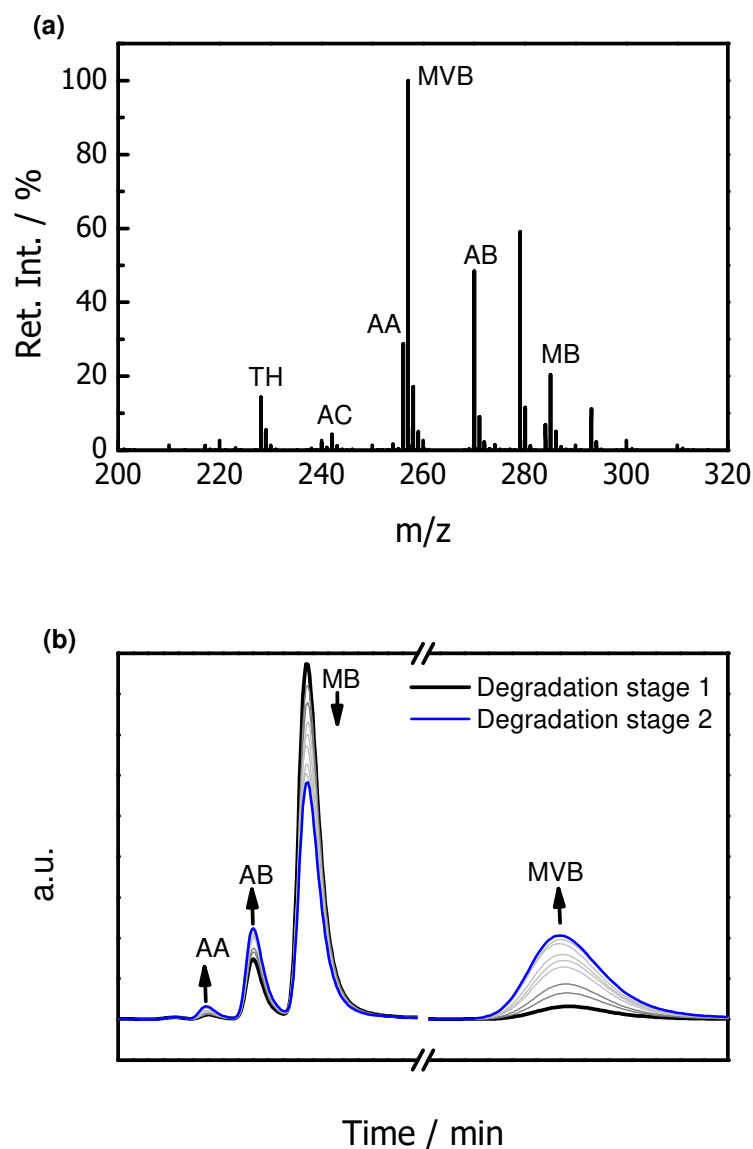
Figure 40. (a) MS-spectra of species produced by MB in alkali (pH = 12.5) after 30 min of reaction time. (b) HPLC separation of species produced in alkaline methylene blue (pH = 12.5) taken at different degradation stages.

Other studies investigating, *e.g.* the alkaline degradation pathway reported also UV/Vis spectra with absorption maxima < 600 nm and showed that these can belong to deprotonated water immiscible species [89, 99]. To enforce the precipitation of possible species with low solubility, the initial concentration of MB was increased from 0.6 μM to a maximum of 50 μM, which led to the formation of a solid sediment. NMR spectroscopy of the precipitate redissolved in chloroform perfectly match to the spectra reference of MVB (see Figure 41). While the spectra of protonated MVB (Figure 39b) cannot be responsible for the features observed below 600 nm, the deprotonated form could be responsible [89]. To get further evidence, MVB, as also AA, AB, AC and TH, was dissolved in acetone, to obtain spectra of the deprotonated form. The spectra

clearly fit to the features observed below 600 nm (Figure 39 d and e). Due to the similarity of the spectra for the deprotonated compounds, and missing reference spectra in highly alkaline aqueous phase (stability problem), a further deconvolution of the spectra accounting for all deprotonated species cannot be carried out easily. While the NMR characterization suggests that especially deprotonated MVB is present, it cannot be fully clarified if not also AA, AB, AC and TH deprotonated species are present. Therefore, in the further evaluation all deprotonated compounds are summarized to deprotonated-species (D-species), without further specification.
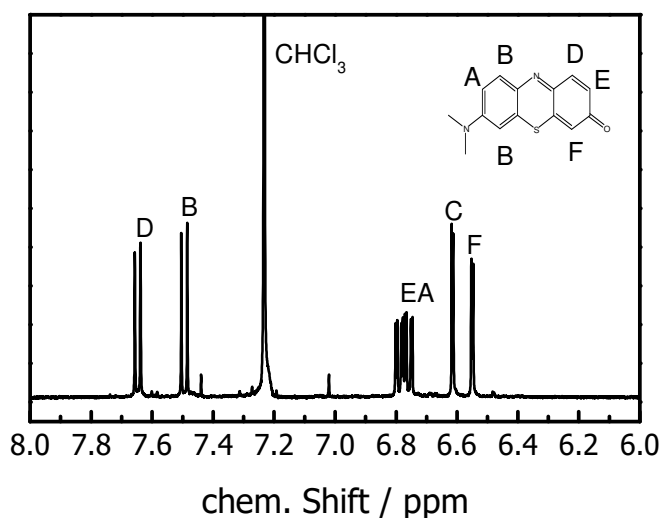
Figure 41. ¹H-NMR spectra of a dry sediment dissolved in chloroform.

5.3.3. Temporal change of species for experiments in anaerobic and aerobic conditions

Based on the identified species, the obtained spectra were deconvoluted to derive semi-quantitative time dependent information. The analysis is regarded to be semi-quantitative as the deprotonated species could not be calibrated. They are accounted only roughly through a single broad Gaussian peak. Figure 42 shows exemplarily the fit resulting for the spectra, which shows the highest content of D-species (pH 12.5 MB solution without glucose and degraded under continuous illumination). While a reasonable fit results, it is also clear that the single Gaussian leads also to a rough quantification, and can falsify also the quantitative result for MVB or the azure compounds.
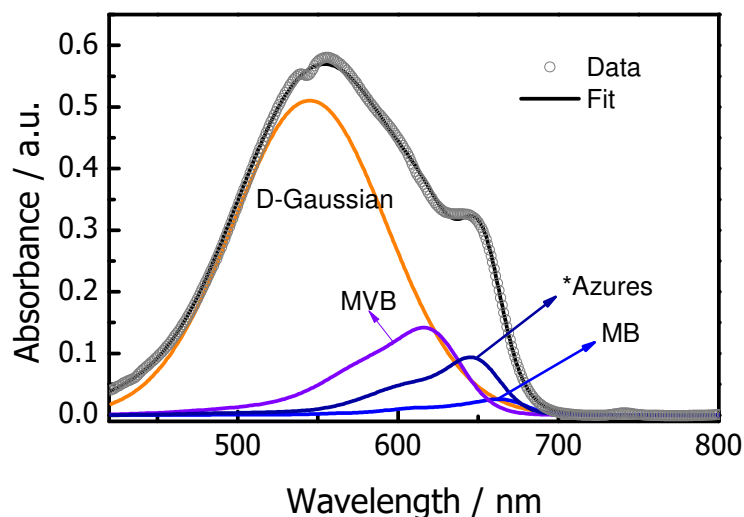
Figure 42. Spectra deconvolution of a continuous experiment in an alkaline MB (pH = 12.5) solution in N_2 environment at 20 min reaction time in a 52 cm LCWM reactor. *Azures: it refers principally to AB and very small traces of further N-demethylated species.

Despite the limitations of the fitting, the semi-quantitative analysis of the spectra can be used to obtain further insights on the temporal evolution of the different species. Figure 43a gives the resulting temporal changes for anaerobic conditions (note that for the roughly fitted sum of D-species no concentration is given, but the change in fitted area). The figure shows that MB reacts away very fast in the first 10 mins. The two major compounds observed are MVB resulting from mono-deamination and D-species. Varying the pH during the experiment shows a strong influence on formation of D-species (Figure 43b). With pH 11 nearly no D-species are observed. Interestingly, pH 12 gives already a pronounced amount, further increasing with increasing the pH to 13. The sharp increase of D-species above pH 11 can be correlated to the pKa values of the azure compounds, which is from 11.5 to 12.1.
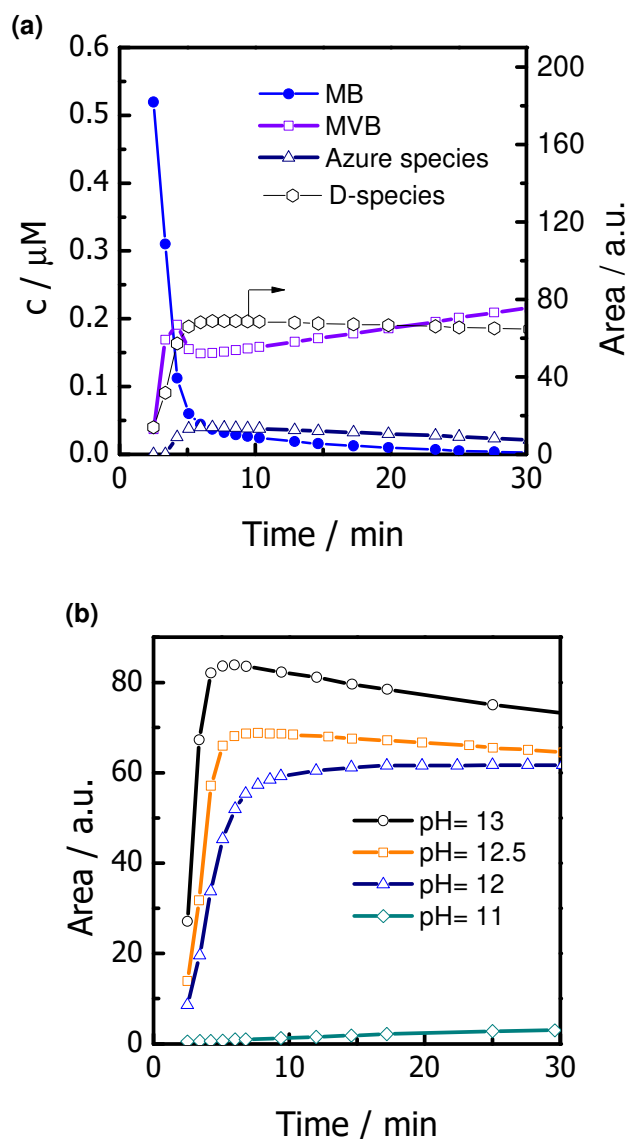
Figure 43. (a) Concentration vs. time curve for different MB-derivatives obtained by spectra deconvolution at anaerobic conditions, pH = 12.5 (right axis: area of the D-Gaussian curves which represent all deprotonated species. (b) Area vs. time curves of D-species dissolved in the aqueous media at different pH values at anaerobic conditions. *Reaction conditions*: MB (0.6 µM), glucose (50 mM), NaOH (1.25-200 mM), pH = 11-13, temperature: 27 °C, gas saturation: 3 bar N_2.

To further study the influence of oxygen on the degradation pathway, studies at pH 13 and aerobic conditions were carried out. Figure 44 and b compares the development of the spectra at anaerobic and aerobic conditions, while Figure 45 gives the temporal evolution of the spectra with time. As discussed prior, for anaerobic conditions very fast D-species are obtained. Furthermore, it can be seen that these compounds degrade slowly in consecutive reactions and the mixture becomes translucent. In contrast, under aerobic conditions clearly less N-demethylation products (azure species and their deprotonated forms) are observed. Again a

consecutive degradation towards non-UV/Vis-active compounds takes place, while an increase in rate of this secondary reaction is observed.

As oxygen itself can not oxidize the dyes at the applied conditions at this high rate, the higher degrading rate must be based on an photoactivated oxidation process. MB is known to act as a photosensitizer and most likely the excited triple-state form (MB*(3)) is involved [95]. MB*(3) forms from the excited singlet state (MB*(1)) through the intersystem-crossing mechanism, and could interact with oxygen for enhanced degradation by two different mechanisms: i) electron-transfer with a substrate, yielding free radicals and finally superoxide ions, and ii) by the direct formation of singlet oxygen from triplet oxygen with MB*(3) as photosensitizer, which is known to be hundred times faster than mechanism i.[96]. Thus, the second pathway could explain the suppression of azure species at aerobic conditions. These species are likely to be formed from the excited MB*(3) intermediate. If singlet oxygen is reacting with MB*(3) as a photosensitizer, it can reduce the lifetime of the intermediate towards the azure species in a competitive parallel reaction dramatically. Due to this observation the second mechanism is seen to take place more likely in the studied system.
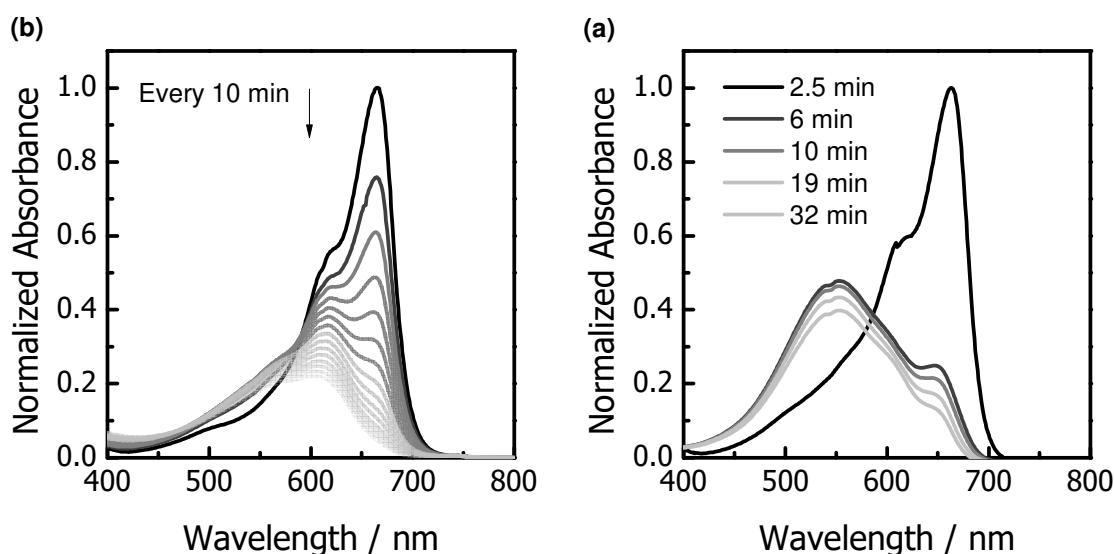
Figure 44. Spectral changes recorded for MB in alkaline solution (pH = 13) with continuous light irradiation in (a) anaerobic (N_2), and (b) aerobic conditions (synth. Air). **_Reaction conditions_**: MB (0.6 µM), glucose (50 mM), NaOH (200 mM), pH = 13, temperature: 27 °C, gas saturation: 3 bar (N_2 and synth. air).
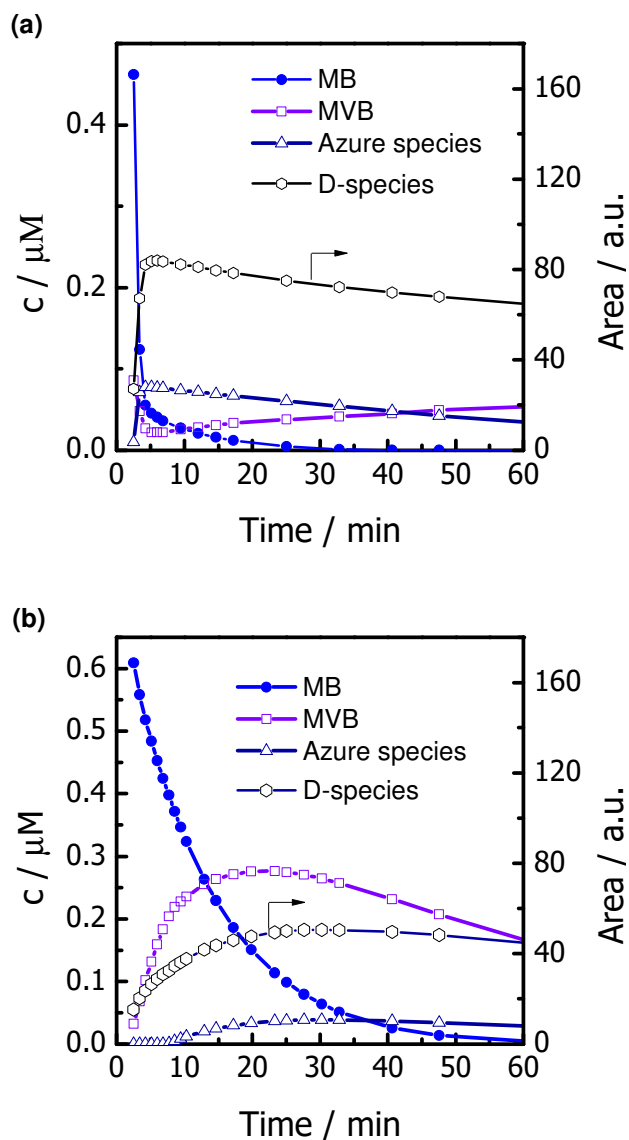
Figure 45. Concentration vs. time curves by spectra deconvolution of MB in alkaline solution (pH = 13) with continuous light irradiation under (a) anaerobic (N_2), and (b) aerobic conditions. ***Reaction conditions***: MB (0.6 µM), glucose (50 mM), NaOH (200 mM), pH = 13, temperature: 27 °C, gas saturation: 3 bar (N_2 and synth. air).

5.3.4. Conclusion

In this application, we have proved the suitability of the LCWM microreactor concept as a promising tool for studying *in situ* complex gas-liquid light redox reactions. The reactor allows exchanging the gas atmosphere fast, measuring *in situ* high resolution UV/Vis spectra, controlling intense light-matter interaction, and detecting ultra-low concentrations, advantages not easily achieved with conventional photo-reactors. Thus, the system should find wide application, enabling rapid investigation of complex reaction networks in photochemistry.

Furthermore, a reaction network accounting for all studied effects is proposed and summarized in Figure 46. The proposed reaction network starts with the well-known non-photoactivated MB ←→ LMB redox cycle. With MB as common intermediate the redox cycle is connected to a photosensitizer cycle, leading to MB in an excited triple state (MB*(3)). Under anaerobic conditions MB*(3) undergoes mainly deamination and N-demethylation. The corresponding MVB and azure species can further deprotonate, depending on the pKa of the species and the pH of the solution. Under aerobic conditions MB*(3) can interact with triplet oxygen to form singlet oxygen. Thereby, the fast reaction with oxygen seems to suppress the deamination and N-demethylation reactions, and the photosensitizer cycle is a major source for fast mineralization of all organic compounds in solution. All of these findings should therefore shed light into ambiguous interactions usually faced when MB acts as substrate, sensitizer or both.
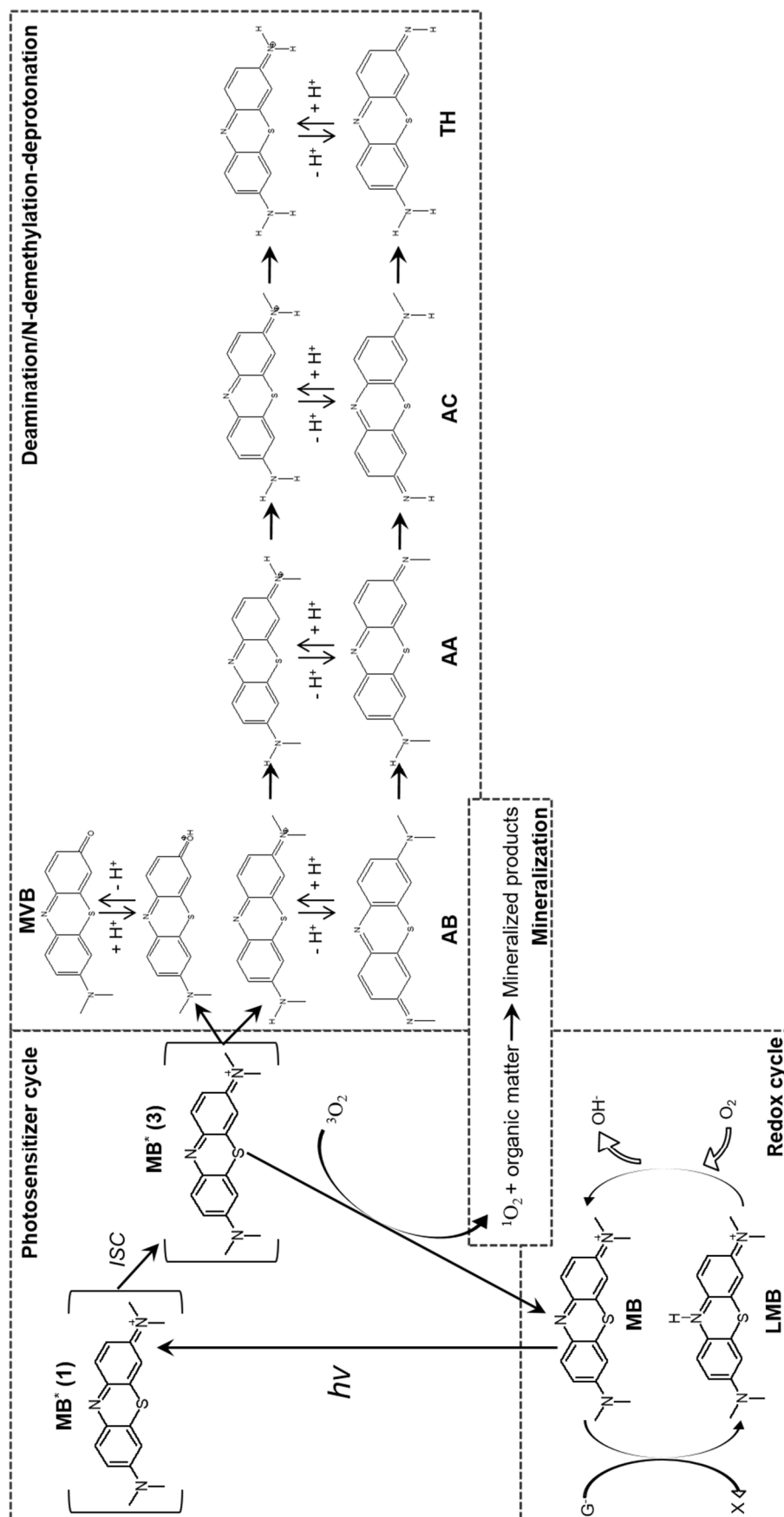
Figure 46. Summary of possible reactions in a photoenhanced MB redox cycle in alkali at anaerobic and aerobic conditions within the LCWM optical microreactor.

5.4. Application for studying photochemical transformations of colloidal particles: Silver nanoparticles degradation

In this case study not homogeneous liquid systems (with dissolved gas phase), but a colloidal suspension of nanoparticles is studied. As the studied AgNP colloids exhibit surface-plasmon resonance (SPR) absorbance dependent on their size, shape, and distribution [115], changes of these properties can be detected by *in situ* UV/Vis spectroscopy within the LCWM reactor. AgNPs are known to interact with oxygen, and suffer photochemical transformations [112, 114, 119, 120] under light irradiation and here the kinetics and mechanisms of NP transformation are studied for varying atmospheres (N$_2$, air), different light irradiation (UV, Vis, UV-Vis), citrate concentration, and temperature.

5.4.1. Silver nanoparticle photooxidation kinetics

It is well-known that silver nanoparticles are not persistent in environments containing dissolved oxygen. It leads to the formation of Ag$^+$ and/or its complexes (e.g. Ag$_2$S, Ag$_3$(citrate), etc.) at the NP surface, which can further dissolved in the aqueous medium [111-113]. It has been also shown that this oxidation process can be enhanced, if the NPs are photoexcited by light irradiation (photooxidation) [139, 140]. Thus, the stability of AgNP colloids (c$_{TSC}$=0.2 mM, see Table 9 in Section 4.8) under UV light irradiation was first studied. Figure 47 shows such experiments carried out under anaerobic (a) and aerobic (b) conditions within the LCWM setup. A steady SPR intensity decrement depending on the exposure time can be observed, while samples in dark conditions did not show any changes within weeks of storage. In both LCWM experiments, possible agglomeration, coalescence, or sedimentation are neglected, as minor shifts on the absorption spectra, and stable light transmission were observed. Thus, decolorization can be directly related to a photooxidation process, as demonstrated by Gorham et al. in UV-irradiated colloid-filled Quartz vials (7 mL) [116]. To determine the photooxidation kinetics, the normalized SPR absorption at the initial peak maxima (≈398 nm) as function of time was plotted (Figure 47c). AgNPs photooxidation by UV light under aerobic conditions follows an exponential decay, indicating a pseudo-first order kinetic mechanism. Compared to aerobic conditions the anaerobic experiment shows after approx. 60 % of total degradation a strong deviation from a first order degradation profile (see Figure 47c blue points). In addition, for the initial degradation the rate constant under nitrogen is almost half compared to the one under air atmosphere (see Table 15). Reason for this observation could be oxygen trapped on

the nanoparticles during the synthesis process (i.e. aging step), which is consumed and gradually depleted by the photoexcited NPs, limiting the whole reaction.

Under aerobic conditions experiments were carried out at different air saturation pressures (1 - 5 bar), and showed nearly no dependency on the kinetic constant (see Figure A.19a). Thus, minor oxygen present seems to be sufficient for the reaction, and probably saturates the NP surface very fast. Moreover, photooxidation experiments with temperature variation from 27 to 80 ºC under aerobic conditions were carried out. As the spectra stay unaltered (see example at 80 ºC in Figure 49a up) no agglomeration or variation on the optical properties was observed, and even at higher temperatures, the photooxidation process seems to be the major degradation process. From the temperature variation an activation energy for the photooxidation under UV irradiation of 18 kJ mol^{-1} was calculated (see Arrhenius plot in Figure A.19b in Annex.)

Additionally, the effect of capping agent on the AgNPs photooxidation was studied by varying its concentration. Figure 48 shows a quasi-exponential decline of the photooxidation kinetic constants while increasing the initial concentration of the capping agent TSC during the synthesis. A dramatic 90 % difference between the lowest (0.2 mM) and highest (8 mM) concentrations is observed (see values in Table 15). As shown in Figure 24 in the Experimental Section, surface-plasmon resonance properties are not quite affected depending on the initial citrate concentration. Thus, the fading should be mostly related to a surface shielding effect against dissolved oxygen in solution. This is in good accordance with literature [114] where citrate is used to control the release of biological active (i.e. Ag$^+$) species from the AgNPs surface.
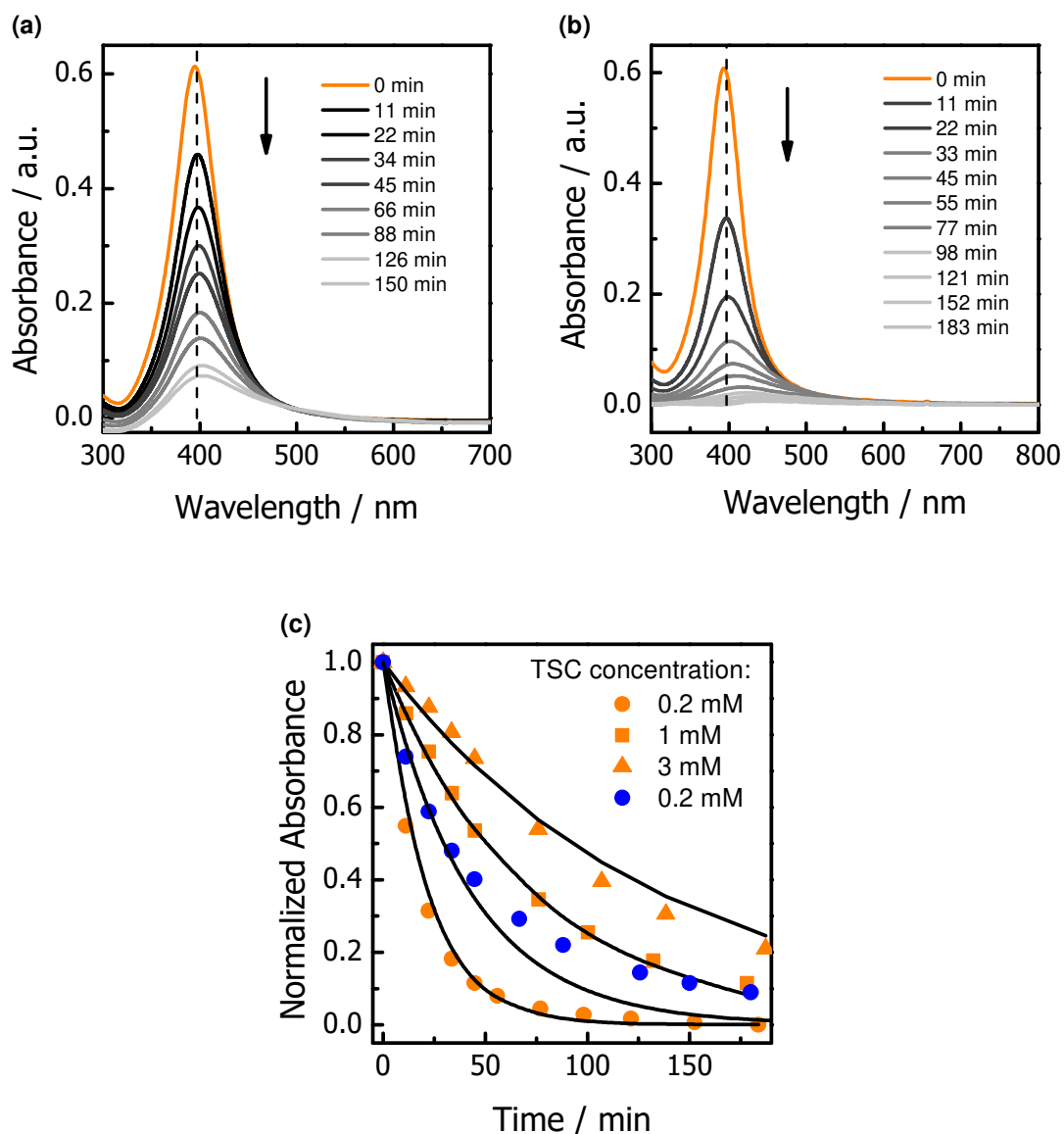
Figure 47. Example absorption spectra of the photooxidation of AgNP colloids under (a) anaerobic, and (b) aerobic conditions. *Reaction conditions:* TSC (0.2 mM), temperature: 27 °C, irradiation: UV (deuterium lamp), gas saturation: 3 bar (N_2, synth. air). (c) Normalized absorbance-time profiles (symbols) at 398 nm, and fitting to a first-order reaction kinetic model (lines) of the photooxidation within the LCWM microreactor. *Reaction conditions:* TSC (0.2 – 3 mM), temperature: 27 °C, irradiation: UV (deuterium lamp), gas saturation: 3 bar N_2 (blue) or synth. air (orange).
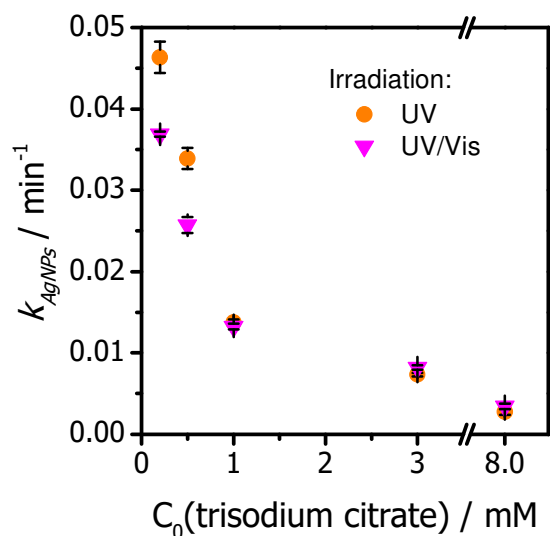
Figure 48. Photooxidation kinetic constants vs. initial tri-sodium citrate concentrations of AgNP colloids measured in the LCWM microreactor. **Reaction conditions:** TSC (0.2 – 8 mM), temperature: 27 °C, irradiation: UV (deuterium lamp), UV-Vis (deuterium and halogen lamp), gas saturation: 3 bar (N_2, synth. Air).

Table 15. Kinetic data obtained in the LCWM microreactor from photooxidation of AgNP colloid experiments. Uncertainty of measurements is given as standard deviations for the measurements.

c_{TSC} (mM)	$k_{(UV-air)}$	$k_{(UV-N2)}$ (min $^{-1}$)	$k_{(UV-Vis air)}$
0.2	0.0464 ± 0.0019	0.0210 ± 0.0006	0.0369 ± 0.0002
0.5	0.0339 ± 0.0013	-	0.0257 ± 0.0009
1	0.0138 ± 0.0003	-	0.0133 ± 0.0003
3	0.0074 ± 0.0002	-	0.0082 ± 0.0002
8	0.0028 ± 0.0003	-	0.0034 ± 0.0003

5.4.2. Influence of irradiation in the visible regime

While in the prior subsection only UV irradiation (deuterium lamp) was applied, here also irradiating within the visible regime (deuterium + halogen lamp, spectra of sources see Figure A. 18 in Annex) is employed under aerobic conditions. Kinetic data (see Figure 48b and Table 15) show a small decrement (20 %) in the rate of photooxidation for colloids with 0.2 and 0.5 mM TSC concentration compared to the studies under solely UV-irradiation. As the only difference between both experiments is the visible light irradiation, it gets clear that this difference must stem from a competing process triggered by lower frequency wavelengths. To get more evidence about this additional reaction pathway, Figure 49 a and b shows the

absorption spectra of experiments developed at 80 °C and UV and UV/Vis irradiation under aerobic conditions. In contrast to experiments developed under UV irradiation (Figure 49a top), baseline distortion under UV/Vis irradiation is observed (Figure 49b top). To avoid effects of baseline distortion, the first-order derivative spectra was calculated (Figure 49b bottom). Same calculation was developed for the experiment under UV irradiation for comparison (Figure 49a bottom). Similarities between them, prove that both experiments are indeed a photooxidation process, being UV/Vis experiments almost 10 times slower. It is known that citrate stabilized AgNPs irradiated by light in the Vis-NIR range, slowly tend to the formation of bigger aggregates through the photo-voltage mechanism [119]. The overall reaction is the indirect photooxidation of citrate by O_2, catalyzed by metallic silver. From this reaction, electrons are injected into the particle, which finally induce the reduction and deposition of Ag^0 growing newer NP shapes [119] (see a more detailed explanation in Section 2.5.2). This mechanism could explain both the baseline distortion, and the slower degradation rates observed. Citrate oxidation products, such as acetone ($\eta_{acetone}$=1.36) (see Eq. (25)), could vary the index of refraction of the medium. Hence, more light would be transmitted compared to the water background (i.e. base line distortion), emerging negative absorbance. Moreover, slower kinetics will result by the two competing mechanism of reaction, which are the oxidation (fast) and reduction (slow) of silver ions at the nanoparticle surface.
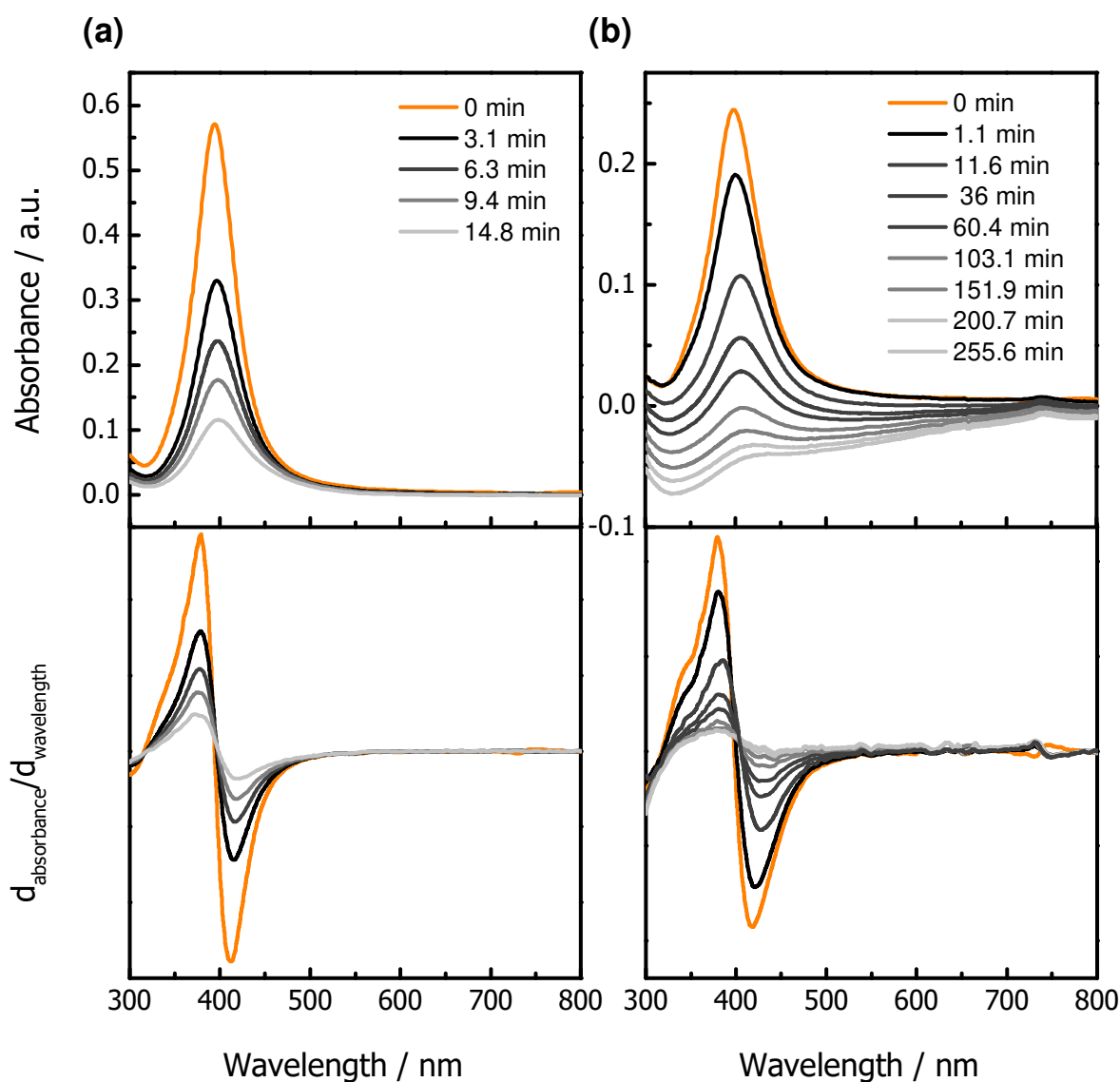
Figure 49. (Up) Example absorption spectra of the photodegradation of AgNP colloids under aerobic conditions. (Bottom) First-order derivative spectra. ***Reaction conditions:*** TSC (0.2 mM), temperature: 80 °C, irradiation: (a) UV (deuterium lamp), and (b) UV/Vis (deuterium and halogen lamp), gas saturation: 3 bar synth. air.

Finally experiments under aerobic and anaerobic conditions, but only under visible light irradiation were carried out. As with the absence of UV irradiation the photooxidation is slowed down, the experiments give more insights into the slower nanoparticle aggregation. Under aerobic conditions, a small red shift of the SPR peak maxima is observed (see Figure A.20). This deviation is more evident under nitrogen saturated systems, as depicted in Figure 50a. After a 24 hours experiment, a considerable red shift of ≈ 20 nm was obtained (see Figure 50b), which is normally related to the formation of bigger particles in the colloidal solution [117, 141]. As product phase analysis is not carried out within this study for semi-batch experiments, the Mie model was used as a predictive tool for particle size by fitting the UV/Vis spectra recorded

within the LCWM microreactor (see curves in Figure 51). The calculations were based on the published work by Wu et al. [129]. The model resembles calculated values from TEM images, as shown in Figure 23 in the Experimental Section. As expected, the red shift in the spectra (Figure 50b left axis) is a consequence of nanoparticle diameter increment, keeping more or less a spherical shape (values in Figure 50b right axis). However, under longer periods of irradiation (> 11 hours), the NP start to loss their spherical shape properties to the formation of undetermined bigger clusters. This effect can be observed in Figure 51 b and c where the Mie model cannot accurately fit the SPR spectra anymore.

In summary, the broad light irradiation under citrate-AgNPs colloids will include two competing processes, which are highly dependent on the gas saturation. On the one side, the photooxidation of Ag^0 from the NP surface, and on the other side, the indirect reduction of Ag^+ by citrate, which leads to NPs growth.
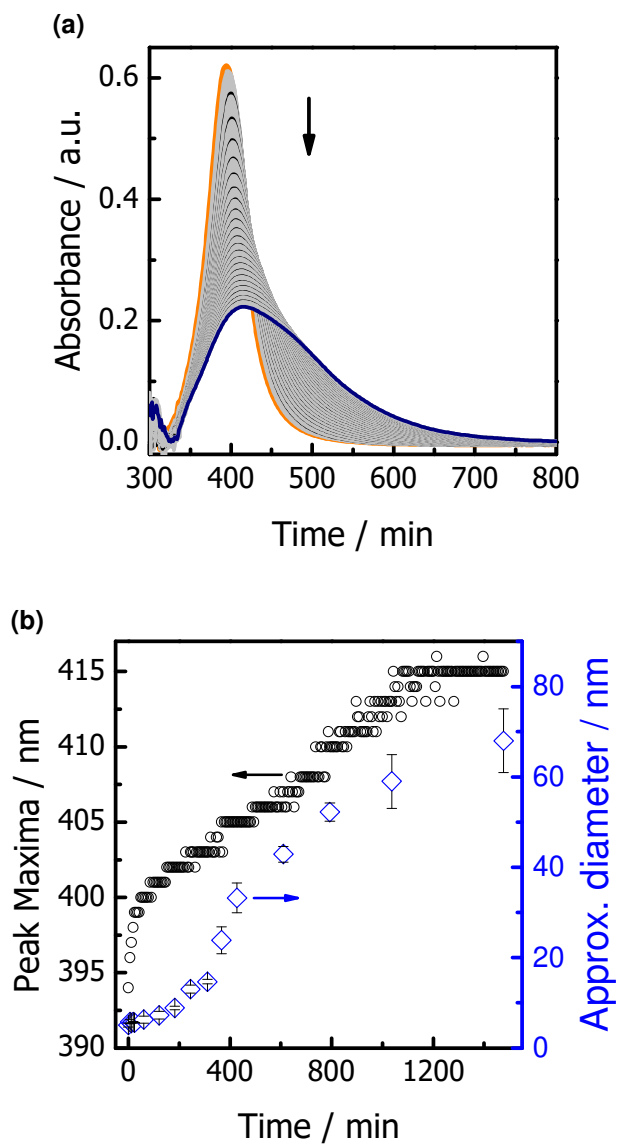
Figure 50. (a) Example absorption spectra of the photooxidation and aggregation of AgNP colloids. Measurements taken every 360 s. Dark lines guide the eye every hour. (b) Peak maxima and approx. diameter versus time of measurements developed in (a). *Reaction conditions:* TSC (0.2 mM), temperature: 27 °C, irradiation: Vis (halogen lamp), gas saturation: 3 bar N_2.
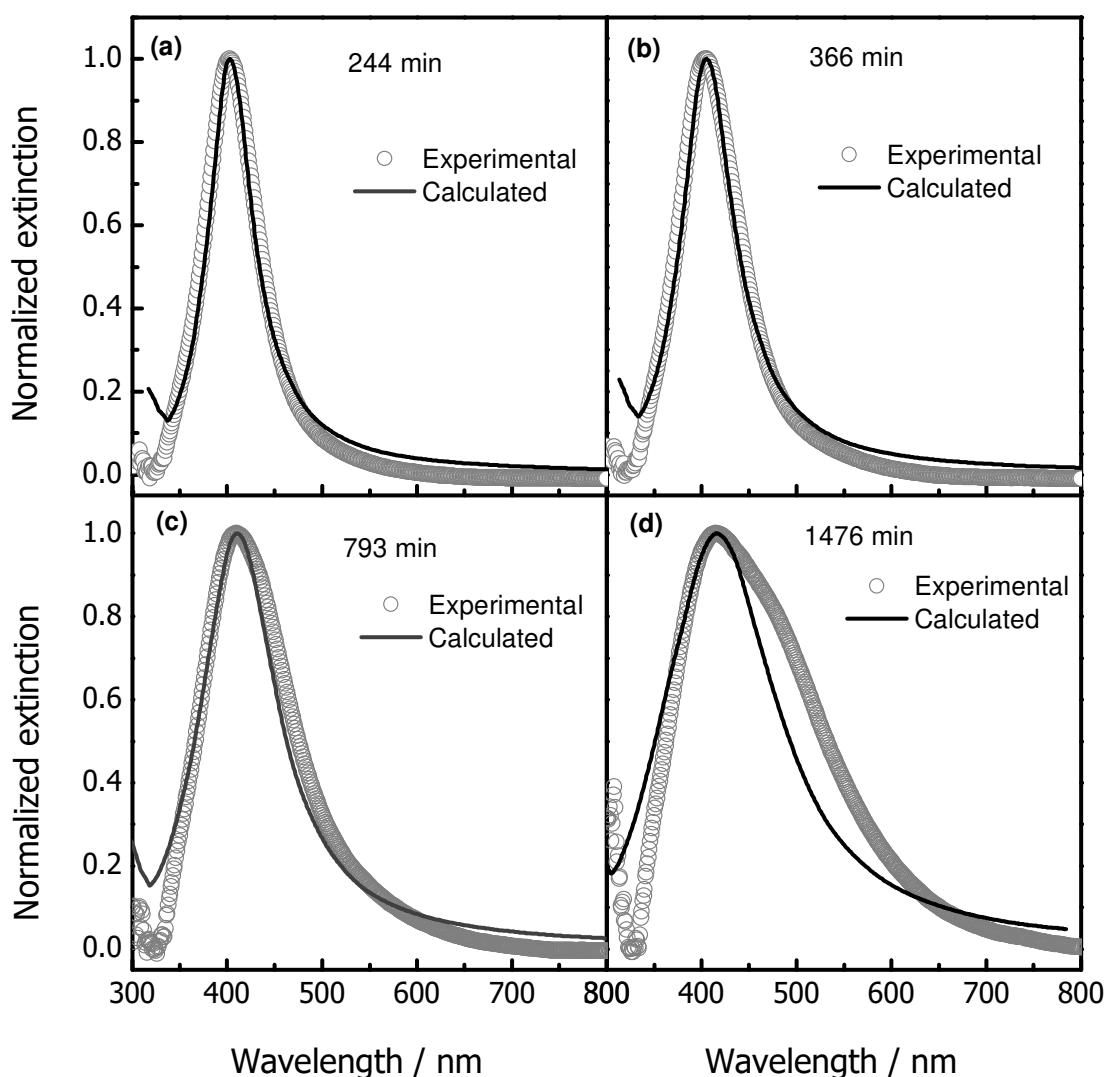
Figure 51. Experimental and calculated surface-plasmon resonance applying the Mie model method at different reaction times. **_Reaction conditions:_** TSC (0.2 mM), temperature: 27 °C, irradiation: Vis (Halogen lamp), gas saturation: 3 bar N_2.

5.4.3. Long term experiments in batch and continuous flow

With the results obtained from the kinetic investigations, the LCWM microreactor opened the possibility of developing ultra-fast experiments for predicting colloids behavior under long-term storage conditions. As mentioned above, for semi-batch conditions, a rapid AgNPs photooxidation during the first 90 min is observed (Figure 52a step 1 → 2). If the "clear" solution stays irradiated under aerobic conditions, it is possible that the photooxidation of citrate catalyzed by Ag^+ should become relevant. This opens the possibility for re-nucleation, aggregation, and formation of new Ag clusters from dissolved metallic silver. The latter process

seems to happen with the slowly formation of a new surface-plasmon resonance spectra, as recorded in Figure 52a step 2 to 3. This behavior, somehow, endorses the affirmation that NPs generation may be an intrinsic property of materials oxidized and reduced, as previously discussed by Glover et al. [142]. To avoid refractive index variation effects, Figure 52b shows the first-order derivative spectra for selected stages through the whole reaction. Interestingly, negative absorbance values and opposing first derivative spectra, are evidence of new clusters with special optical properties (e.g. light emission) that, as much as the author knows, have not been evidenced in literature. Unfortunately, in this study, reaction products analysis was not possible, remaining unclear the complete characteristics of these new clusters. This behavior (photooxidation → NPs growth) has been more or less observed in batch experiments developed in [125], but after 3 months of irradiation time compared to less than a day LCWM experiments (18 hours).
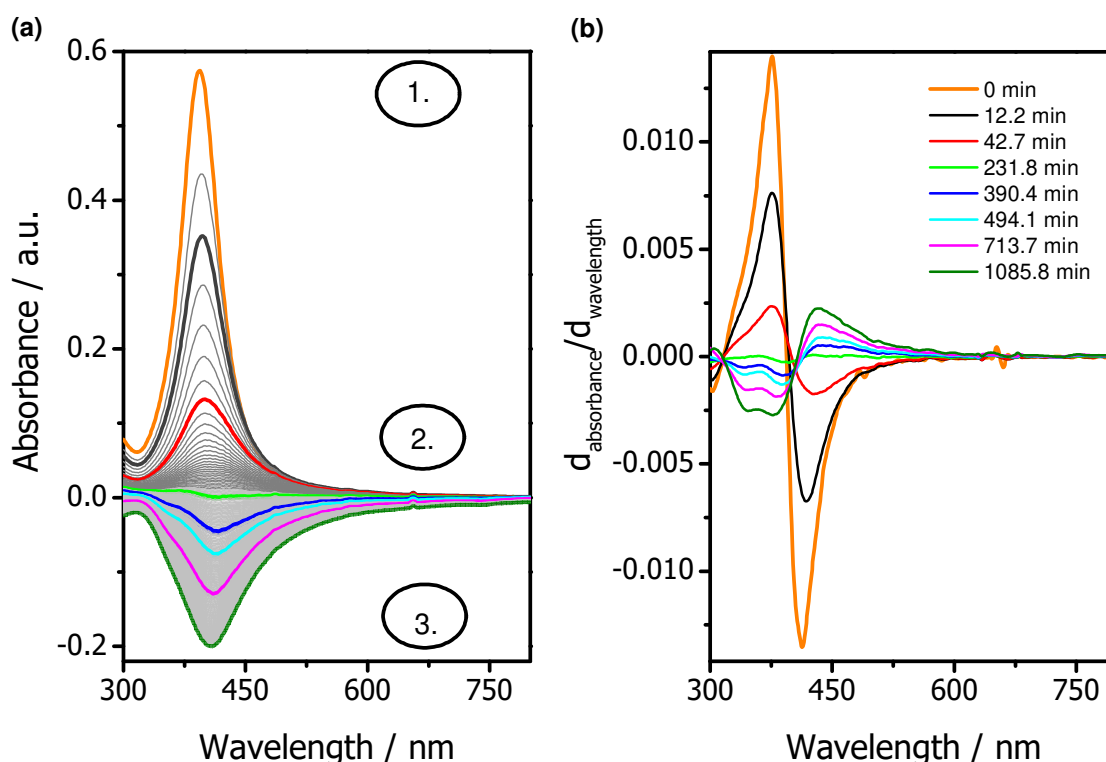
Figure 52. (a) Example absorption spectra for the photooxidation and re-nucleation of silver clusters under long-term irradiation experiments. Step 1 to 2: photooxidation, and step 2 to 3: re-nucleation and NP agglomeration. (b) First-order derivative spectra curves of (a). *Reaction conditions:* TSC (0.2 mM), temperature: 27 °C, irradiation: UV/Vis (deuterium and Halogen lamp), gas saturation: 3 bar synth. air.

While all prior NP degradation studies were discontinuous for the NP suspension (but continuous flushing of the gas phase), also an experiment with continuous pumping of the NP suspension through the reactor was carried out. The suspension was recycled continuously during this experiment. Also these measurements showed baseline distorted similar to the discontinuous experiments under visible light irradiation. Figure A.22 shows that the NP aggregation under convective liquid flow is faster compared to the discontinuous experiment. This indicates that the flow reduces mass transfer limitations and facilitates a faster aggregation. Also in literature [143] microreactors have been demonstrated to be time-efficient for the synthesis of tetrahedral nanoparticles starting from spherical seeds under external light irradiation. Nevertheless, details which kind of limitation is overcome cannot be deduced at this stage. Exemplary first derivative spectra taken after the first and last cycle shows a pronounced red shift compared to the initial colloid (see Figure 53). Mie model fitting of the UV/Vis spectra would predict clusters after the last cycle (> 50 nm), nevertheless, with a high deviation from spherical shape similar to what was observed in Figure 51d. Figure 54 shows TEM measurements of the irradiated sample. This observation confirms the presence of different clusters present in the solution compared to the initial colloid (see Figure 23a). Coalescence (a) and formation of big NP agglomerates (b, c, and d) in the resulting colloid are noticeable. Interestingly, it is also observable the presence of huge triangular flat shape surfaces, which clearly result from a deposition process triggered by the photo-voltage mechanism, discussed in section 2.5.2 [119]. These results are of interest for performing a complete NPs characterization for predicting colloids behavior after their disposal into a liquid fluent, for instance.
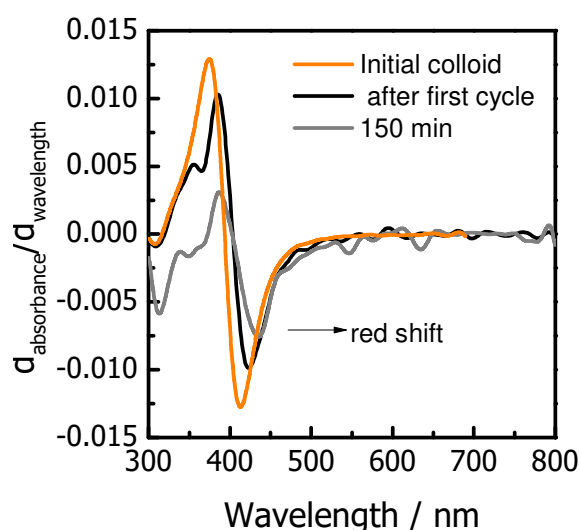
Figure 53. First-order derivative spectra of Ag agglomerates after AgNP colloids irradiation in continuous flow. *Reaction conditions:* TSC (0.2 mM), temperature: 27 ºC, irradiation: UV-Vis (deuterium-halogen lamp), gas saturation: 3 bar synth. air, liquid-phase pressure: 7 bar, time: ≈ 2.5 hours closed loop.
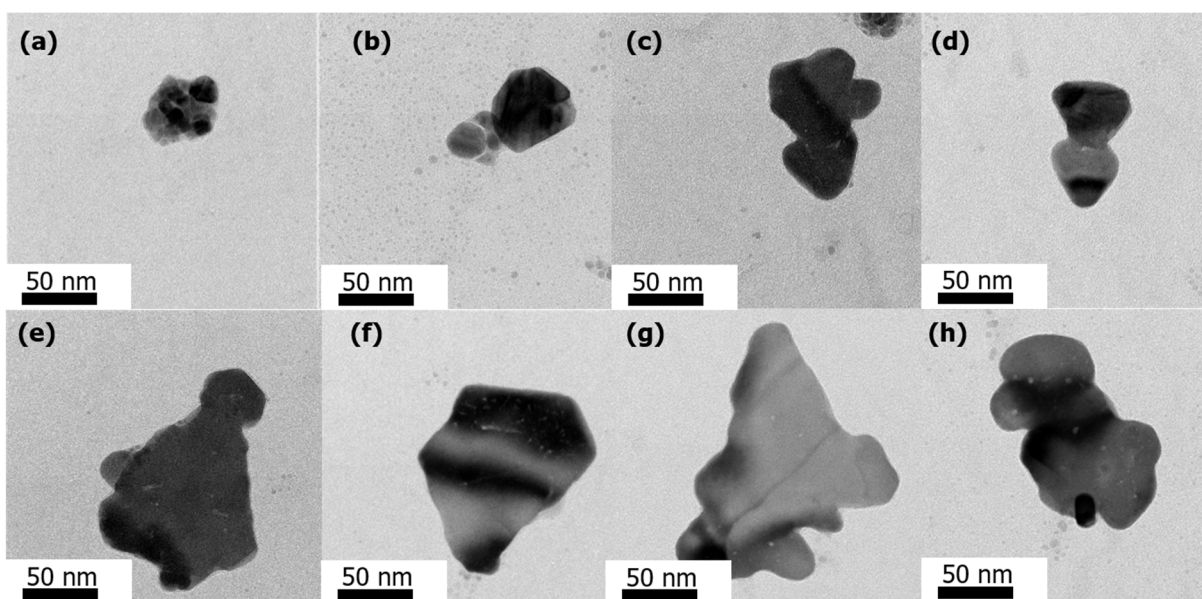
Figure 54. Example TEM images of Ag agglomerates after AgNP colloids irradiation in continuous flow. **_Reaction conditions:_** TSC (0.2 mM), temperature: 27 °C, irradiation: UV-Vis (deuterium-halogen lamp), gas saturation: 3 bar synth. air, liquid-phase pressure: 7 bar, time: ≈ 2.5 hours closed loop.

5.4.4. Conclusion

The case study proved the suitability of the liquid core waveguide membrane microreactor concept to carry out ultra-fast photochemical transformations for kinetic and stability studies of colloidal nanoparticles showing SPR. The kinetics of the photooxidation of AgNPs under UV light irradiation were deduced. While employing an approx. 10^3 times smaller amount of colloidal solution (compared to a 1 cm cuvette), the NPs degradation process are in agreement with what is observed in common photo-reactors developed in the literature [116, 144]. In addition, within the LCWM setup, intense light irradiation combined to controlled aerobic or anaerobic conditions is easily achieved, obtaining degradation results in minutes compared to days-long experiments found in literature. This time-scale is important for avoiding the presence of side reactions (e.g. NPs agglomeration, as observed in [116]), which could alter the reliability of the kinetic investigations. Thus, while common photo-reactor studies allow for qualitative interpretation of photooxidation processes, the experiments within the LCWM reactor enabled reliable quantitative information.

Optical studies under broader (UV + Vis) light irradiation were also developed. In the presence of lower energy wavelengths, a second reaction pathway was clearly observable. Visible light irradiation was found to enhance the indirect citrate photooxidation, which could derivate in

NP growth. Nanoparticle growing was demonstrated by fitting the surface-plasmon resonance of the resulting colloids with the Mie model. Moreover, these two effects were clearly observable by developing long-term photoirradiation studies under aerobic conditions, as schematically represented in Figure 55. Steps 1 to 2 show the fast photooxidation (size reduction) of the initial colloid, due to oxygen saturation and light irradiation. However, once the NPs have been totally degraded, the indirect photooxidation of citrate would reduce this metallic silver ions promoting re-nucleation and NPs formation (Steps 2 to 3). These results are consistent with observations carried out in common photo-reactors (time scale: months), but using much shorter time scales (hours). Finally, studies developed in a continuous loop revealed that flow conditions would promote nanoparticles aggregation and the indirect citrate photooxidation, which triggers the formation of big agglomerates and clusters with flat surfaces.
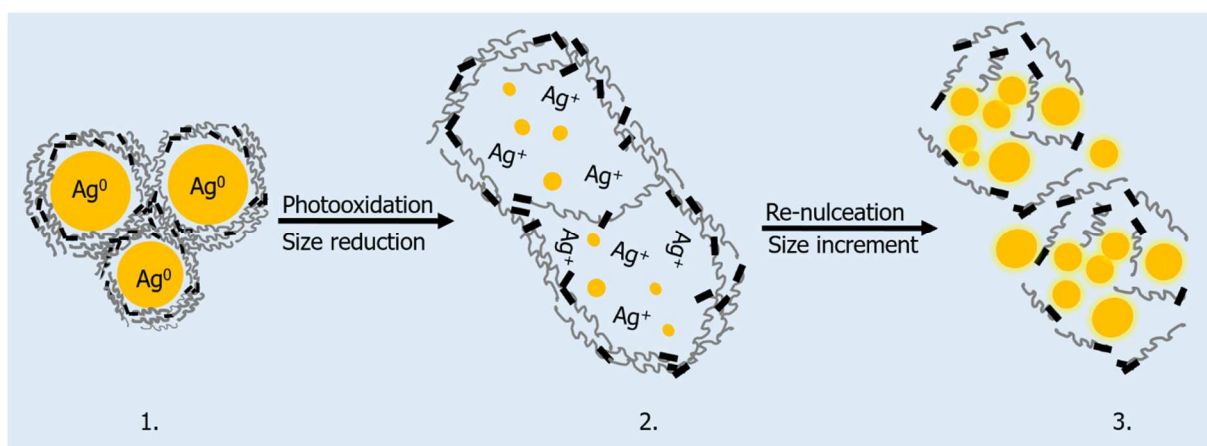
Figure 55. Proposed mechanism for the photooxidation and re-nucleation of silver clusters under long-term broader light irradiation experiments in semi-batch conditions. The scheme represents steps 1 to 3 of Figure 52a. 1-2: (fast) AgNPs photooxidation with subsequently size reduction and possible production of metallic silver. 2-3: (slow) indirect photooxidation of tri-sodium citrate, which involves reduction of silver cations, and subsequently re-nucleation and nanoparticle growth.

6. Conclusions

In this work, an optical liquid core waveguide membrane microreactor for developing *in situ* sensing and/or photoactivation of gas-liquid reactions was successfully designed, built, and applied. The setup is based on a Teflon AF tube, which provides light transmission in a wide spectral range (240-1500 nm) with low optical losses, gas permeation (CO_2, N_2, synth. air) for pressures up to 8 bar, working temperatures up to 150 °C, and uses lesser amounts of initial reactants. Moreover, in the studied regime of continuous operation Bo numbers between 21 and 60 were derived.

In the first application, the LCWM reactor was successfully applied as a chemical reactor for performing redox kinetic investigations of different vanadium-substituted heteropolyacid catalysts during the so-called "OxFA" process. The catalyst reduction kinetics were studied for non (HPA-0) to 5 times (HPA-5) substituted HPA catalysts, at varying temperatures (40 to 80 °C), initial substrates, and catalyst concentrations. With these studies, important information about the kinetics and mechanism of reaction were deduced. Furthermore, the results are consistent with observations carried out in autoclave reactor experiments, but using 10^4 times lesser amount of catalyst, lower pressure, and shorter time scales. Overall, while the HPA-5 catalyst showed, substrate independent, the fastest reduction kinetics, no direct linear correlation of the substitution degree to the reduction kinetics was observed. Combining the kinetic results with CV and EPR characterization indicates, that two competing active sites influence the reduction kinetics. On the one hand, dissolved VO_2^+, and on the other hand the heteropolyanion itself. While the activity of the heteroplyanions as active site itself seem to slow down with higher V-substitution degree, the amount of highly active VO_2^+ dissolved increases with higher substitution. The detrimental effect of vanadium substitution on activity and number of active sites explains the observed reduction activity trend as also selectivity patterns reported in literature. Moreover, for reoxidation experiments, the degree of V-substitution played once more a determinant role. By far, HPA-5 complexes showed the highest initial reoxidation rates, while for mono-and non-substituted catalysts no reoxidation could be observed below 100 °C.

For the second example, the LCWM reactor as a suitable alternative system for *in situ* sensing of gas-liquid-light redox reactions was demonstrated. The tiny amount of samples used, the high resolution measurements, and principally the possibility of performing transient response experiments (gas exchange $N_2 \leftrightarrow$ air) are advantages not easily achievable with conventional photoreactor systems. Furthermore, the ambiguous interactions usually faced when MB acts as

substrate, sensitizer or both were studied. Combining UV/Vis spectra deconvolution with MS- and NMR-spectroscopy, a reaction network for accounting whole thermal and photoactivated pathways was proposed. In summary, under anaerobic conditions, in addition to the MB ←→ LMB redox cycle, MB is also related to a photosensitizer cycle and deamination and N-demethylation processes. Furthermore, the MB-derivatives can further deprotonate, depending on the pH of the solution. On the other hand, under aerobic conditions, MB in its triple state can interact with triplet oxygen to form singlet oxygen, suppressing the deamination and N-demethylation reactions. The photosensitizer cycle seems to be also a major source for fast mineralization organic compounds present.

In the final application, the possibility of performing studies under non homogeneous liquid systems, but colloidal particle suspensions was demonstrated. Ultra-fast photochemical transformations for kinetic and stability studies of silver nanocolloids were developed. Photooxidation of AgNPs under UV light irradiation showed to follow a clear pseudo-first order mechanism, which is in agreement with common photoreactor studies found in literature, but with shorter time-scales. In contrast with common photoreactor studies, within the LCWM allowed for qualitative and quantitative interpretation. Moreover, experiments under UV + Vis light irradiation were also developed. Broader light irradiation showed to add a second reaction pathway related to the indirect citrate photooxidation, which derivates in AG^0 deposition (NPs growth). Thus, the kinetics will result by the two competing mechanism of reaction, which are the oxidation (fast) and reduction (slow) of silver ions at the NP surface. Finally, studies developed in a continuous loop revealed that flow conditions would promote NPs aggregation, which triggers the formation of big agglomerates and flat surfaces.

Overall, in this study was shown that the optical setup could be applied in many laboratory applications with scientific and industrial relevance, which involve *in situ* sensing, photoactivation, and gas-liquid reactions.

7. Annex

7.1. LCWM setup and characterization

LCWM setup

Three basic components are shown in Figure A.1: The LCWM arrangement with inlet and outlet fluidic cells (a), the tube-in-tube contactor for gas permeation, and the gas panel with pressure control (b), and the liquid-phase pressure control (c).
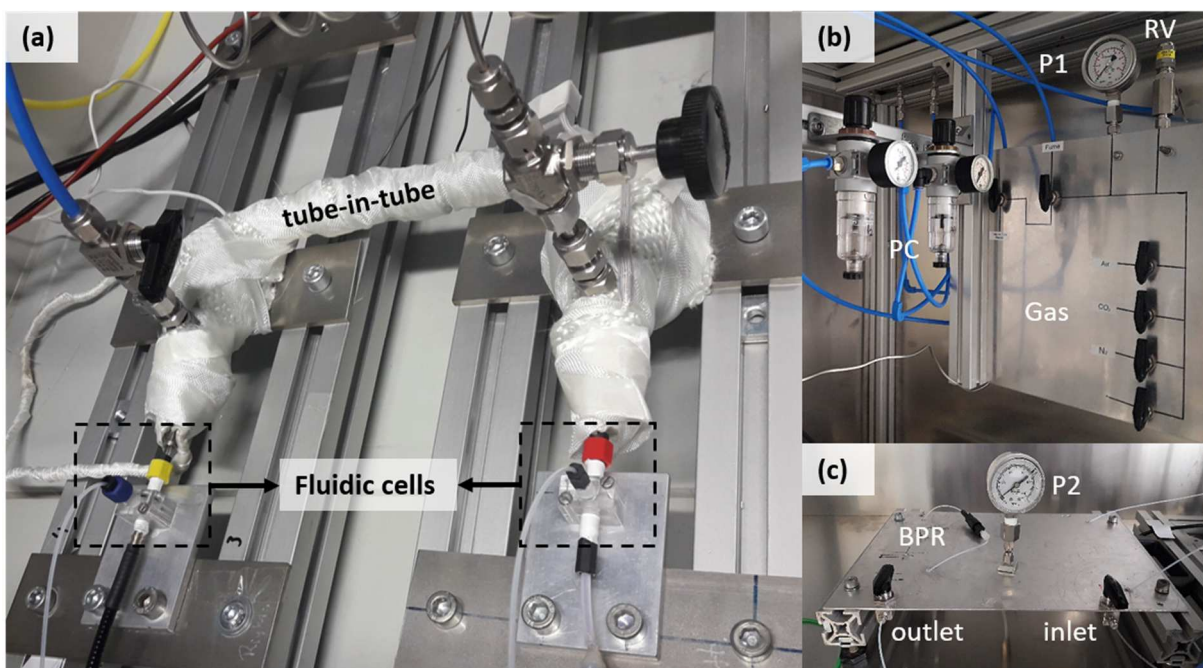
Figure A.1. Picture of LCWM setup (a), gas supply (b), and liquid-phase pressure control (c) (where: P = pressure gauge, RV = release valve, BPR = backpressure regulator, PC = pressure controller).
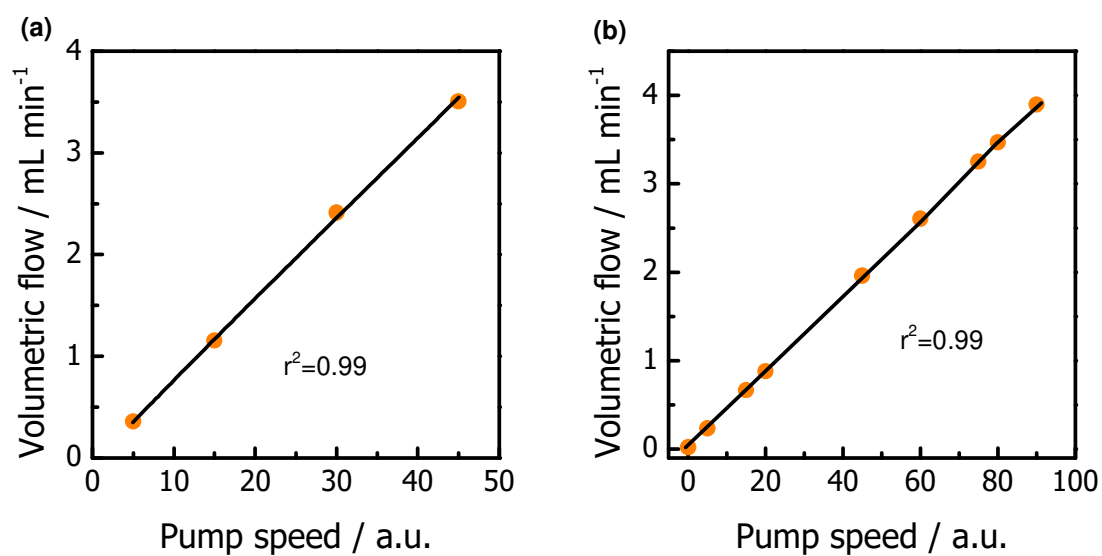
Figure A.2. Pump calibration curves. (a) HPLC pump (E2001, *ProMinent Electronics*) slope: 0.0785. (b) Peristaltic pump (REGLO Analog, *Ismatec*) Intercept: 0.0109; slope: 0.0431.
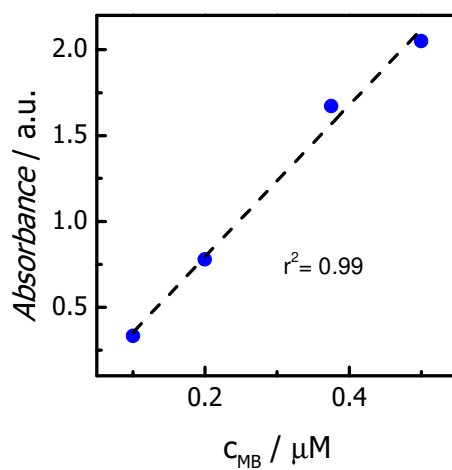
Figure A.3. Example of MB calibration curve at 664 nm in the range 0.1 to 0.6 μM within the LCWM reactor.

Fluidic cells fabrication
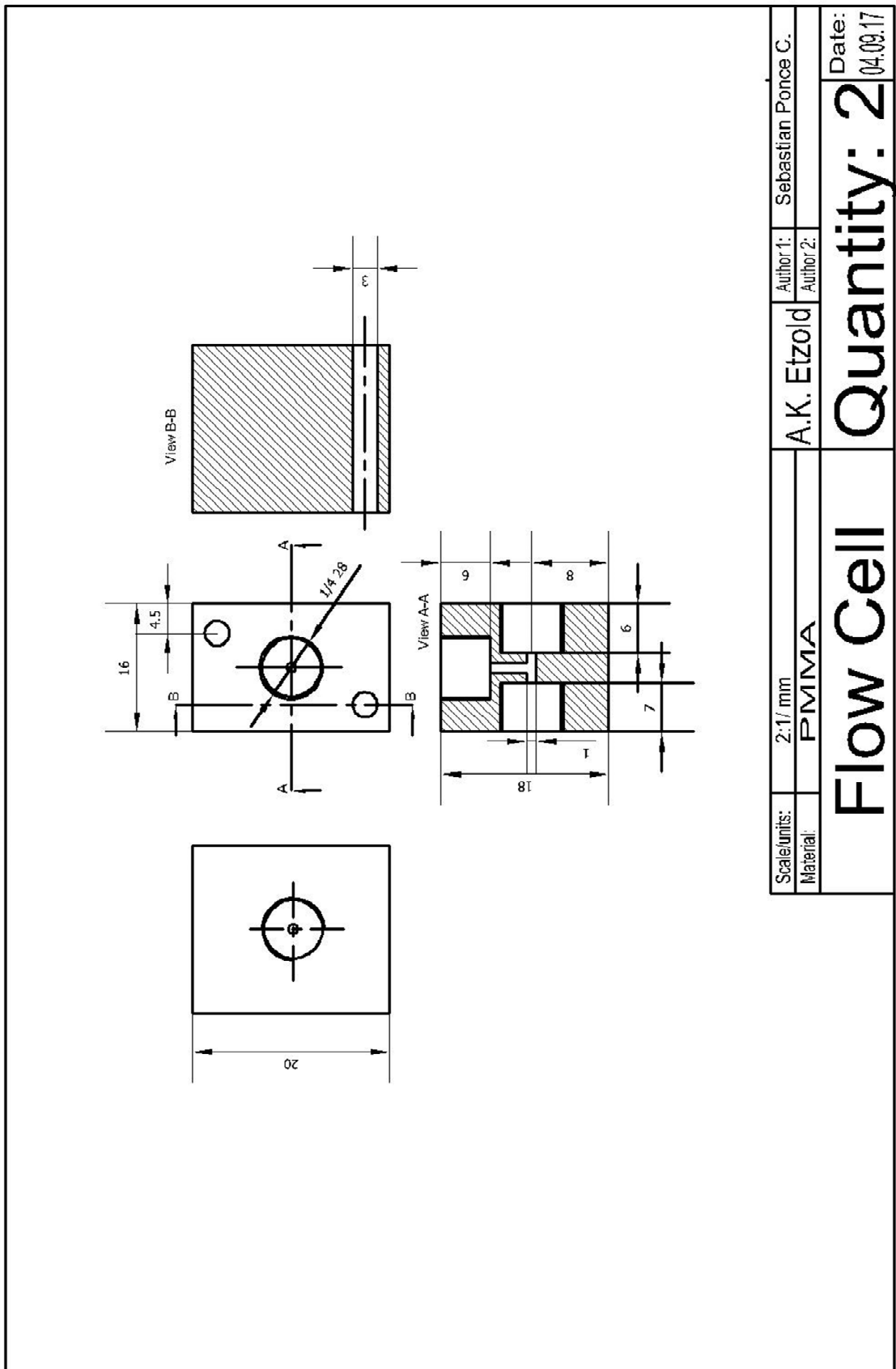
Figure A.4. Sketch of the fluidic cell built in the LCWM reactor.

Optical Loss
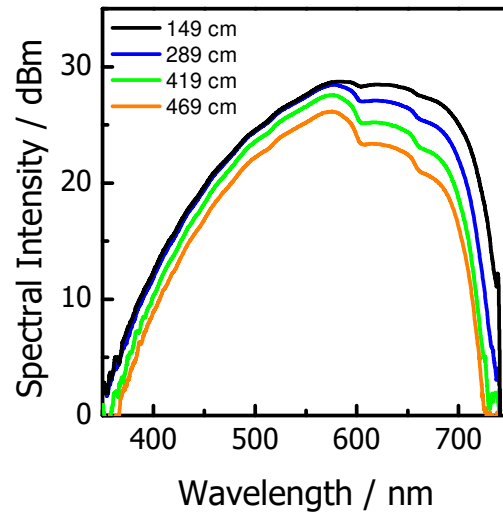
Figure A.5. Spectral intensities of water-filled Teflon AF tubes with different lengths. The spectra were recorded with a compact spectrometer (CSS 100, Thorlabs).

RTD experiments
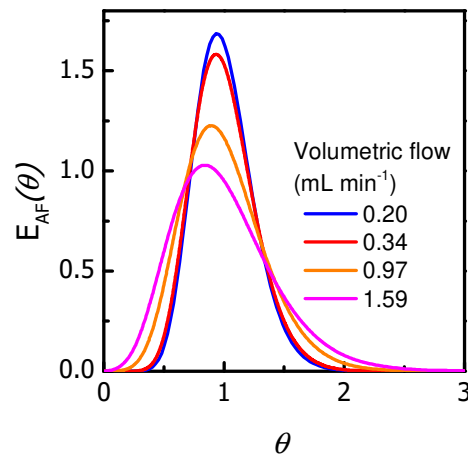
Figure A.6. Calculated Teflon AF age distribution curves, $E_{AF}(\theta)$, obtained from the tank-in-series model for all volumetric flows tested, where θ represents the dimensionless time (t/τ).
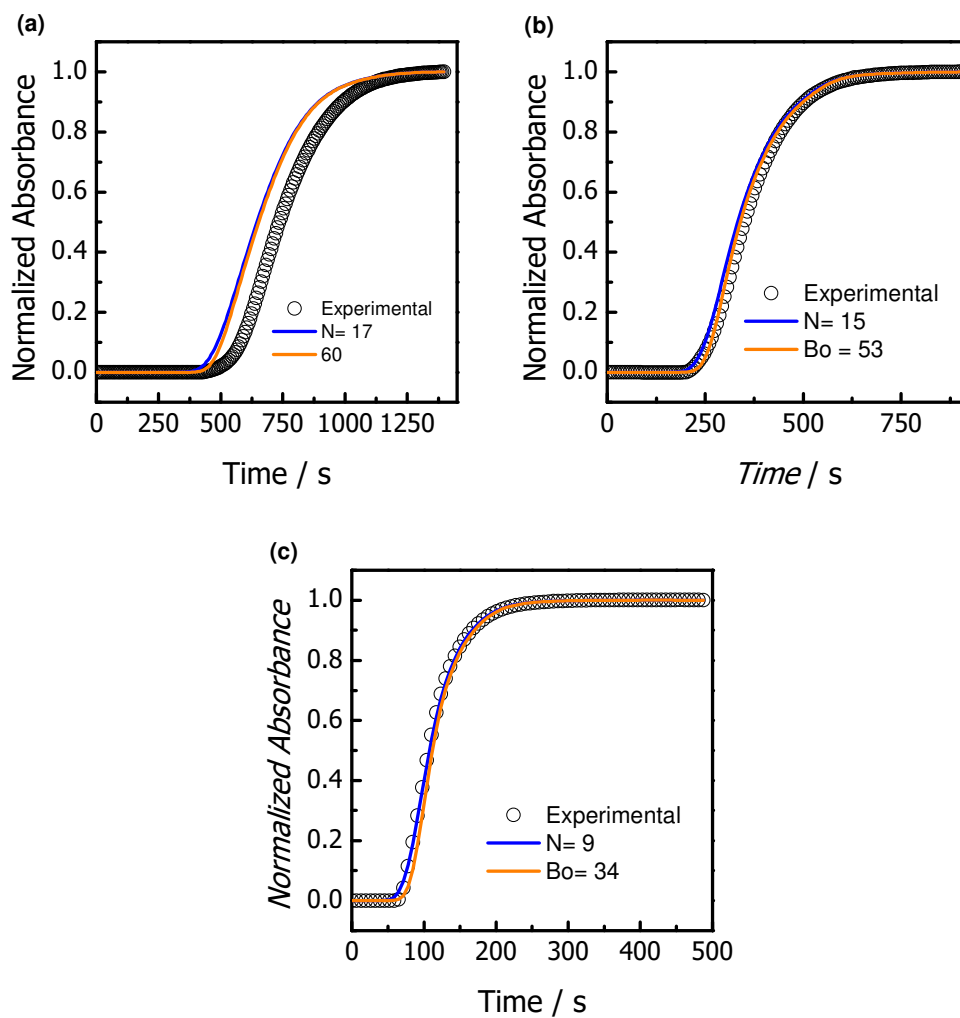
Figure A.7. Step response at the outlet of the Teflon AF tube at a total flow rate of 0.20 mL min^{-1} (a), 0.34 mL min^{-1}(b), 1.59 mL min^{-1} (c). Empty circles: experimental results. Lines: Convoluted curves.

Transient response experiments spectra
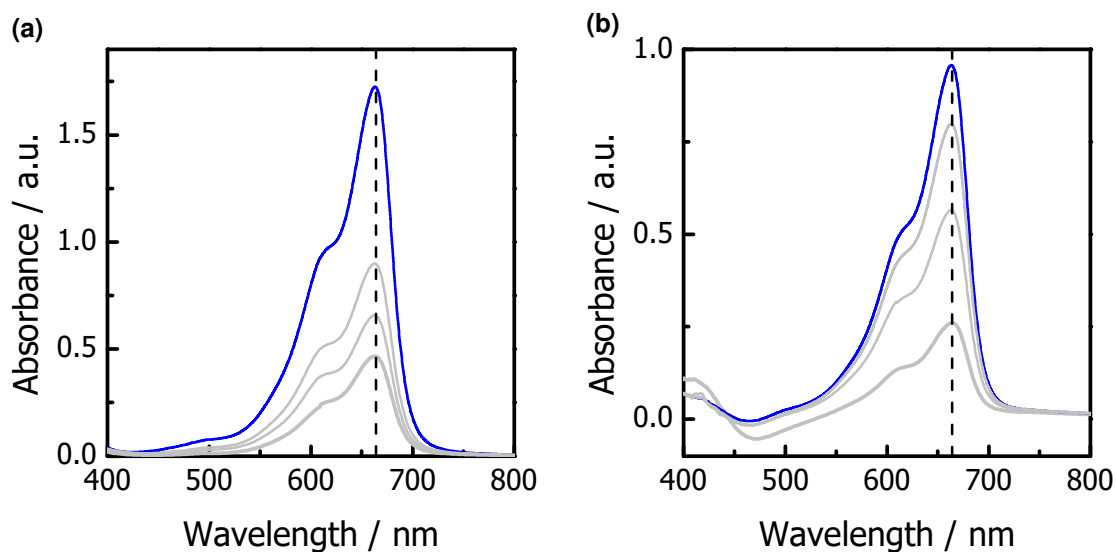
Figure A.8. Example absorbance spectra at different times for experiments under anaerobic and aerobic conditions within a 27 cm LCWM reactor. **Reaction Conditions:** MB as substrate (1 μM), NaBH$_4$ as reducing agent (5 mM), room temperature (373 K), 3 bar gas saturation (N$_2$, and synthetic air). (a) clean fiber, (b) Ag clusters impregnated in the Teflon AF walls.

Light transmission in continuous operation
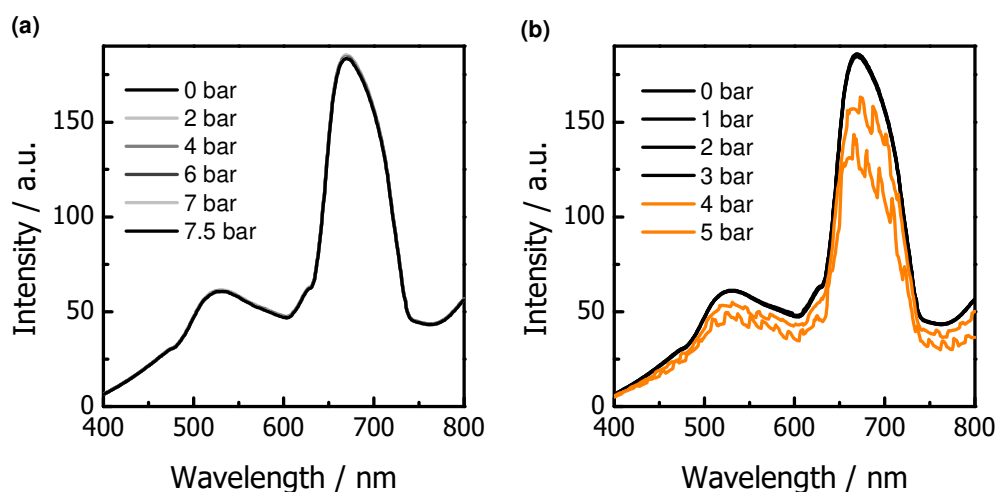
Figure A.9. Example light transmission spectra in a bi-distilled filled LCWM with a fixed liquid-phase pressure of 7 bar (a), and 2.8 bar (b) (Residence time < 30 s).

7.2. Biomass oxidation by HPA-n catalysts

HPA-n_{ox} catalysts reduction under nitrogen saturated systems
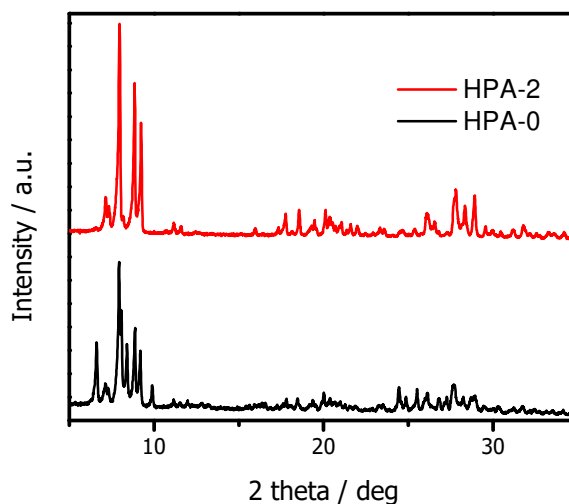
Figure A.10. Powder XRD diffraction measurements in HPA-0 and HPA-2 catalysts.

Autoclave experiments

Table A.1. Oxidative conversion of glucose catalyzed by different heteropolyacids developed in autoclave reactors.

Catalyst	Y_{FA} (%)	Y_{GA} (%)	Y_{CO2} (%)	Y_{total} (%)
HPA-0	0.29	0.46	0.00	0.75
HPA-1	0.00	0.00	0.22	0.22
HPA-2	8.75	3.15	14.41	26.31
HPA-5	52.15	2.78	12.27	67.22

Reaction conditions: 1-25 mg of glucose as a substrate, and 0.1-1 mmoL of catalysts dissolved in 100-200 mL of water, at 20-60 bar O_2, T = 80-90 °C, reaction time: up 22 h, 1000 rpm (GA: Glycolaldehyd).
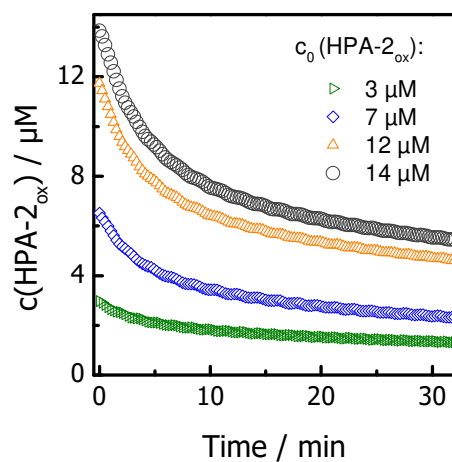
Figure A.11. Concentration vs. time profiles of the reduction of HPA-2ox at 450 nm. **Reaction conditions**: D-glucose as substrate (0.75 mM), HPA-2ox as catalyst (3, 7, 12 and 14 μM), T = 80 °C, 2 bar N_2 saturation in water.
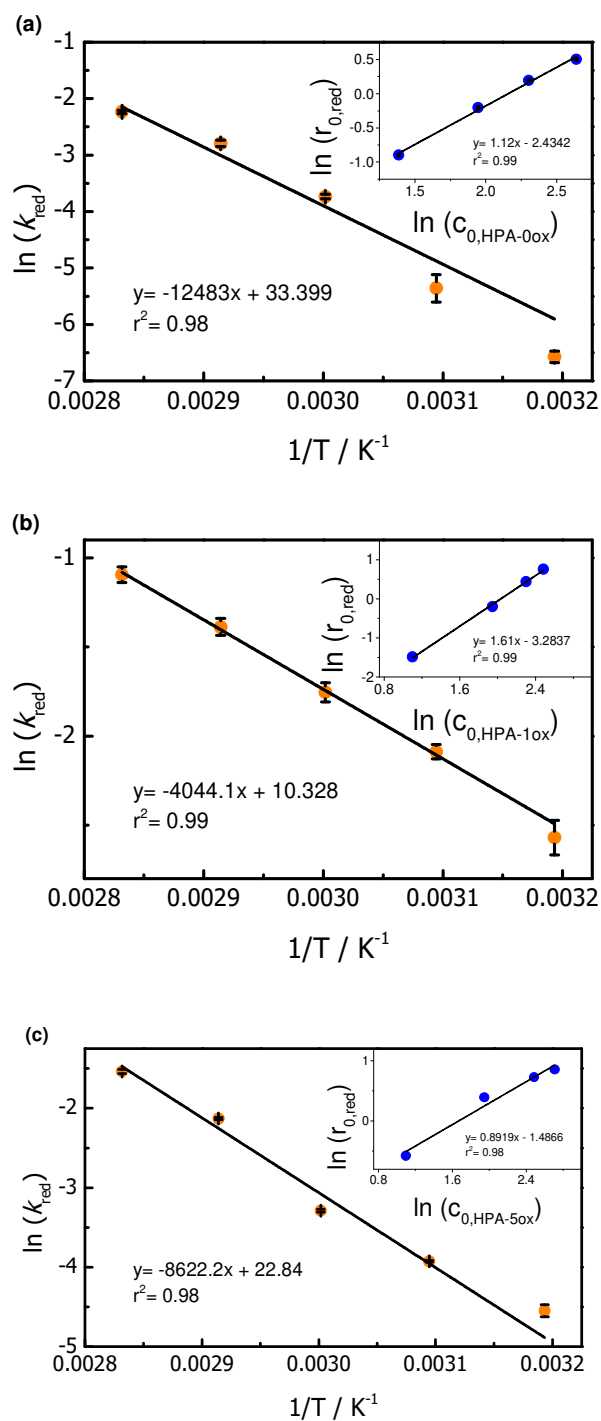
Figure A.12. Arrhenius plot for the reduction of HPA-n_{ox} catalysts. Inset: Logarithmic plot of the reduction reaction rate vs. natural logarithm of initial concentration of HPA-n_{ox} catalyst. (a) HPA-0_{ox}, (b) HPA-1_{ox}, (c) HPA-5_{ox}. (The equations show the values of the best linear regression). ***Reaction conditions***: HPA-n_{ox} as catalyst (3 to 14 µM), D-glucose as substrate (0.75 mM), T = 80 °C, 2 bar N_2 saturation in water.
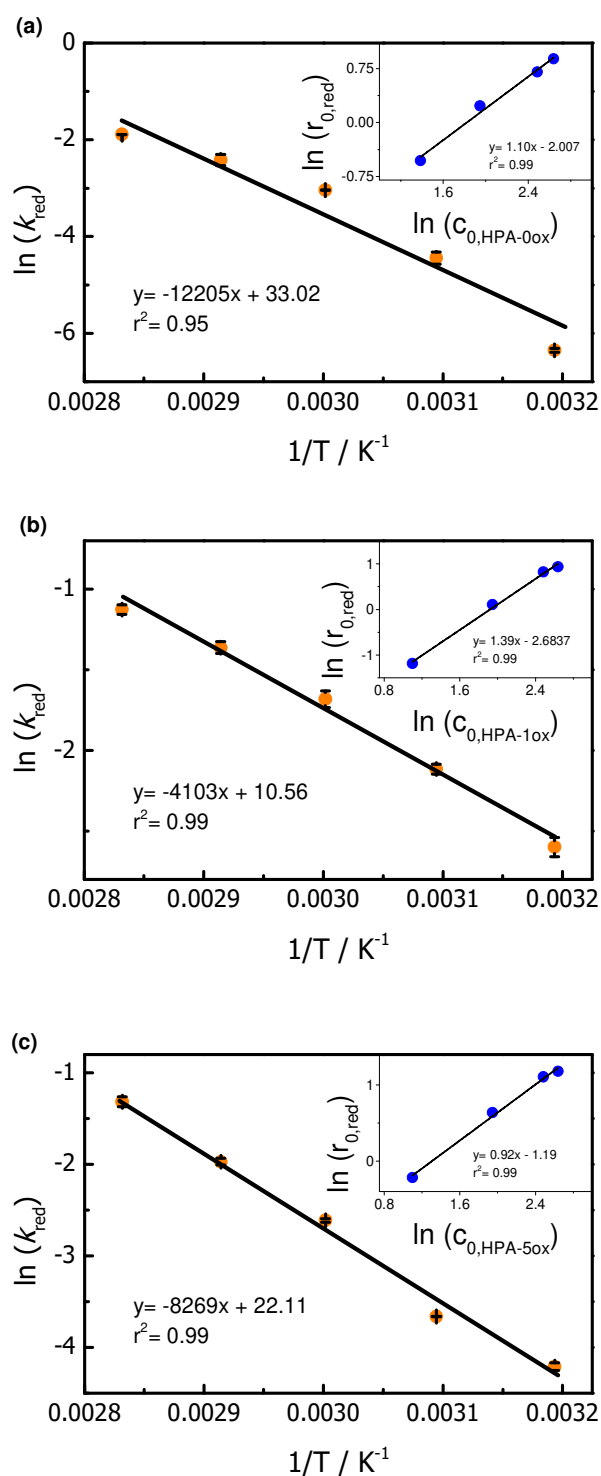
Figure A.13. Arrhenius plot for the reduction of HPA-n_{ox} catalysts. Inset: Logarithmic plot of the reduction reaction rate vs. natural logarithm of initial concentration of HPA-n_{ox} catalyst. (a) HPA-0_{ox}, (b) HPA-1_{ox}, (c) HPA-5_{ox}. (The equations show the values of the best linear regression). ***Reaction conditions***: HPA-n_{ox} as catalyst (3 to 14 µM), Ethylene Glycol as substrate (4 mM), T = 80 °C, 2 bar N_2 saturation in water.
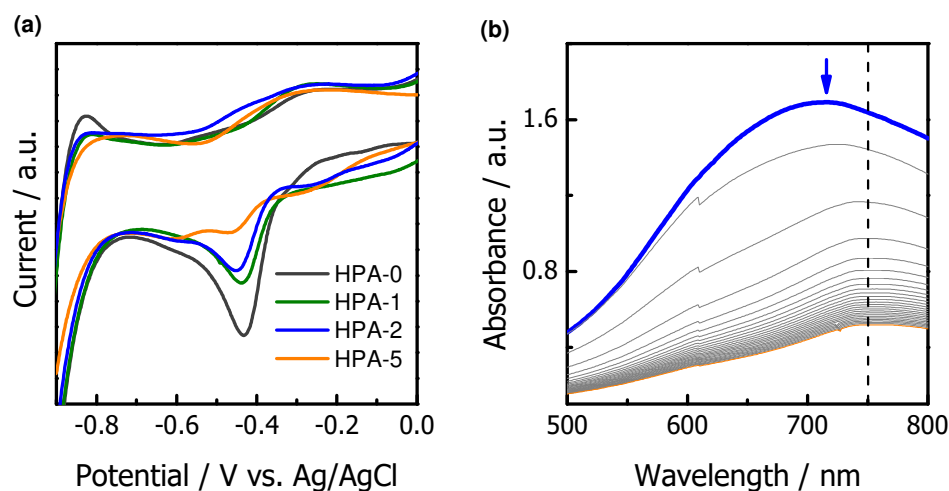
Figure A.14. Cyclic voltammograms of HPA-n catalysts recorded in N_2-saturated 0.5 M Na_2SO_4 aqueous electrolyte solution at a scan rate of 20 mV s^{-1} (pH = 3.3). (b) Example absorption spectra during the reoxidation of HPA-0$_{red}$ catalyst. **Reaction condition**s: HPA-0$_{ox}$ as catalysts (20 µM), T = 140 ºC, 5 bar synthetic air saturation environment.

7.3. MB degradation

Transient response experiments in a methylene blue sodium borohydride solution

An exemplary transient response experiment in homogenous (gas-liquid reaction systems is shown. The MB redox cycle (MB⟵⟶LMB, see Equation (9)) was recorded. For the experiments, the procedure for semi-batch experiments with gas exchange (transient response), as described in Section 4.3, was followed. A mixture solution of MB with a reducing agent was pumped into the system, setting a constant liquid-phase pressure of 4 bar. The reduction step is studied by applying anaerobic conditions. Switching to aerobic conditions by exchanging N_2 with synthetic air allows to observe the oxidation step. Figure A. 15 shows such experiment carried out in a MB/NaBH$_4$ solution. The depletion of MB (orange open circles) and the fully recovery (blue open circles) can be detected. This reversible process (MB ↔ LMB) can be repeated for several cycles.
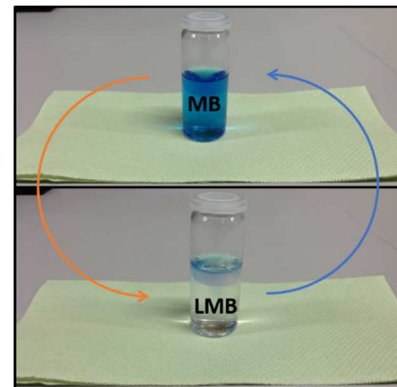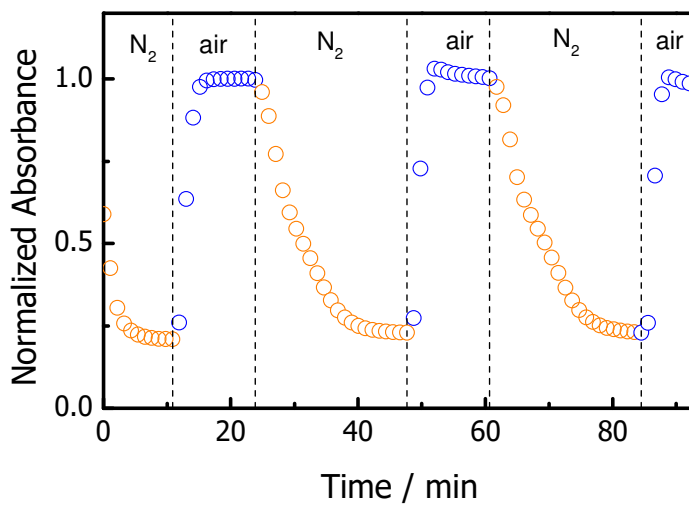
Figure A. 15. Normalized absorbance at MB absorption maxima (664 nm) vs. time for an experiment under anaerobic and aerobic conditions within a 27 cm LCWM reactor. **_Reaction Conditions:_** MB as substrate (1 μM), NaBH₄ as reducing agent (5 mM), temperature: room temperature (373 K), gas saturation: 3 bar (N₂, and synthetic air).

Spectral intensity used in MB degradation experiments
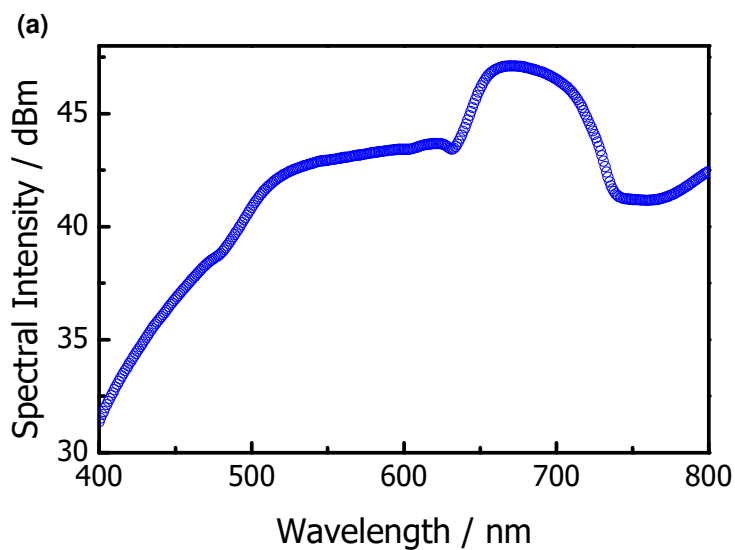
Figure A. 16. Spectral intensity along the water-filled and fully gas-saturated Teflon AF tube (Length of the tube: 27 cm) used in MB-degradation experiments measured with a spectrometer Spectro 320 (D) R5. Halogen lamp (Vis). (Scan speed = 100 ms nm^{-1}, Scan step = 1, Band-pass = 5).

(a)

(b)
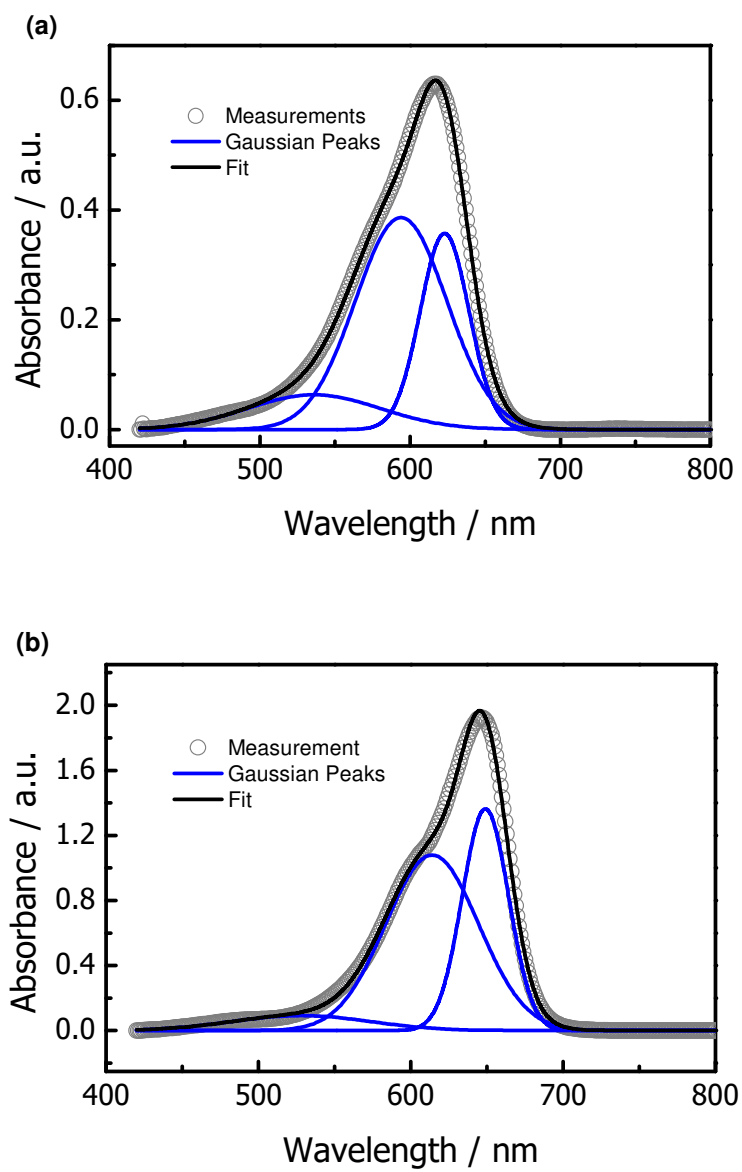
Figure A. 17. Example spectra deconvolution based on a 3 Gaussian peaks method of (a) Methylene Violet B, and (b) Azure B (0.6 μM).

Table A.2. Gaussian parameters for peaks obtained from deconvolution of the visible spectra of different MB degradation species.

Entry	Substance	Center	HWHM	Ratio of height to reference peak
		nm	nm	
1	MB	666	33.4	-
		616	54.8	0.504
		529	109.8	0.033
		565	35.4	0.063
		643	28.8	0.276
		709	26.6	0.022
2	MVB	623	38.2	-
		594	71.8	1.078
		536	104.4	0.178
3	AB	649	35.8	-
		614	72.0	0.790
		528	106.0	0.068
4	AA	640	109.0	-
		601	101.0	0.684
		531	17.4	0.073
5	AC	625	41.2	-
		596	75.6	1.158
		522	109.6	0.118
6	TH	605	31.6	-
		581	67.4	1.222
		524	105.0	0.190
7	D-species	539	104.8	-
		568	61.2	-
		606	33.0	-
		429	101.6	-

7.4. AgNPs photochemical transformations

Spectral intensities used in AgNPs degradation
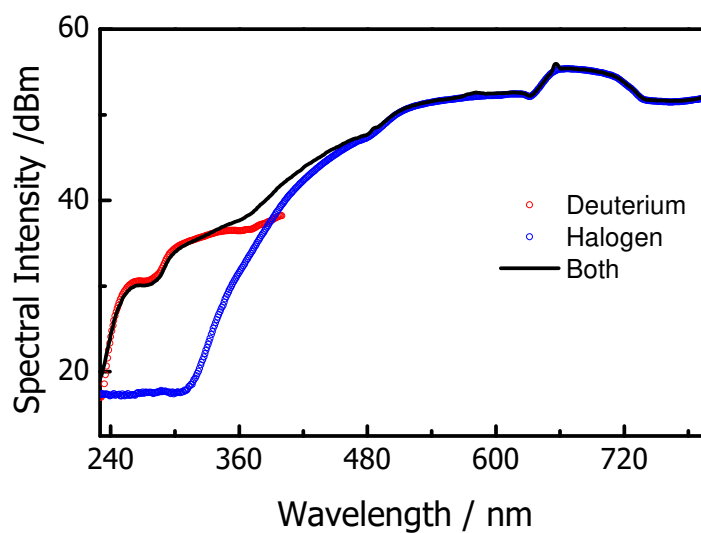
Figure A. 18. Spectral intensity along the water-filled and fully gas-saturated Teflon AF tube measured with a spectrometer Spectro 320 (D) R5. Deuterium (UV), Halogen (VIS) and both lamps (UV/Vis) (Scan speed = 100 ms nm^{-1}, Scan step= 1, Band-pass= 5).

Kinetic experiments
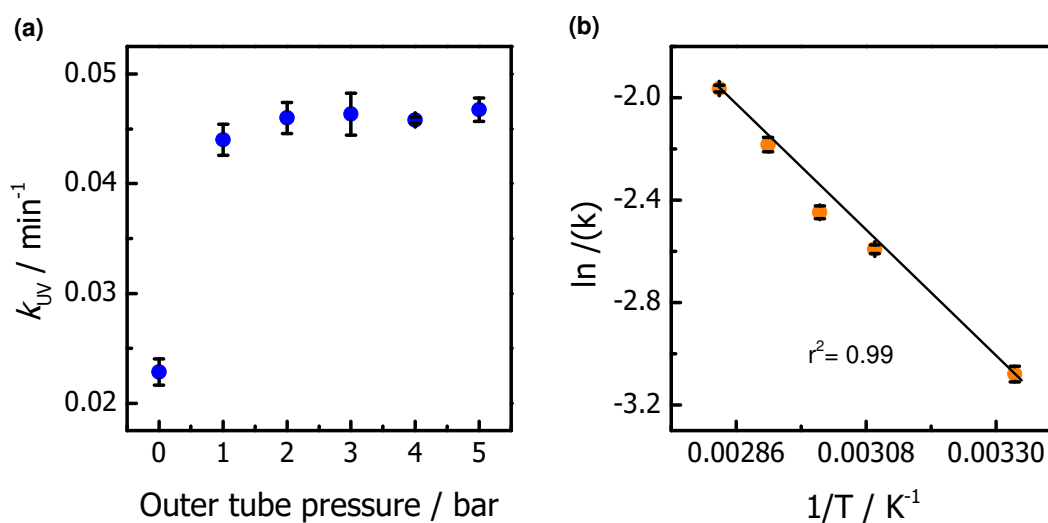
Figure A.19. (a) Oxygen concentration effect on the kinetic constant during the photooxidation of silver NP colloids within the LCWM microreactor (line guide the eye). Reaction conditions: UV-light irradiation, TSC (0.2 mM), room temperature. (b) Arrhenius plot of the photooxidation of AgNPs at different temperatures. **Reaction Conditions**: TSC (0.2 mM), temperature: 27 to 80 °C, irradiation: UV (deuterium lamp), gas saturation: 0 to 5 synth. air.

Broader light irradiation experiment
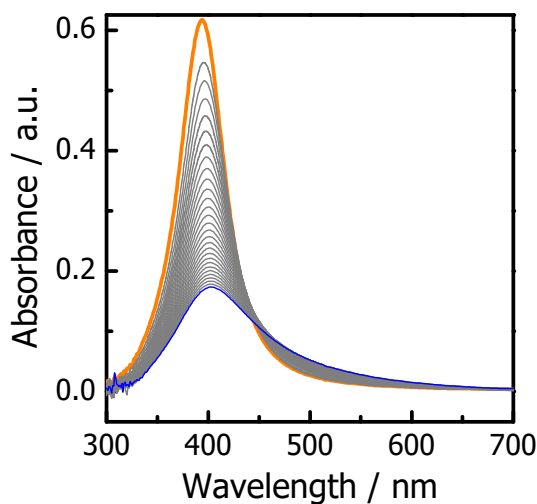
Figure A.20. Example absorption spectra of the photooxidation and aggregation of AgNP colloids. Measurements taken every 360 s. **Reaction conditions:** TSC (0.2 mM), temperature: 27 °C, irradiation: Vis (halogen lamp), gas saturation: 3 bar synth. air.
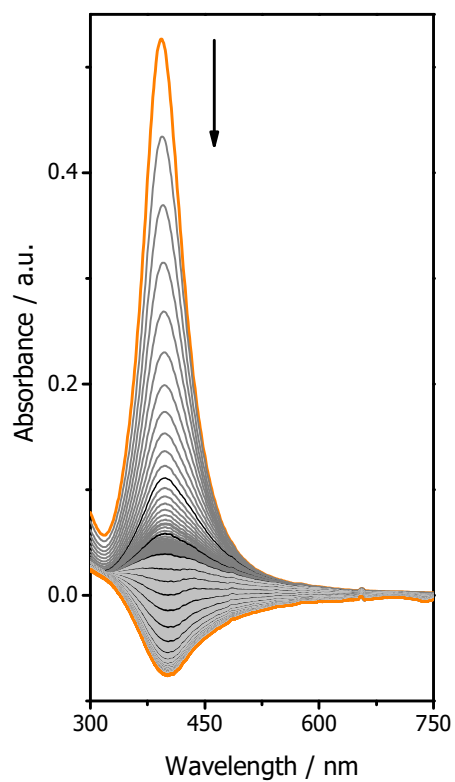
Figure A.21. Example absorption spectra for the photooxidation and re-nucleation of silver clusters under long-term irradiation experiments. ***Reaction conditions:*** TSC (0.5 mM), temperature: 27 °C, irradiation: UV/Vis (deuterium and Halogen lamp), gas saturation: 3 bar synth. air.

Figure A.22. First-order derivative spectra of Ag agglomerates after AgNP colloids irradiation in continuous flow. ***Reaction conditions:*** TSC (0.2 mM), temperature: 27 °C, irradiation: UV-Vis (deuterium-halogen lamp), gas saturation: 3 bar synth. air, liquid-phase pressure: 7 bar, time: ≈ 2.5 hours closed loop.

List of Figures

Abbreviations

AA	Azure A
AB	Azure B
AC	Azure C
AgNP	Silver nanoparticle
AOP	Advanced oxidation process
BCP	Bromocresol purple
BPR	Backpressure regulator
CV	Cyclic Voltammetry
CNPs	Colloidal nanoparticles
D-	Deprotonated
EPR	Electron paramagnetic resonance
FA	Formic acid
FEP	Fluorinated ethylene propylene
HC-PCF	Hollow-core photonic crystal fiber
H-NMR	Proton nuclear magnetic resonance
HPLC	High-performance liquid chromatography
HWFM	Half width of the half maximum
ICP-OES	Inductive coupled plasma-optical emission spectroscopy
IVCT	Homo-intervalence-charge-transfer-bands
LCW	Liquid core waveguide
LCWM	Liquid core waveguide membrane
LMB	Leuco-methylene blue
MB	Methylene blue
MB-OH	N-hydroxy adduct of methylene blue
MS	Mass spectroscopy
MVB	Methylene Violet Bernthsen
PDD	2,2-bis-trifluoromethyl 1-4,5-difluoro-1,3-dioxole
PEEK	polyether ether ketone

PMMA	Polymethyl methacrylate	
POM	Polyoxometalates	
PS	Photosensitizer	
PTFE	polytetrafluoroethylene	
PVP	Polyvinylpyrrolidone	
RTD	Residence time distribution	
SED	Simple electron donor	
SPR	Surface-plasmon resonance	
Teflon AF	Teflon amorphous fluoropolymer	
TEM	Transmission electron microscopy	
TFE	Tetrafluoroethylene	
TH	Thionin	
TIR	Total internal reflection	
TOF-MS	Time-of-flight mass spectroscopy	
TSC	Tri-sodium citrate	
XRD	X-ray diffraction	

Nomenclature

a	reaction order	[-]
A	empirical parameter	[-]
a_L, b_L	MIE scattering coefficients	[-]
b	optical path-length	[cm]
Bo	Bodenstein number	[-]
c	concentration	[mol L^{-1}]
$E(\theta)$	age distribution	[-]
E_a	activation energy	[J mol^{-1}]
ε	molar absorption coefficient	[L mol^{-1} cm^{-1}]
HPA-n	Kegging-type heteropolyacids (n represents the degree of V substitution)	[-]
HPA-n-1	HPA lacunary species	[-]
$HPA - n_{red}$	catalyst in its reduced form	[-]
$HPA - n_{ox}$	catalyst in its oxidized form	[-]

$I_{0,1}$	intensity of incident and transmitted light	[a.u.]
k_{ISC}	Rate constant of intersystem crossing	[s^{-1}]
k_{en}	rate constant of energy transfer	[s^{-1}]
$k_{r,nr}$	rate constant of radiative and non-radiative processes	[s^{-1}]
k	kinetic constant of the photo-Fenton reaction	[s^{-1}]
k_{red}	reduction rate constant	[min^{-1}]
k_{ox}	reoxidation rate constant	[min^{-1}]
k_0	pre-exponential factor	[-]
k_{wv}	wave vector of incident light	[-]
L	length	[cm]
L_{mp}	multi-pole order	[-]
m	degree of reduction	[-]
N	number of tanks	[-]
$^{1,3}O_2$	singlet and ground state triplet oxygen	[-]
m	Degree of reduction	[-]
$P_{1,2}$	light transmission at different length tubes	[-]
$P_{0,liq}$	light transmission with tube filled with tetrachloroethylene and water	[-]
r^2	correlation coefficient	[-]
r$_{ox,red}$	Reoxidaiton and reduction rate	[mol L^{-1} min^{-1}]
$r_{0,red}$	initial reduction rate	[mol L^{-1} min^{-1}]
R	universal gas constant	[8.314 J K^{-1} mol^{-1}]
Re	real part of the complex number $a_L + b_L$	[-]
R_p	radius or size parameter	[m]
$R_{0,ox}$	Initial reoxidation reaction rate	[mol L^{-1} min^{-1}]
S_{0-1}	singlet ground and first excited states	[-]
t	time	[s, min]
T	temperature	[K, ^{o}C]
T_1	first excite triplet state	[-]
(VO_2^+)	pervanadyl	[-]
(VO^{2+})	vanadyl	[-]
V$^{5+,4+}$	vanadium oxidized and reduced species	[-]
ψ_L, η_L	spherical Ricatti-Bessel functions	[-]

$\emptyset$	angle	[rad]
τ	residence time	[s, min]
θ	dimensionless time	[-]
σ_θ^2	variance	[-]
σ_θ	standard deviation	[-]
μ	first raw moment	[-}
η	refractive index	[-]
η_c	complex index of refraction	[-]
η_m	real surrounding medium index of refraction	[-]
Γ_∞	bulk metal value	[s^{-1}]
v_F	fermi speed	[m s^{-1}]
v	flow speed	[cm s^{-1}]
$\propto (\lambda)$	absorption coefficient as function of wavelength	[-]

References

1. Jähnisch, K., et al., *Chemistry in Microstructured Reactors.* Angewandte Chemie International Edition, 2004. **43**(4): p. 406-446.

2. Yao, X., et al., *Review of the applications of microreactors.* Renewable and Sustainable Energy Reviews, 2015. **47**: p. 519-539.

3. Sobieszuk, P., J. Aubin, and R. Pohorecki, *Hydrodynamics and Mass Transfer in Gas-Liquid Flows in Microreactors.* Chemical Engineering & Technology, 2012. **35**(8): p. 1346-1358.

4. Cubillas, A.M., et al., *Photonic crystal fibres for chemical sensing and photochemistry.* Chemical Society Reviews, 2013. **42**(22): p. 8629-8648.

5. Knowles, J.P., L.D. Elliott, and K.I. Booker-Milburn, *Flow photochemistry: Old light through new windows.* Beilstein Journal of Organic Chemistry, 2012. **8**: p. 2025-2052.

6. Cambié, D., et al., *Applications of Continuous-Flow Photochemistry in Organic Synthesis, Material Science, and Water Treatment.* Chemical Reviews, 2016. **116**(17): p. 10276-10341.

7. Wang, N., et al., *Microfluidic reactors for photocatalytic water purification.* Lab on a Chip, 2014. **14**(6): p. 1074-1082.

8. Gilmore, K. and P.H. Seeberger, *Continuous Flow Photochemistry.* The Chemical Record, 2014. **14**(3): p. 410-418.

9. Chen, J.S.Y., et al., *Photochemistry in Photonic Crystal Fiber Nanoreactors.* Chemistry – A European Journal, 2010. **16**(19): p. 5607-5612.

10. Williams, G.O.S., et al., *Photonic crystal fibre as an optofluidic reactor for the measurement of photochemical kinetics with sub-picomole sensitivity.* Lab on a Chip, 2012. **12**(18): p. 3356-3361.

11. Cubillas, A.M., et al., *Ultra-Low Concentration Monitoring of Catalytic Reactions in Photonic Crystal Fiber.* Chemistry – A European Journal, 2012. **18**(6): p. 1586-1590.

12. Schmidt, M., et al., *Chemical and (Photo)-Catalytical Transformations in Photonic Crystal Fibers.* ChemCatChem, 2013. **5**(3): p. 641-650.

13. Ponce, S., et al., *Stable Immobilization of Size-Controlled Bimetallic Nanoparticles in Photonic Crystal Fiber Microreactor.* Chemie Ingenieur Technik, 2018. **90**(5): p. 653-659.

14. Cubillas, A.M., et al., *In Situ Heterogeneous Catalysis Monitoring in a Hollow-Core Photonic Crystal Fiber Microflow Reactor.* Advanced Materials Interfaces, 2014. **1**(5): p. 1300093.

15. Polyzos, A., et al., *The Continuous-Flow Synthesis of Carboxylic Acids using CO2 in a Tube-In-Tube Gas Permeable Membrane Reactor.* Angewandte Chemie International Edition, 2011. **50**(5): p. 1190-1193.

16. Brzozowski, M., et al., *Flow Chemistry: Intelligent Processing of Gas–Liquid Transformations Using a Tube-in-Tube Reactor.* Accounts of Chemical Research, 2015. **48**(2): p. 349-362.

17. Koos, P., et al., *Teflon AF-2400 mediated gas–liquid contact in continuous flow methoxycarbonylations and in-line FTIR measurement of CO concentration.* Organic & Biomolecular Chemistry, 2011. **9**(20): p. 6903-6908.

18. O'Brien, M., et al., *Hydrogenation in flow: Homogeneous and heterogeneous catalysis using Teflon AF-2400 to effect gas–liquid contact at elevated pressure.* Chemical Science, 2011. **2**(7): p. 1250-1257.

19. Wu, G., et al., *A Novel Approach for Measuring Gas Solubility in Liquids Using a Tube-in-Tube Membrane Contactor.* Chemical Engineering & Technology, 2017. **40**(12): p. 2346-2350.

20. Newton, S., et al., *Asymmetric Homogeneous Hydrogenation in Flow using a Tube-in-Tube Reactor.* Advanced Synthesis & Catalysis, 2012. **354**(9): p. 1805-1812.

21. Wu, G., et al., *Continuous Heterogeneously Catalyzed Oxidation of Benzyl Alcohol Using a Tube-in-Tube Membrane Microreactor.* Industrial & Engineering Chemistry Research, 2015. **54**(16): p. 4183-4189.

22. Waterbury, R.D., W. Yao, and R.H. Byrne, *Long pathlength absorbance spectroscopy: trace analysis of Fe(II) using a 4.5m liquid core waveguide.* Analytica Chimica Acta, 1997. **357**(1): p. 99-102.

23. Wang, Z., et al., *A long pathlength spectrophotometric pCO2 sensor using a gas-permeable liquid-core waveguide.* Talanta, 2002. **57**(1): p. 69-80.

24. Páscoa, R.N.M.J., I.V. Tóth, and A.O.S.S. Rangel, *Sequential injection trace determination of iron in natural waters using a long-pathlength liquid core waveguide and different spectrophotometric chemistries.* Limnology and Oceanography: Methods, 2009. **7**(11): p. 795-802.

25. Li, J., P.K. Dasgupta, and Z. Genfa, *Transversely illuminated liquid core waveguide based fluorescence detection: Fluorometric flow injection determination of aqueous ammonium/ammonia.* Talanta, 1999. **50**(3): p. 617-623.

26. Dasgupta, P.K., et al., *Luminescence Detection with a Liquid Core Waveguide.* Analytical Chemistry, 1999. **71**(7): p. 1400-1407.

27. Frosch, T., D. Yan, and J. Popp, *Ultrasensitive Fiber Enhanced UV Resonance Raman Sensing of Drugs.* Analytical Chemistry, 2013. **85**(13): p. 6264-6271.

28. Páscoa, R.N.M.J., I.V. Tóth, and A.O.S.S. Rangel, *Review on recent applications of the liquid waveguide capillary cell in flow based analysis techniques to enhance the sensitivity of spectroscopic detection methods.* Analytica Chimica Acta, 2012. **739**: p. 1-13.

29. Dallas, T. and P.K. Dasgupta, *Light at the end of the tunnel: recent analytical applications of liquid-core waveguides.* TrAC Trends in Analytical Chemistry, 2004. **23**(5): p. 385-392.

30. Jensen, K.F., *Microreaction engineering — is small better?* Chemical Engineering Science, 2001. **56**(2): p. 293-303.

31. K. Schubert, J.B.M.F.G.L.U.S.A.W., *MICROSTRUCTURE DEVICES FOR APPLICATIONS IN THERMAL AND CHEMICAL PROCESS ENGINEERING.* Microscale Thermophysical Engineering, 2001. **5**(1): p. 17-39.

32. Yu, L., et al., *A two-phase segmented microfluidic technique for one-step continuous versatile preparation of zeolites.* Chemical Engineering Journal, 2013. **219**: p. 78-85.

33. Wu, H., et al., *Preparation of Barium Sulfate Nanoparticles in an Interdigital Channel Configuration Micromixer SIMM-V2.* Industrial & Engineering Chemistry Research, 2013. **52**(15): p. 5313-5320.

34. Guidelli, E.J., et al., *Mechanistic Insights and Controlled Synthesis of Radioluminescent ZnSe Quantum Dots Using a Microfluidic Reactor.* Chemistry of Materials, 2018. **30**(23): p. 8562-8570.

35. Chung, C.K., et al., *Design and experiments of a short-mixing-length baffled microreactor and its application to microfluidic synthesis of nanoparticles.* Chemical Engineering Journal, 2011. **168**(2): p. 790-798.

36. Wu, T., et al., *A New Synthetic Method for Controlled Polymerization Using a Microfluidic System.* Journal of the American Chemical Society, 2004. **126**(32): p. 9880-9881.

37. Wang, T., et al., *Optical tweezers directed one-bead one-sequence synthesis of oligonucleotides.* Lab on a Chip, 2011. **11**(9): p. 1629-1637.

38. Lu, H., M.A. Schmidt, and K.F. Jensen, *Photochemical reactions and on-line UV detection in microfabricated reactors.* Lab on a Chip, 2001. **1**(1): p. 22-28.

39. Mengeaud, V., et al., *A ceramic electrochemical microreactor for the methoxylation of methyl-2-furoate with direct mass spectrometry coupling.* Lab on a Chip, 2002. **2**(1): p. 39-44.

40. Abdallah, R., et al., *Micro-structured reactors as a tool for chiral modifier screening in gas–liquid–solid asymmetric hydrogenations.* Catalysis Today, 2007. **125**(1): p. 34-39.

41. Neuenschwander, U. and K.F. Jensen, *Olefin Autoxidation in Flow.* Industrial & Engineering Chemistry Research, 2014. **53**(2): p. 601-608.

42. Yube, K. and K. Mae, *Efficient Oxidation of Aromatics with Peroxides under Severe Conditions Using a Microreaction System.* Chemical Engineering & Technology, 2005. **28**(3): p. 331-336.

43. Schmidt, H. and A.R. Hawkins, *The photonic integration of non-solid media using optofluidics.* Nature Photonics, 2011. **5**: p. 598.

44. Eftekhari, F., et al., *Nanoholes As Nanochannels: Flow-through Plasmonic Sensing.* Analytical Chemistry, 2009. **81**(11): p. 4308-4311.

45. Chen, A., et al., *Dual-color fluorescence cross-correlation spectroscopy on a planar optofluidic chip.* Lab on a Chip, 2011. **11**(8): p. 1502-1506.

46. Khaing Oo, M.K., et al., *Structure fits the purpose: photonic crystal fibers for evanescent-field surface-enhanced Raman spectroscopy.* Optics Letters, 2010. **35**(4): p. 466-468.

47. Hook, B.D.A., et al., *A Practical Flow Reactor for Continuous Organic Photochemistry.* The Journal of Organic Chemistry, 2005. **70**(19): p. 7558-7564.

48. Lévesque, F. and P.H. Seeberger, *Highly Efficient Continuous Flow Reactions Using Singlet Oxygen as a "Green" Reagent.* Organic Letters, 2011. **13**(19): p. 5008-5011.

49. Pinnau, I. and L.G. Toy, *Gas and vapor transport properties of amorphous perfluorinated copolymer membranes based on 2,2-bistrifluoromethyl-4,5-difluoro-1,3-dioxole/tetrafluoroethylene.* Journal of Membrane Science, 1996. **109**(1): p. 125-133.

50. Hougham, G.G., et al., *Fluoropolymers 2.* Vol. 2. 1999: Springer Science & Business Media. 25-33.

51. DUPONT, *Teflon AF Amorphous Fluoropolymers. A new generation of Teflon Fluorocarbon Resins for High Performance [Brochure]*, S.P. Division, Editor.: USA.

52. 2019 04/04]; Available from: http://www.biogeneral.com/teflon-af/.

53. Bai, M., et al., *A compact photometer based on metal-waveguide-capillary: application to detecting glucose of nanomolar concentration.* Scientific Reports, 2015. **5**: p. 10476.

54. Takiguchi, H., et al., *Liquid Core Waveguide Spectrophotometry for the Sensitive Determination of Nitrite in River Water Samples.* Analytical Sciences, 2006. **22**(7): p. 1017-1019.

55. Tao, S., et al., *Mercury atomic absorption by mercury atoms in water observed with a liquid core waveguide as a long path absorption cell.* Analyst, 2004. **129**(4): p. 342-346.

56. Zimmer, L.A. and G.A. Cutter, *High resolution determination of nanomolar concentrations of dissolved reactive phosphate in ocean surface waters using long path liquid waveguide capillary cells (LWCC) and spectrometric detection.* Limnology and Oceanography: Methods, 2012. **10**(8): p. 568-580.

57. Le, T. and S. Tao, *Intrinsic UV absorption spectrometry observed with a liquid core waveguide as a sensor technique for monitoring ozone in water.* Analyst, 2011. **136**(16): p. 3335-3342.

58. Liu, X., et al., *In Situ Spectrophotometric Measurement of Dissolved Inorganic Carbon in Seawater.* Environmental Science & Technology, 2013. **47**(19): p. 11106-11114.

59. Yao, W. and R.H. Byrne, *Spectrophotometric Determination of Freshwater pH Using Bromocresol Purple and Phenol Red.* Environmental Science & Technology, 2001. **35**(6): p. 1197-1201.

60. Wang, Z.A., et al., *In Situ Sensor Technology for Simultaneous Spectrophotometric Measurements of Seawater Total Dissolved Inorganic Carbon and pH.* Environmental Science & Technology, 2015. **49**(7): p. 4441-4449.

61. O'Brien, M., I.R. Baxendale, and S.V. Ley, *Flow Ozonolysis Using a Semipermeable Teflon AF-2400 Membrane To Effect Gas−Liquid Contact.* Organic Letters, 2010. **12**(7): p. 1596-1598.

62. Cranwell, P.B., et al., *Flow synthesis using gaseous ammonia in a Teflon AF-2400 tube-in-tube reactor: Paal–Knorr pyrrole formation and gas concentration measurement by inline flow titration.* Organic & Biomolecular Chemistry, 2012. **10**(30): p. 5774-5779.

63. Bourne, S.L. and S.V. Ley, *A Continuous Flow Solution to Achieving Efficient Aerobic Anti-Markovnikov Wacker Oxidation.* Advanced Synthesis & Catalysis, 2013. **355**(10): p. 1905-1910.

64. Yang, L. and K.F. Jensen, *Mass Transport and Reactions in the Tube-in-Tube Reactor.* Organic Process Research & Development, 2013. **17**(6): p. 927-933.

65. Zhang, J., et al., *Automated in Situ Measurement of Gas Solubility in Liquids with a Simple Tube-in-Tube Reactor.* Analytical Chemistry, 2017. **89**(16): p. 8524-8530.

66. Fukuzumi, S., T. Kobayashi, and T. Suenobu, *Unusually Large Tunneling Effect on Highly Efficient Generation of Hydrogen and Hydrogen Isotopes in pH-Selective Decomposition of Formic Acid Catalyzed by a Heterodinuclear Iridium−Ruthenium Complex in Water.* Journal of the American Chemical Society, 2010. **132**(5): p. 1496-1497.

67. Jin, F., et al., *Hydrothermal conversion of carbohydrate biomass into formic acid at mild temperatures.* Green Chemistry, 2008. **10**(6): p. 612-615.

68. Zhang, J., M. Sun, and Y. Han, *Selective oxidation of glycerol to formic acid in highly concentrated aqueous solutions with molecular oxygen using V-substituted phosphomolybdic acids.* RSC Advances, 2014. **4**(67): p. 35463-35466.

69. Xu, J., et al., *Selective oxidation of glycerol to formic acid catalyzed by Ru(OH)4/r-GO in the presence of FeCl3.* Applied Catalysis B: Environmental, 2014. **154-155**: p. 267-273.

70. Liu, W., et al., *Solar-induced direct biomass-to-electricity hybrid fuel cell using polyoxometalates as photocatalyst and charge carrier.* Nature Communications, 2014. **5**: p. 3208.

71. Albert, J., *Selective oxidation of lignocellulosic biomass to formic acid and high-grade cellulose using tailor-made polyoxometalate catalysts.* Faraday Discussions, 2017. **202**(0): p. 99-109.

72. Wölfel, R., *Katalytische Erzeugung von Wasserstoff aus biogenen Rohstoffen*, in *Lehrstuhl für Chemische Reaktionstechnik*. 2012, Universität Erlangen-Nürnberg,.

73. Albert, J., *Chemische Wertschöpfung aus Biomasse mittels selektiver katalytischer Oxidation zu Ameisensäure (FA) - der Erlanger OxFA-Prozess-Chemical valorization from biomass by selective catalytic oxidation to formic acid (FA) - the Erlanger OxFA-process.* 2015.

74. Wölfel, R., et al., *Selective catalytic conversion of biobased carbohydrates to formic acid using molecular oxygen.* Green Chemistry, 2011. **13**(10): p. 2759-2763.

75. Albert, J., et al., *Selective oxidation of complex, water-insoluble biomass to formic acid using additives as reaction accelerators.* Energy & Environmental Science, 2012. **5**(7): p. 7956-7962.

76. Albert, J., et al., *Spectroscopic and electrochemical characterization of heteropoly acids for their optimized application in selective biomass oxidation to formic acid.* Green Chemistry, 2014. **16**(1): p. 226-237.

77. Reichert, J., et al., *Biomass oxidation to formic acid in aqueous media using polyoxometalate catalysts – boosting FA selectivity by in-situ extraction.* Energy & Environmental Science, 2015. **8**(10): p. 2985-2990.

78. Albert, J. and P. Wasserscheid, *Expanding the scope of biogenic substrates for the selective production of formic acid from water-insoluble and wet waste biomass.* Green Chemistry, 2015. **17**(12): p. 5164-5171.

79. Streb, C., *New trends in polyoxometalate photoredox chemistry: From photosensitisation to water oxidation catalysis.* Dalton Transactions, 2012. **41**(6): p. 1651-1659.

80. Kozhevnikov, I.V., *Catalysis by Heteropoly Acids and Multicomponent Polyoxometalates in Liquid-Phase Reactions.* Chemical Reviews, 1998. **98**(1): p. 171-198.

81. Khenkin, A.M., L. Weiner, and R. Neumann, *Selective Ortho Hydroxylation of Nitrobenzene with Molecular Oxygen Catalyzed by the H5PV2Mo10O40 Polyoxometalate.* Journal of the American Chemical Society, 2005. **127**(28): p. 9988-9989.

82. Li, J., et al., *Catalytic Air Oxidation of Biomass-Derived Carbohydrates to Formic Acid.* ChemSusChem, 2012. **5**(7): p. 1313-1318.

83. Shatalov, A.A. and H. Pereira, *Polyoxometalate catalyzed ozonation of chemical pulps in organic solvent media.* Chemical Engineering Journal, 2009. **155**(1): p. 380-387.

84. Shatalov, A.A., D.V. Evtuguin, and C. Pascoal Neto, *Cellulose degradation in the reaction system O2/heteropolyanions of series [PMo(12−n)VnO40](3+n)−.* Carbohydrate Polymers, 2000. **43**(1): p. 23-32.

85. Sadakane, M. and E. Steckhan, *Electrochemical Properties of Polyoxometalates as Electrocatalysts.* Chemical Reviews, 1998. **98**(1): p. 219-238.

86. Reichert, J. and J. Albert, *Detailed Kinetic Investigations on the Selective Oxidation of Biomass to Formic Acid (OxFA Process) Using Model Substrates and Real Biomass.* ACS Sustainable Chemistry & Engineering, 2017. **5**(8): p. 7383-7392.

87. Caro, H., E.P. 3751, Editor. 1877.

88. Tang, W., et al., *Photodynamic Characterization and In Vitro Application of Methylene Blue-containing Nanoparticle Platforms¶.* Photochemistry and Photobiology, 2005. **81**(2): p. 242-249.

89. Mills, A., et al., *Effect of alkali on methylene blue (C.I. Basic Blue 9) and other thiazine dyes.* Dyes and Pigments, 2011. **88**(2): p. 149-155.

90. Lee, S.-K. and A. Mills, *Novel photochemistry of leuco-Methylene Blue.* Chemical Communications, 2003(18): p. 2366-2367.

91. Mills, A. and J. Wang, *Photobleaching of methylene blue sensitised by TiO2: an ambiguous system?* Journal of Photochemistry and Photobiology A: Chemistry, 1999. **127**(1): p. 123-134.

92. Li, M., et al., *Accelerated methylene blue (MB) degradation by Fenton reagent exposed to UV or VUV/UV light in an innovative micro photo-reactor.* Applied Catalysis B: Environmental, 2016. **187**: p. 83-89.

93. Houas, A., et al., *Photocatalytic degradation pathway of methylene blue in water.* Applied Catalysis B: Environmental, 2001. **31**(2): p. 145-157.

94. DePuccio, D.P., et al., *Degradation of Methylene Blue Using Porous WO3, SiO2–WO3, and Their Au-Loaded Analogs: Adsorption and Photocatalytic Studies.* ACS Applied Materials & Interfaces, 2015. **7**(3): p. 1987-1996.

95. DeRosa, M.C. and R.J. Crutchley, *Photosensitized singlet oxygen and its applications.* Coordination Chemistry Reviews, 2002. **233-234**: p. 351-371.

96. Ye, Y., et al., *Homogeneous photosensitized degradation of pharmaceuticals by using red light LED as light source and methylene blue as photosensitizer.* Chemical Engineering Journal, 2017. **316**: p. 872-881.

97. Bonnett, R., *Photosensitizers of the porphyrin and phthalocyanine series for photodynamic therapy.* Chemical Society Reviews, 1995. **24**(1): p. 19-33.

98. Katafias, A., et al., *Alkaline hydrogen peroxide as a degradation agent of methylene blue—kinetic and mechanistic studies.* 2010. **101**(2): p. 251-266.

99. Basu, S., et al., *Solvent Effect on the Electronic Spectra of Azine Dyes under Alkaline Condition.* The Journal of Physical Chemistry A, 2007. **111**(4): p. 578-583.

100. Zhang, T., et al., *Photooxidative N-demethylation of methylene blue in aqueous TiO2 dispersions under UV irradiation.* Journal of Photochemistry and Photobiology A: Chemistry, 2001. **140**(2): p. 163-172.

101. Yogi, C., et al., *Photocatalytic degradation of methylene blue by TiO2 film and Au particles-TiO2 composite film.* Thin Solid Films, 2008. **516**(17): p. 5881-5884.

102. Marbán, G., T.T. Vu, and T. Valdés-Solís, *A simple visible spectrum deconvolution technique to prevent the artefact induced by the hypsochromic shift from masking the concentration of methylene blue in photodegradation experiments.* Applied Catalysis A: General, 2011. **402**(1): p. 218-223.

103. Tominaga, Y., T. Kubo, and K. Hosoya, *Surface modification of TiO2 for selective photodegradation of toxic compounds.* Catalysis Communications, 2011. **12**(9): p. 785-789.

104. Mueller, N.C. and B. Nowack, *Exposure Modeling of Engineered Nanoparticles in the Environment.* Environmental Science & Technology, 2008. **42**(12): p. 4447-4453.

105. Tsuji, T., T. Kakita, and M. Tsuji, *Preparation of nano-size particles of silver with femtosecond laser ablation in water.* Applied Surface Science, 2003. **206**(1): p. 314-320.

106. Tsuji, T., et al., *Preparation of silver nanoparticles by laser ablation in solution: influence of laser wavelength on particle size.* Applied Surface Science, 2002. **202**(1): p. 80-85.

107. Hajiesmaeilbaigi, F., et al., *Preparation of silver nanoparticles by laser ablation and fragmentation in pure water.* Laser Physics Letters, 2006. **3**(5): p. 252-256.

108. Iravani, S., et al., *Synthesis of silver nanoparticles: chemical, physical and biological methods.* Research in pharmaceutical sciences, 2014. **9**(6): p. 385-406.

109. Kumar, P., et al., *Photocatalytic degradation of methyl orange dye using silver (Ag) nanoparticles synthesized from Ulva lactuca.* Colloids and Surfaces B: Biointerfaces, 2013. **103**: p. 658-661.

110. Vidhu, V.K. and D. Philip, *Catalytic degradation of organic dyes using biosynthesized silver nanoparticles.* Micron, 2014. **56**: p. 54-62.

111. Xiu, Z.-m., et al., *Negligible Particle-Specific Antibacterial Activity of Silver Nanoparticles.* Nano Letters, 2012. **12**(8): p. 4271-4275.

112. Liu, J. and R.H. Hurt, *Ion Release Kinetics and Particle Persistence in Aqueous Nano-Silver Colloids.* Environmental Science & Technology, 2010. **44**(6): p. 2169-2175.

113. Dobias, J. and R. Bernier-Latmani, *Silver Release from Silver Nanoparticles in Natural Waters.* Environmental Science & Technology, 2013. **47**(9): p. 4140-4146.

114. Liu, J., et al., *Controlled Release of Biologically Active Silver from Nanosilver Surfaces.* ACS Nano, 2010. **4**(11): p. 6903-6913.

115. Mock, J.J., et al., *Shape effects in plasmon resonance of individual colloidal silver nanoparticles.* The Journal of Chemical Physics 2002. **116**(15): p. 6755-6759.

116. Gorham, J.M., et al., *UV-induced photochemical transformations of citrate-capped silver nanoparticle suspensions.* Journal of Nanoparticle Research, 2012. **14**(10): p. 1139.

117. Grillet, N., et al., *Photo-Oxidation of Individual Silver Nanoparticles: A Real-Time Tracking of Optical and Morphological Changes.* The Journal of Physical Chemistry C, 2013. **117**(5): p. 2274-2282.

118. Jin, R., et al., *Photoinduced Conversion of Silver Nanospheres to Nanoprisms.* Science, 2001. **294**(5548): p. 1901.

119. Wu, X., et al., *Photovoltage Mechanism for Room Light Conversion of Citrate Stabilized Silver Nanocrystal Seeds to Large Nanoprisms.* Journal of the American Chemical Society, 2008. **130**(29): p. 9500-9506.

120. Stamplecoskie, K.G. and J.C. Scaiano, *Light Emitting Diode Irradiation Can Control the Morphology and Optical Properties of Silver Nanoparticles.* Journal of the American Chemical Society, 2010. **132**(6): p. 1825-1827.

121. Stone, V., et al., *Nanomaterials for environmental studies: Classification, reference material issues, and strategies for physico-chemical characterisation.* Science of The Total Environment, 2010. **408**(7): p. 1745-1754.

122. MacCuspie, R.I., et al., *Challenges for physical characterization of silver nanoparticles under pristine and environmentally relevant conditions.* Journal of Environmental Monitoring, 2011. **13**(5): p. 1212-1226.

123. Kamat, P.V., *Photophysical, Photochemical and Photocatalytic Aspects of Metal Nanoparticles.* The Journal of Physical Chemistry B, 2002. **106**(32): p. 7729-7744.

124. Yin, Y., et al., *Water chemistry controlled aggregation and photo-transformation of silver nanoparticles in environmental waters.* Journal of Environmental Sciences, 2015. **34**: p. 116-125.

125. Gorham, J.M., et al., *Storage Wars: how citrate-capped silver nanoparticle suspensions are affected by not-so-trivial decisions.* 2014. **16**(4): p. 2339.

126. Ponce, S., et al., *Insights into the redox kinetics of vanadium substituted heteropoly acids through liquid core waveguide membrane microreactor studies.* Chemical Engineering Journal, 2019. **369**: p. 443-450.

127. Zhou, L., et al., *Effect of vanadyl species in Keggin-type heteropoly catalysts in selective oxidation of methacrolein to methacrylic acid.* Journal of Catalysis, 2015. **329**: p. 431-440.

128. Rocchiccioli-Deltcheff, C., et al., *Catalysis by 12-Molybdophosphates: 1. Catalytic Reactivity of 12-Molybdophosphoric Acid Related to Its Thermal Behavior Investigated through IR, Raman, Polarographic, and X-ray Diffraction Studies: A Comparison with 12-Molybdosilicic Acid.* Journal of Catalysis, 1996. **164**(1): p. 16-27.

129. Wu, K.-J., G.M. De Varine Bohan, and L. Torrente-Murciano, *Synthesis of narrow sized silver nanoparticles in the absence of capping ligands in helical microreactors.* Reaction Chemistry & Engineering, 2017. **2**(2): p. 116-128.

130. Ponce, S., et al., *An Optical Microreactor Enabling In Situ Spectroscopy Combined with Fast Gas-Liquid Mass Transfer.* Chemie Ingenieur Technik, 2018. **90**(11): p. 1855-1863.

131. Kedenburg, S., et al., *Linear refractive index and absorption measurements of nonlinear optical liquids in the visible and near-infrared spectral region.* Optical Materials Express, 2012. **2**(11): p. 1588-1611.

132. Curcio, J.A. and C.C. Petty, *The Near Infrared Absorption Spectrum of Liquid Water.* Journal of the Optical Society of America, 1951. **41**(5): p. 302-304.

133. Khenkin, A.M. and R. Neumann, *Oxidative C−C Bond Cleavage of Primary Alcohols and Vicinal Diols Catalyzed by H5PV2Mo10O40 by an Electron Transfer and Oxygen Transfer Reaction Mechanism.* Journal of the American Chemical Society, 2008. **130**(44): p. 14474-14476.

134. Park, D.R., et al., *Redox properties and oxidation catalysis of group 5 metal (V, Nb, Ta)-containing Keggin and Wells–Dawson heteropolyacid (HPA) catalysts.* Applied Catalysis A: General, 2010. **373**(1): p. 201-207.

135. Park, D.R., et al., *Redox Properties and Catalytic Oxidation Activities of Polyatom-Substituted HnPW11M1O40 (M = V, Nb, Ta, and W) Keggin Heteropolyacid Catalysts.* 2009. **132**(3): p. 363.

136. Khenkin, A.M., et al., *The kinetics and mechanism of oxidation of reduced phosphovanadomolybdates by molecular oxygen: theory and experiment in concert.* Physical Chemistry Chemical Physics, 2018. **20**(11): p. 7579-7587.

137. Lee, J.K., et al., *Transient responses of the local electronic and geometric structures of vanado-molybdo-phoshate catalysts H3+nPVnMo12−nO40 in selective oxidation.* Applied Catalysis A: General, 2001. **214**(1): p. 125-148.

138. Adamčíková, L.u., K. Pavlíková, and P. Ševčík, *The methylene blue-D-glucose-O2 system. Oxidation of D-glucose by methylene blue in the presence and the absence of oxygen.* International Journal of Chemical Kinetics, 1999. **31**(6): p. 463-468.

139. Matsubara, K. and T. Tatsuma, *Morphological Changes and Multicolor Photochromism of Ag Nanoparticles Deposited on Single-crystalline TiO2 Surfaces.* Advanced Materials, 2007. **19**(19): p. 2802-2806.

140. Ohko, Y., et al., *Multicolour photochromism of TiO2 films loaded with silver nanoparticles.* Nature Materials, 2002. **2**: p. 29.

141. Sato-Berrú, R.Y., et al., *Synthesis of Silver Colloids with a Homemade Light Source.* 2018. **29**(4): p. 719-724.

142. Glover, R.D., J.M. Miller, and J.E. Hutchison, *Generation of Metal Nanoparticles from Silver and Copper Objects: Nanoparticle Dynamics on Surfaces and Potential Sources of Nanoparticles in the Environment.* ACS Nano, 2011. **5**(11): p. 8950-8957.

143. Silvestrini, S., T. Carofiglio, and M. Maggini, *Shape-selective growth of silver nanoparticles under continuous flow photochemical conditions.* Chemical Communications, 2013. **49**(1): p. 84-86.

144. Cheng, Y., et al., *Toxicity Reduction of Polymer-Stabilized Silver Nanoparticles by Sunlight.* The Journal of Physical Chemistry C, 2011. **115**(11): p. 4425-4432.

Sebastián Ponce   Datum:

Troyesstr. 6

64297-Darmstadt

<div align="center">

Erklärung

</div>

Ich erkläre hiermit, dass ich meine Dissertation selbstständig und nur mit den angegebenen
Hilfsmitteln angefertigt und noch keinen Promotionsversuch unternommen habe.

_____

Sebastián Ponce

Sebastián Ponce   Datum:

Troyesstr. 6

64297- Darmstadt

<div align="center">Erklärung</div>

Ich erkläre hiermit, dass die vorliegende elektronische Version meiner Dissertation identisch mit der vorliegenden schriftlichen Fassung ist.

_____

Sebastián Ponce

Resume

Address:	Urb. Biloxi, Oe7-63 y 6ᵗᵃ A, # 252
Birth/place of birth:	10.08.1987 / Quito-Ecuador

Education:

12/2015 - today   **Technical University of Darmstadt, Germany**

Research Assistant / Ph.D. candidate

Thema: "Development and application of a liquid core waveguide membrane microreactor"

10/2013 - 09/2015   **Friedrich Alexander University of Erlangen-Nuremberg, Germany**

M.Sc. with honours (Advanced Materials and Processes)

Master-Thesis: "Application of colloidal PtNi nanoparticles in hydrogenation reactions and their immobilization into photonic crystal fibers for *in situ* catalysis monitoring"

10/2005 - 12/2011   **National Polytechnic School, Quito- Ecuador**

Mechanical Engineer

Bachelor-Thesis: "Obtención de materiales compuestos de matriz polimérica biodegradable reforzada con fibra natural"

09/1999 - 06/2005   **San Gabriel High-school, Quito- Ecuador**

_____

Sebastián Ponce